Spring 5-31-2012

Evolution of 3-d magnetic topology in flare-productive active regions

Yixuan Li
New Jersey Institute of Technology

ABSTRACT

EVOLUTION OF 3-D MAGNETIC TOPOLOGY IN FLARE-PRODUCTIVE ACTIVE REGIONS

by
Yixuan Li

Solar eruptive phenomena, such as flares and coronal mass ejections (CMEs), derive their energy from complex magnetic fields and are the principal source of disturbances that affect space weather. Although physical mechanism and dynamic morphology of flares have been a subject of intense research, many aspects of the flaring process still remain unclear. The objective of this dissertation is to advance the understanding of the physics behind solar flares based on observations, simulations and nonlinear force-free (NLFF) field modeling of magnetic fields.

The data used in this study are obtained from several ground-based or space-borne instruments, including BBSO/DVMG, Hinode/SOT/SP, SDO/HMI and GOES. In addition, the advanced coronal modeling method was utilized to extrapolate NLFF magnetic fields. This dissertation focuses on the magnetic properties (magnetic inclination angle, transverse magnetic field, Lorentz force, etc.) and their evolution associated with flares. The observation is also compared with numerical MHD simulations and theoretical models.

The main findings in this dissertation are briefly summarized as follows: (1) the white-light observation of δ sunspots reveal the rapid penumbral decay and central umbral/penumbral darkening associated with flares; (2) the magnetic inclination angle shows an increase in the decayed peripheral penumbra and a decrease in the central area close to the flaring polarity inversion line (PIL) after major flares; (3) magnetic field observations indicate a rapid and permanent enhancement of the transverse magnetic field in the

umbral core or inner penumbral region, while that in the outer decayed penumbral region decreases; (4) the downward Lorentz force exerted on the flaring area displays a sudden enhancement after flares; (5) the footpoint of flare ribbons shows slow shearing followed by fast diverging and deshearing motion. The remote Hα brightenings appear in the first stage of the eruption while the associated hard X-ray emission occurs in the later phase. These results provide strong evidence favoring superimposed effects of both the tether-cutting model, in which a short and flat loop forms near the photosphere after the eruption, and the back reaction of the coronal magnetic field following the energy release.

The major contribution of this dissertation is: (1) First study of 3-D magnetic field change associated with flares in the perspective of magnetic inclination angle and transverse magnetic field; (2) First successful comparison of the numerical simulation, observation and theory of solar flare associated magnetic field changes; (3) First clear evidence of the two stage magnetic reconnection (implosion and explosion); (4) First evidence in support of the conservation of momentum in solar flare.

To understand the radio emission produced by electrons at the very acceleration site of a solar flare, two competing acceleration models– stochastic acceleration by cascading MHD turbulence and regular acceleration in collapsing magnetic traps were studied. It is found that the radio emission from the acceleration sites (1) has sufficiently strong intensity to be observed by currently available radio instruments and (2) has spectra and light curves which are distinctly different in these two competing models, which makes them observationally distinguishable.

EVOLUTION OF 3-D MAGNETIC TOPOLOGY IN FLARE-PRODUCTIVE ACTIVE REGIONS

by
Yixuan Li

A Dissertation
Submitted to the Faculty of
New Jersey Institute of Technology and
Rutgers, the State University of New Jersey - Newark
in Partial Fulfillment of the Requirements for the Degree of
Doctor of Philosophy in Applied Physics

Federated Physics Department

May 2012

APPROVAL PAGE

EVOLUTION OF 3-D MAGNETIC TOPOLOGY IN FLARE-PRODUCTIVE ACTIVE REGIONS

Yixuan Li

Dr. Ju Jing, Dissertation Co-Advisor — Date
Research Professor of Physics, NJIT

Dr. Haimin Wang, Dissertation Co-Advisor — Date
Distinguished Professor of Physics, Director of Space Weather Research Laboratory, NJIT

Dr. Dale E. Gary, Committee Member — Date
Distinguished Professor of Physics, Director of Owens Valley Solar Array, NJIT

Dr. Andrew J. Gerrard, Committee Member — Date
Professor of Physics, Deputy Director of Center for Solar Terrestrial Research, NJIT

Dr. Zhen Wu, Committee Member — Date
Professor of Physics, Rutgers University, Newark

BIOGRAPHICAL SKETCH

Author: Yixuan Li

Degree: Doctor of Philosophy

Date: May 2012

Undergraduate and Graduate Education:

- Doctor of Philosophy in Applied Physics,
  New Jersey Institute of Technology, Newark, New Jersey, 2012
- Bachelor of Theoretical and Applied Mechanics,
  Peking University, Beijing, P.R.China, 2006

Major: Applied Physics

Journal Publications:

Li, Y., Jing, J., Fan, Y., and Wang, H., "Comparison Between Observation and Simulation of Magnetic Field Changes Associated with Flares" 2011, *Astrophysical Journal Letters*, 727, 19.

Li, Y., and Fleishman, G. D., "Radio Emission from Acceleration Sites of Solar Flares" 2009, *The Astrophysical Journal Letters*, 701, 52.

Li, Y., Jing, J., Tan, C., and Wang, H., "The Change of Magnetic Inclination Angles Associated with the X3.4 Flare on December 13, 2006" 2009, *Science in China Series G: Physics Mechanics and Astronomy*, 52, 1702.

Wang, P., Li, Y., Ding, M., Ji, H., and Wang, H. "Evidence of Two-Stage Magnetic Reconnection in the 2005 January 15 X2.6 flare" 2011, *New Astronomy*, 16, 470.

Li, Y., Jing, J., and Wang, H., "Study of the Change of Surface Magnetic Field associated with Flares" 2011, *Proceeding of International Astronomical Union Symposium 273*, pp417-421.

Li, Y., Jing, J., and Wang, H., "3-D Emerging Magnetic Structure of Active Region 11158 Leading Flare on Feb 15 2011", in preparation.

Li, Y., Jing, J., and Wang, H., "Simulated Flare Ribbon Footpoint Motion and Horizontal Lorentz Force Changes Associated with Flare", in preparation.

Presentations:

Li, Y., Jing, J., Fan, Y., and Wang, H. "Comparison Between Observation and Simulation of Magnetic Field Changes Associated with Flares", 2011 Solar Physics Division Meeting, Las Cruces, New Mexico, June, 2011.

Li, Y., Jing, J., and Wang, H. "Evolution of Magnetic Setting in Flare-Productive Active Regions", the American Astronomical Society 216th Meeting, Miami, Florida, May, 2010.

Li, Y., Jing, J., and Wang, H. "The Change of Magnetic Inclination Angles associated with Flares", 2009 Solar Physics Division Meeting , Boulder, Colorado, 2009.

Li, Y., Jing, J., and Wang, H. "The Change of Magnetic Inclination Angles Associated with the X3.4 Flare on December 13 2006", the American Astronomical Society 214th Meeting, Fort Lauderdale, Florida, May, 2008.

To my family,

for their endless love and support

ACKNOWLEDGMENT

This dissertation would not have been possible without the grace of God given me and there are so many people and organizations I would like to gratefully give thanks to for their endless support and guidance throughout my Ph.D. study. The following words are just a small token of my gratitude.

First and foremost, I would like to deeply thank my co-advisor Dr. Haimin Wang, for his great guiding and continuing support. He gave me much valuable guidance and inspiration throughout the Ph.D. study, not only in my academic education but also in personal life. He offered me the opportunity and financial support to step into the world of solar physics, enlightened me with his great wisdom and kindness, and encouraged me all the way through various difficulties. Without him I would not finish this dissertation.

My sincere gratitude also goes to my co-advisor Dr. Ju Jing, for her friendship, encouragement and advice. She has been always very amiable and easy to access if I have questions for her. She spent so much time and energy on my experimental design and data analysis. I heartily appreciate her support and help. I also appreciate that Dr. Gregory D. Fleishman encouraged me to study radio emission from acceleration sites of solar flare. This work is leading to a publication and part of my dissertation.

I am deeply indebted to all of my committee members: Dr. Dale E. Gary, Dr. Andrew J. Gerrard and Dr. Zhen Wu, for their encouragement, support and advice, for taking the time to read this dissertation and give valuable feedback on the draft of this dissertation.

I would also like to thank all my collaborators I've worked with and contributed to

various parts of this research, particulary to Drs. Rui Liu, Chang Liu, Yan Xu and Na Deng. Thanks to all the group members: Hui Song, Changyi Tan, Sung-Hong Park, Samuel Tun and Yuan Yuan. Also to all my friends and colleagues at NJIT. We spent so much time together inside and outside of the lab, sharing our thoughts and happiness, comforting and encouraging each other. I couldn't imagine finishing my Ph.D. without the help and support from them.

I thank the Solar Physics Division of the American Astronomical Society for traveling funds to attend annual conference. I would also like to thank all the rest of the academic and support staff of the Center for Solar-Terrestrial Research and New Jersey Institute of Technology for providing resources and financial support. Special thanks should be given to Ms. Christine Oertel, the administrative assistant in our research center, for assisting me in many ways and made my study life much easier.

Lastly but most importantly, I wish to thank my parents, Peiwen Li and Yuping Li, for the endless moral support during my graduate study. I do not think I could have finished my dissertation without the love and support from my husband, Chunmin Wang.

This work is supported by NASA and NSF through a number of grants: NSF grant AGS-0936665 and AGS-0745744 and NASA grants NNX08-BA22G and NNX08-AQ90G.

TABLE OF CONTENTS

Chapter **Page**

TABLE OF CONTENTS
(Continued)

Chapter **Page**

TABLE OF CONTENTS
(Continued)

Chapter **Page**

LIST OF TABLES

Table **Page**

LIST OF FIGURES

Figure **Page**

LIST OF FIGURES
(Continued)

Figure **Page**

LIST OF FIGURES
(Continued)

Figure **Page**

LIST OF FIGURES
(Continued)

Figure **Page**

Figure **Page**

LIST OF FIGURES
(Continued)

Figure **Page**

LIST OF FIGURES
(Continued)

Figure **Page**

CHAPTER 1

INTRODUCTION

The Sun, as the nearest star, is the most important astronomical body for mankind. As the civilization developed people realized more and more that the Sun is not just a bright lump of gas but a critical supply of steady energy flow for the earth, which nurtures the farming crops and energizes the climatic and atmospheric conditions. In addition, the dynamic and eruptive energy release from the Sun, in form of solar flares and coronal mass ejections (CMEs), essentially affects the Earth's environment and human activities, e.g., the highly energetic particles can produce hazardous radiation to astronauts and cause enormous economic and commercial losses. Nowadays, solar physics entered an unprecedented harvesting era with several atmosphere-free space observation missions, such as YOHKOH, Reuven Ramaty High Energy Solar Spectroscopic Imager (RHESSI), Solar and Heliospheric Observatory (SOHO), Transition Region and Coronal Explorer (TRACE) and Solar Dynamic Observatory (SDO), and various ground-based observing facilities, such as the Global Oscillation Network Group (GONG) and the Big Bear Solar Observatory (BBSO), also with the expanded coverage of the wavelength, from extreme ultraviolet to X-rays and gamma rays. Therefore, the solar research community has devoted a bountiful effort to understanding the physical mechanisms of the impulsive energy release in solar flares and the forecasting the real-time space weather. However, the triggering mechanism and detailed scenarios associated with solar activity remain unanswered questions. This dissertation attempts to shed light on these important questions.

1.1 General Description of Sun

The Sun as the center of the Solar System, accounts for ∼99.86% of the total mass of the Solar System. The Sun is not a peculiar star in the Milky Way galaxy, but a very ordinary star which has typical values of mass, absolute visual magnitude, and effective temperature in G-type main sequence of the Hertzsprung-Russell diagram. The Sun was formed ∼4.58 billion years ago by the collapse of a hydrogen molecular cloud, and is now half way through its main sequence evolution. In about 5 billion years the hydrogen fuel in the Sun's core will be consumed and the outer layer of the Sun will expand thus entering its red giant phase. Following the red giant phase, the Sun will eject its outer layers as a result of the intense thermal pulsation and remain only the extremely hot stellar core which will cool down as a white dwarf for billions of years.

The distance of the Sun to the Earth varies as the Earth moves from perihelion in January to aphelion in July. The astronomical unit (AU) was defined in 1976 by the International Astronomical Union (IAU), as the radius of an unperturbed circular orbit of the Sun, at which a particle of infinitesimal mass would move with an orbital period of 365.2568983 days. Therefore, the value of the astronomical unit is 149,597,870.691 km, approximately equal to the average Earth-Sun distance. Once the AU and the Earth's orbital period (P_E) are determined, the mass of Sun $M_\odot$ could be estimated using the Kepler's third Law:

$$M_\odot \simeq 5.9165 \times 10^{11} \frac{(1AU)^3}{P_E^2} = 1.989 \times 10^{30} kg \tag{1.1}$$

The Sun's radius is measured from its center to the edge of the photosphere, which is 6.955×10^5 km, about 109 times the Earth's radius.

Figure 1.1 illustrates a cutaway view of the Sun, revealing its major interior regions

and its external atmosphere. Like other main-sequence stars, the solar energy is supplied by the nuclear processes which convert hydrogen to helium deep in the interior, referred as the core. The temperature in the core is about 15 million K. Above the core, up to about three-quarter of the solar radius from the center, lies the radiative zone. In the radiative zone, the temperature, pressure and density of the plasma are all in a stable equilibrium. Energy in this zone is transferred by thermal radiation, free of thermal convection. At the top of the radiative zone, energy is transferred with hot gas rising to the surface, radiating the heat and sinking back to the depths in a region over 200,000 km thick, which is called the convection zone. The smallest convective cells are referred as granules. A image of granulation near a sunspot taken by BBSO/New Solar Telescope (NST), is shown in Figure 1.2. The diameter of a typical granule is in the order of 1,500 km and granules exist for 8-10 minutes before dissolving. Hart (1956) discovered a velocity field which fluctuates on the photosphere and subsequently the large cellular pattern with a mean size of 30,000 km was found and named supergranulation (Leighton et al. 1962). The lifetime of supergranulation is of the order of 24 hours. Mesogranulation is an intermediate scale of convection between granulation and supergranulation, with a characteristic scale of 3-10 Mm and lifetime of 3-10 hours.

The photosphere is the visible surface of the Sun with the thickness of a little more than one hundred kilometers and a temperature of $\sim$ 6000 K. The solar gas converts from almost completely transparent to completely opaque through the photosphere and going inwards. The energy escapes the Sun from the photosphere entirely. The solar atmosphere is the part of the Sun above the photosphere and comprises three zones: the chromosphere, the transition region and the corona. The chromosphere is a layer about 2000 km thick and the temperature in the chromosphere increases gradually with altitude from about 4000 K

up to around 20,000 K near the top. Above the chromosphere lies the transition region with a thin layer about 200 km thick and a rapidly rising temperature from 20,000 K to nearly 1,000,000 K. The corona is the outer atmosphere of the Sun extended into space with average temperature of 1,000,000-2,000,000 K.

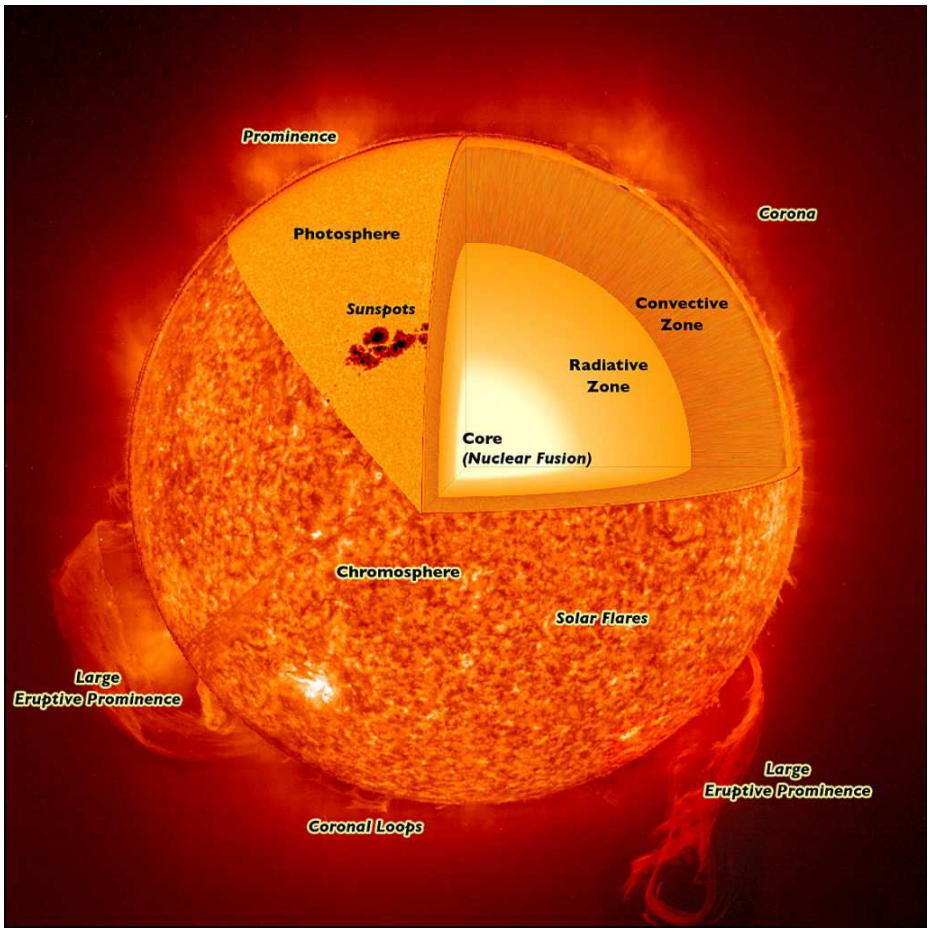

Figure 1.1 A cutaway view of the Sun with labels identifying various parts of the Sun. Moving outward from the center, the regions of the Sun's interior are the core, radiation zone, and convection zone. The photosphere, which is the visible surface of the Sun, is the boundary between the solar interior and the Sun's atmosphere. The atmosphere of the Sun includes the thin chromosphere and the extended corona (courtesy of NASA).

The chemical composition of the solar atmosphere is primarily hydrogen and helium which account for 92.1% and 7.9% of the number of atoms in the photosphere respectively. In 1814, Joseph von Fraunhofer investigated the visible spectrum of the Sun

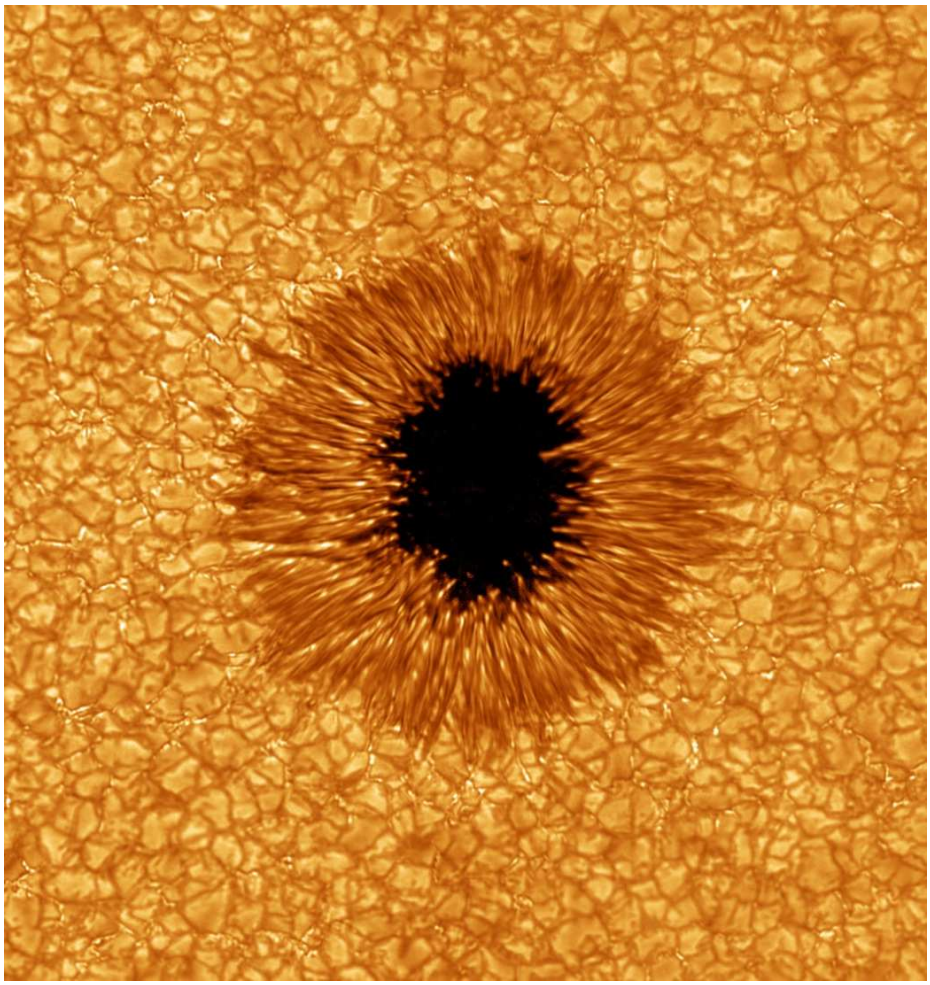

Figure 1.2 Image of NOAA active region 1084 taken on July 2, 2010 in BBSO TiO (706 nm) filter and with realtime correction for atmospheric distortion (adaptive optics). The spot is surrounded by the granular field.

and measured the position of over 570 dark lines, which were explained later in 1859 by Gustav Robert Kirchhoff as the absorption of light by cooler gases in the solar photosphere. The dark absorption lines were used to identify the chemical elements in the photosphere and chromosphere of the Sun and also to investigate the relative abundance of the elements there. The 20 most abundant elements in the photosphere are listed in Table 1.1.

1.2 Solar Active Regions and Sunspots

Solar active regions, sites of intense magnetic fields and phenomena of solar activity, are composed of complex magnetic structures, e.g., magnetic knots[1], nested loops of magnetic flux, and extend along concentrated magnetic flux loops into the chromosphere, transition region and corona. In different solar atmospheric layers, the manifestation of the active regions are also quite diverse. Sunspots are the most conspicuous part of active regions observed on the photospheric surface. They are evolving features of the Sun that appear visibly as dark spots with distinct boundaries between umbra, penumbra and surrounding regions, lasting for a few days. In the chromosphere observed at Hα, the isolated sunspots coalesce with many penumbral and penumbral filaments[2]or some overlying large filaments into the larger volume of complex background. From the transition region and throughout the corona, the active regions begin to be bright and hot as observed in Extreme Ultraviolet (EUV) and X-ray images, although the region directly over sunspots remains relatively cool.

---

[1]Magnetic knots are magnetic field concentrations in the vicinity of sunspots with lifetime of at least 1 hour.

[2]Filaments and/or prominences are large extending features located in the corona but possess temperatures a hundred times lower and densities a hundred or a thousand times greater than coronal values (Priest 1981).

Table 1.1 The 20 Most Abundant Elements in the Photosphere of the Sun Adopted from Lang (2001)

Element	Symbol	Atomic Number	Abundance[a]
Hydrogen	H	1	2.79×10^{10}
Helium	He	2	2.72×10^{9}
Carbon	C	6	1.01×10^{7}
Nitrogen	N	7	3.13×10^{6}
Oxygen	O	8	2.38×10^{7}
Neon	Ne	10	3.44×10^{6}
Sodium	Na	11	5.74×10^{4}
Magnesium	Mg	12	1.07×10^{6}
Aluminum	Al	13	8.49×10^{4}
Silicon	Si	14	1.00×10^{6}
Phosphorus	P	15	1.04×10^{4}
Sulfur	S	16	5.15×10^{5}
Chlorine	Cl	17	5.24×10^{3}
Argon	Ar	18	1.01×10^{5}
Potassium	K	19	3.77×10^{3}
Calcium	Ca	20	6.11×10^{4}
Chromium	Cr	24	1.35×10^{4}
Manganese	Mn	25	9.55×10^{3}
Iron	Fe	26	9.00×10^{5}
Nickel	Ni	28	4.93×10^{4}

[a]Normalized to an abundance of Silicon = 1.00×10^{6}.

The active regions are produced from the convection zone of the Sun by the unceasing evolution of strong magnetic fields emerging up. In 1908, Hale measured magnetic fields on the Sun for the first time and discovered later (Hale et al. 1919) that the magnetic polarity of sunspot pairs varies over a period of ~ 22 years and active regions vary in emerging latitude, number, size, complexity and activity level with an 11-year period. This 11-year period is known as the sunspot cycle or solar activity cycle.

Sunspots possess the strongest magnetic concentration on the solar surface, with the size from 2,400 km to several times Earth's size and magnetic field strength reaching 2000-3000 G. Sunspots appear as dark spots because their temperature is lower than that of the surrounding areas of photosphere. Sunspots usually occur in pairs or groups of opposite magnetic polarity that rotate with the surface of the Sun. They are the footprints of magnetic loops pushing through the surface and holding plasma below. The dark central part of a sunspot is the umbra, while the penumbra is the radial and filamentary structure around the umbra.

There are several schemes to classify the sunspots. Waldmeier (1955) described the Zürich classification, which distinguishes the unipolar and bipolar configurations, the size and complexity of the spot, and the presence or absence of penumbra into nine characteristic stages. This classification is mainly an evolutionary pattern of sunspots, which may take several months for sunspots to go through all the stages. Later on, McIntosh (1990) modified the Zürich classification by adding two more parameters, which deal with the shape and complexity of the largest spot within the group. Nowadays, the frequently used classification is that established by George Ellery Hale and his colleagues, the so-called Mt. Wilson classification (Bray & Loughhead 1979). It is based on the morphology and

magnetic complexity of sunspots. Table 1.2 lists the detailed description of the sunspot classification.

The sunspot classification has proved valuable in the prediction of flares: the more complex the magnetic field is, the more likely the magnetic field is to give rise to flares.

1.3 Solar Flares

1.3.1 Overview of Solar Flares

In the solar system, solar flares are the most powerful magnetic events, which are displayed as sudden and intense brightenings in the chromosphere and corona. Solar flare processes are driven by the accumulation of nonpotential magnetic energy and the instability of the magnetic configuration. They can release up to $10^{25} - 10^{26}$ J of energy in the solar corona. Such energy release results in acceleration of nonthermal particles and heating of the coronal/chromospheric plasma. The electromagnetic radiation emitted during large solar flares can cover almost all wavelengths: from γ-rays, hard X-rays, soft X-rays, through EUV, visible light to radio. It is found that the total flare energy is comparable with the amount of magnetic free energy available in active regions, which is the energy stored in the magnetic field above the potential energy (Metcalf 1994; Metcalf et al. 2005; Schrijver et al. 2008).

The classification of flares has been developed according to their intensity at a given wavelength. Table 1.3 gives the flare classification in 1-8 Å soft X-ray band measured by the Geostationary Operational Environmental Satellite (GOES) and their corresponding peak flux range. A, B, C, M, and X represent the five GOES soft X-ray flare classes in the order of magnitude from weak to strong. Table 1.4 shows the flare classification in Hα wavelength. Among classes in different wavelengths, there is an instinctive correlation,

known as the "Big Flare Syndrome" (Kahler 1982), which is that the larger the flares are the greater the emissions will be at all wavelengths.

There are also many other different ways to categorize solar flares. Based on the morphology of flare sites, solar flares could be divided into two particular types: the compact flare and the two-ribbon flare. The compact flares are point-like flares which occur in simple sunspot structures such as the interaction between open field and new bipolar emergence, with small and short-lived brightenings and without changing its shape during the process. For compact flares, the whole process is usually confined in a relatively small loop in the lower corona. In contrast, the two-ribbon flare is characterized by the two separating bright ribbons which are heated by the flare emission at the feet of the field arcades, i.e., post-flare loops. This type of flare is usually associated with filament eruptions, which are considered as the flare trigger, and maybe accompanied by larger energy release and longer duration. According to the time profile of soft X-ray emission, two types of flares could be classified: single burst and multiple burst flare. The multiple-burst flares include homologous flares (Waldmeier 1938; Martres 1989), which are flare events that recur in nearly identical morphology; sympathetic flares (Richardson 1951; Pearce & Harrison 1990), which describe a pair of flares that occurs almost simultaneously or subsequently in different active regions from certain physical connections; and successive flares (Liu et al. 2009), that multiple eruptions occur in one active region within a short time period.

1.3.2 Theoretical Models of Solar Flares

Although solar flares have been observed in multiple wavelengths, the onset of the flare phenomenon remains a mystery. It has been widely believed that magnetic reconnection is

Table 1.2 Mount Wilson Sunspot Classification Scheme Referred from Bray & Loughhead (1979)

Class	Description
α	Unipolar sunspot group
β	Sunspot group having both positive and negative magnetic polarities (bipolar), with a simple and distinct division between the polarities
γ	Complex sunspot group in which the positive and negative polarities are so irregularly distributed as to prevent classification as a bipolar group
$\beta\gamma$	Sunspot group that is bipolar but which is sufficiently complex that no single, continuous line can be drawn between spots of opposite polarities
δ	Sunspot group in which the umbrae of the positive and negative polarities are within 2 degrees of one another and within the same penumbra
$\beta\delta$	Sunspot group of general beta magnetic classification but containing one (or more) delta spots
$\beta\gamma\delta$	Sunspot group of beta-gamma magnetic classification but containing one (or more) delta spots
$\gamma\delta$	Sunspot group of gamma magnetic classification but containing one (or more) delta spots

Table 1.3 GOES Soft X-ray Classification of Flares

Class	Peak Flux[a] (W m^{-2})
A	10^{-8}–10^{-7}
B	10^{-7}–10^{-6}
C	10^{-6}–10^{-5}
M	10^{-5}–10^{-4}
X	10^{-4} and above

[a]measured at 1-8 Å band

Table 1.4 Hα Classification of Flares

Class	Area[a](degree^2)
S	<2.06
1	2.06–5.15
2	5.15–12.4
3	12.4–24.7
4	>24.7

[a]1 degree^2 = 1.476 × 10^8 km^2 of solar surface

the essential process behind solar flares. Based on observations, different flare models have been put forward to explain certain aspects of the flare phenomenon.

The Standard 2-D Models

The most widely accepted standard 2-D magnetic reconnection model for flares was proposed by Kopp & Pneuman (1976) and has been further elaborated by Tsuneta (1996, 1997) and Shibata (1996). Figure 1.3 is a basic cartoon of the standard eruption model in a bipolar configuration. This classical model is able to explain the observational features of solar flares in many aspects. The initial driver of the flare is an erupting prominence above the neutral line, which is the line dividing the polarities. As the plasma at the top of the flare loop is ejected in association with a CME, the flux rope that stored energy before the eruption erupts outwards and the magnetic field lines are stretched by the prominence and become highly extended, in a so called open configuration. Beneath the erupting prominence, the magnetic field lines relax and form closed loops at the X-type reconnection . The X-type reconnection is that the opposite directed magnetic field lines approach, then break and rejoin. The coronal X-point region (see Figure 1.3 (b)) is assumed to be the major magnetic energy release location, which results in the acceleration of particles and the heating of local coronal plasma. The footpoints (FPs) of the reconnecting field line are heated by the resulting high energy particles to produce Hα and hard X-rays emissions, and the evaporating chromospheric plasma filled into flare loops produces soft X-ray emissions. The flare ribbon FP motion indicates the progression of the reconnected field lines. Therefore, as the successive reconnections take place higher and higher in association with the upward moving X-point, the separation of FPs increases with time, and a cusp structure has been

generated at the top (Klimchuk 1997). A cusp structure refers to the "inverted-Y shaped" postflare loops, which is well regarded as one of the strong evidence of magnetic reconnection. After the eruption, the flux rope reconnects to form a closed and nearly current-free configuration. Thus the original magnetic arcade and the core structure have been greatly altered during the whole flare process.

Many observations have been carried out to measure the FP motion and some results (Sakao et al. 1998) show that half of the flares exhibit an increasing FP separation with a nonthermal hard X-ray spectrum, which could be interpreted in terms of the Kopp-Pneuman scenario. Forbes & Priest (1984) proposed a simple relation between the motion of the flare ribbon and the rate of reconnection represented as the electric field E_{rec} in the reconnecting current sheet:

$$E_{rec} = B_n(X_r)V_r \tag{1.2}$$

where the $B_n(X_r)$ is the vertical magnetic field at the location X_r, and V_r is the velocity of the outer edge of the ribbon. Thus, the electric field produced by reconnection in the corona could be estimated by the observed separation motions of the flare ribbons. The E_{rec} represents the reconnection rate per unit length along the current sheet with a 2-D assumption. To avoid the large uncertainties of evaluating ribbon expansion velocities in the 2-D assumption, and given that the magnetic flux is conserved from the photosphere to the corona and the photospheric magnetic fields are line-tied, the rate of photospheric magnetic flux change φ_{rec} and the total reconnection flux ψ_{rec} are defined as (Forbes & Lin 2000; Qiu & Yurchyshyn 2005)

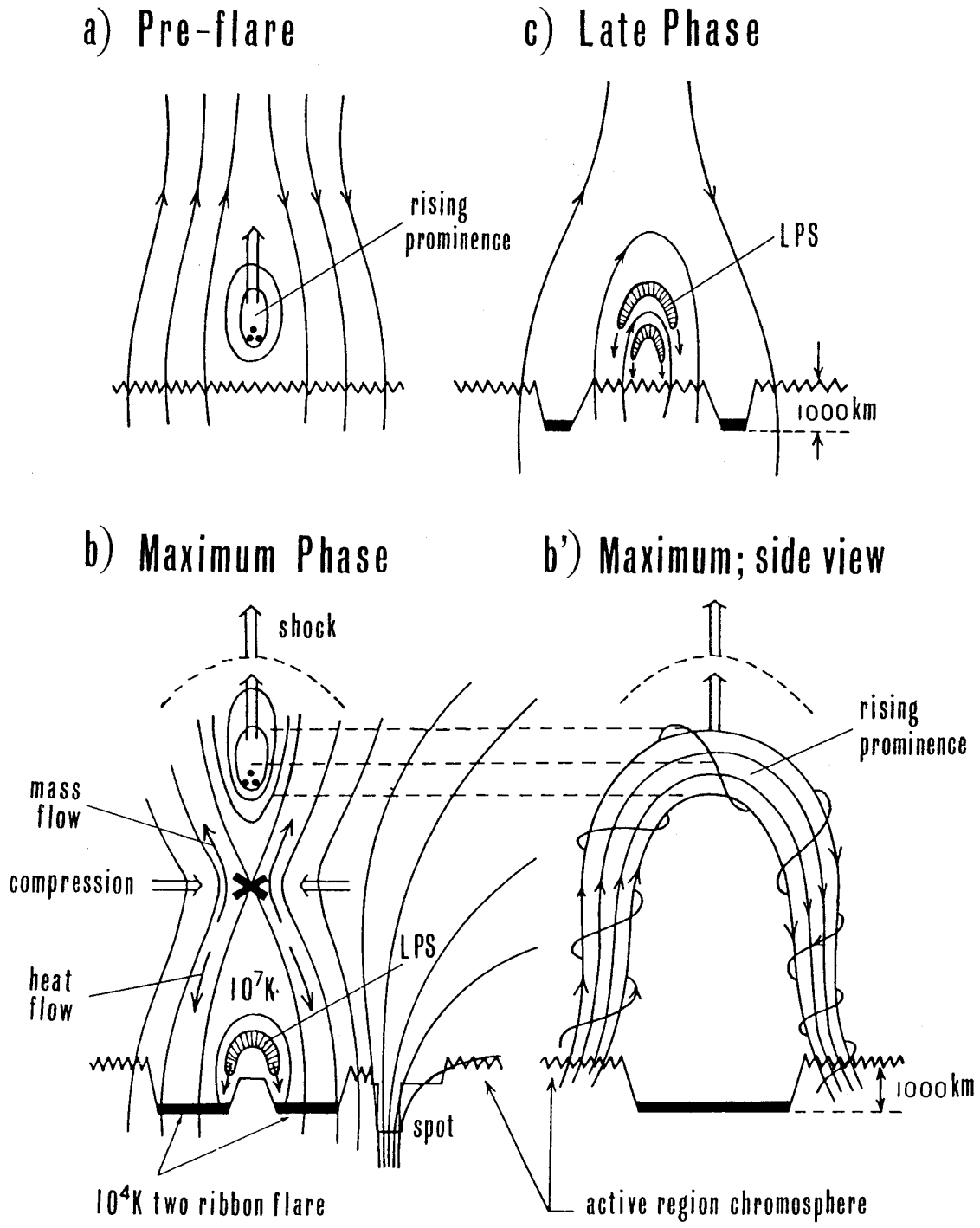

Figure 1.3 A classical flare model proposed by Hirayama (1974), which starts from a erupting prominence (a), triggers X-point reconnection beneath an erupting prominence (b), shown in sideview (b'), and leads to the formation of the two ribbon structure and the postflare loop prominence system (c).

$$\varphi_{rec} = \int E_{rec} dl = \frac{\partial}{\partial t}(\int\int B_n dA) \tag{1.3}$$

$$\psi_{rec} = \int \varphi_{rec}(t) dt \tag{1.4}$$

where dl is the length along the reconnecting current sheet, and dA is the newly brightened flare ribbon area at each time instant.

However, Aly (1991) and Sturrock (1991) found that there is an important energy constraint of this Standard model. They numerically studied a process with a closed force-free arcade system converted into an open field configuration and figured that there is contained more magnetic energy in a completely open field than a completely closed field. This energy constraint from closed to open field configuration is referred as Aly-Sturrock constraint.

The Emerging Flux Model

The flare model proposed by Heyvaerts et al. (1977) is one of the most commonly accepted solar eruption models, which assumes that the magnetic flux tubes concentrated in active regions emerge from the convection zone into the solar atmosphere are due to buoyancy[3] instability. In this model, the closed flux tubes emerging upward and interacting with the existing overlying coronal field cause stresses to build up and accumulate energy in the coronal magnetic field. Eventually, the stress exceeds the threshold beyond which an equi-

[3]The magnetic buoyancy is the upwards directed force exerted on flux tubes whose effect is a rise of the flux tube as a whole.

librium cannot be maintained. As a result, the configuration becomes unstable and stored energy is released with the eruption of the coronal magnetic field.

In this model (see Figure 1.4), new magnetic flux emerges beneath the flare filament at preflare heating time and then continuously reconnects with the old flux and heats the current sheet between them. At the impulsive phase, the heated current sheet rises to a critical height and the disequilibrium triggers rapid current sheet expansion and particle acceleration. After that, the magnetic flux reaches a new equilibrium status with reconnection. There is a limitation for the feasibility of this model, namely the requirement of the existence of a stable current sheet before the onset of the flare. However, observation and simulation (Aschwanden 2005) indicate that the current sheets reconnect as soon as they are formed. Therefore, in principle this model can explain impulsive and compact flares only (Priest & Forbes 2000).

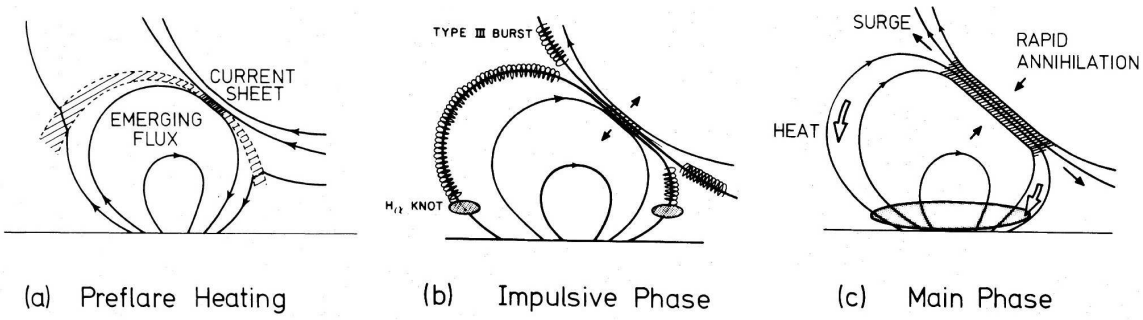

Figure 1.4 The emerging flux mechanism for a subflare (or simple loop flare). (a) Preflare phase; (b) Impulsive phase; (c) Main phase (courtesy of Heyvaerts et al. (1977)).

Break-out Model

The magnetic break-out model is developed by Antiochos et al. (1999), which is the leading theory for the initiation of a CME. Rather than a dipolar geometry, the original magnetic

field configuration of this model is a spherically quadrupolar double arcade (Figure 1.5). The magnetic reconnection occurs on top of the sheared arcade and subsequently removes the unsheared field above the low-lying, sheared, core flux near the magnetic neutral line, which then allows the field above the core flux to open up. The key point of the magnetic breakout model is the interaction of the multi-flux system, which allows the external and disconnected magnetic flux from the neighboring sheared arcade to assist in the opening process while bypassing the Aly-Sturrock constraint. Recent MHD simulation by Lynch et al. (2004) exhibits some features consistent with flare observation, such as the post-eruption flare loop and the chromospheric ribbon.

Flux Rope Catastrophic Model

Forbes & Priest (1995) developed this flare model in which the force-free magnetic field evolution passes a critical point, then the system becomes unstable and a filament eruption is triggered. The essential background field is a biopolar arcade embedded in the photosphere. The coronal magnetic field is described as the well accepted force-free field and the continuous converging flows serve as the driver mechanism. As the mass flow in the photosphere brings the magnetic field upward, the two photospheric field sources are pushed close to one another and then the magnetic field lines of opposite polarity reconnect. This fully analytical 2-D model is able to yield reasonable amounts of energy favorable for flares and CMEs, and demonstrates quantitatively how a loss of magnetic equilibrium leads to a rapid energy release. However, the typically observed photospheric converging flows may be too slow or randomly oriented to constitute a realistic driver of the eruption.

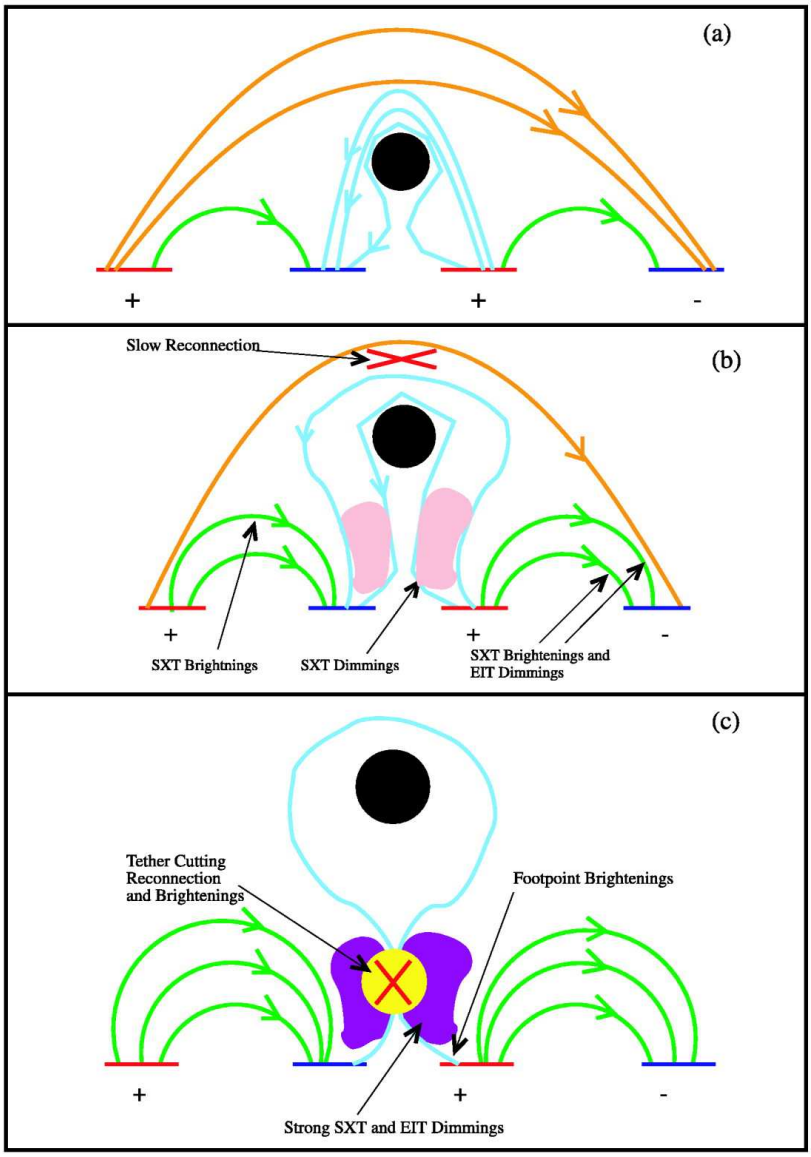

Figure 1.5 2-D schematic of the observed evolution in the quadrupolar region before and during the explosive phase of the eruption, interpreted as slow breakout leading to the onset of the explosive phase (courtesy of Sterling & Moore (2004)).

The Two Flux Loop Model

Melrose (1997) proposed a theoretical 3-D solar flare model, in which the flare energy is the magnetic energy released when two current-carrying flux loops reconnect to form two new current-carrying flux loops between the original four FPs. The fundamental assumption is that the magnetic flux and the electric current are transferred during the reconnection, while the constraint is the flux and the current are conserved at each FP. Therefore, the magnetic reconnection processes only change the current path, while the net current flowing in and out the corona remains fixed. The change of the magnetic energy is calculated in specific configuration of the spots (FPs of the loops). Aschwanden et al. (1999) estimated the transferable flare energy in this model and Yurchyshyn et al. (2000) found that the estimated energy released according to this model in the November 5 1998 M8.4 flare is consistent with the Yohkoh (means Sunbeam in Japanese, known before launch as Solar-A) observations. In Melrose's model, energy release preferentially occurs when a positive polarity spot is near a negative polarity spot (so that one of the final loops is very small) and when the two initial loops are at a large angle to each other. The formation of a shorter loop implies that the current path moves closer to the photosphere.

Moore et al. (2001) investigated six solar eruptive events with sigmoidal bipolar structure and proposed an eruption model for bipoles having sigmoidally sheared and twisted core fields. This model accommodates confined explosions as well as ejective explosions. Figure 1.6 shows the key stages of the tether-cutting model (referred the magnetic fields involved in the reconnection are like tethers holding down the filaments). Before the explosion, the characteristic sigmoidal structure of the core field is formed by the two oppositely curved elbow regions. The two elbow arms are highly sheared along the middle

stretch of the neutral line where the filament is suspended. The field between the two elbow arms are prone to reconnection, when they come into contact and push against each other. Once the two crossed arms are beginning to reconnect, there are two sets of newly connected field lines existing from the reconnection site. One set of the field lines connects the far ends of the two elbows and form a rising twisted flux rope. The other set of the field lines moves downward to form short sheared new loops low over the neutral line. The explosion either ejects the erupting flux rope out of the initially closed bipole and opens the envelope field, or remains confined within the closed bipole. Fisher et al. (2012) computed the change in the Lorentz force implied by the change of observed magnetograms during solar flares, and suggest that based on the need to balance the outward momentum of the ejecta from the flares, solar eruptions should lead the coronal magnetic field to contract inward as an "implosion", which points to a more horizontal state of the photospheric magnetic field as well and hence a downward Lorentz force acting on the solar surface (Figure 1.7).

1.4 Flare-Related Rapid Changes on Photospheric Magnetic Fields

There are a number of models that can explain some aspects of observed properties of solar flares. One way or the other, most flare models contain a key component of Kopp-Pneuman's original theory to explain two-ribbon flares: flare ribbon emissions are due to magnetic reconnection of overlying arcade fields that are opened by the erupting flux ropes, and the ribbons move away from the magnetic polarity inversion line (PIL) as successive reconnections occur at higher and higher latitudes (Kopp & Pneuman 1976). This and modified models of this kind tend to predict that the dense, high-β photosphere with line-

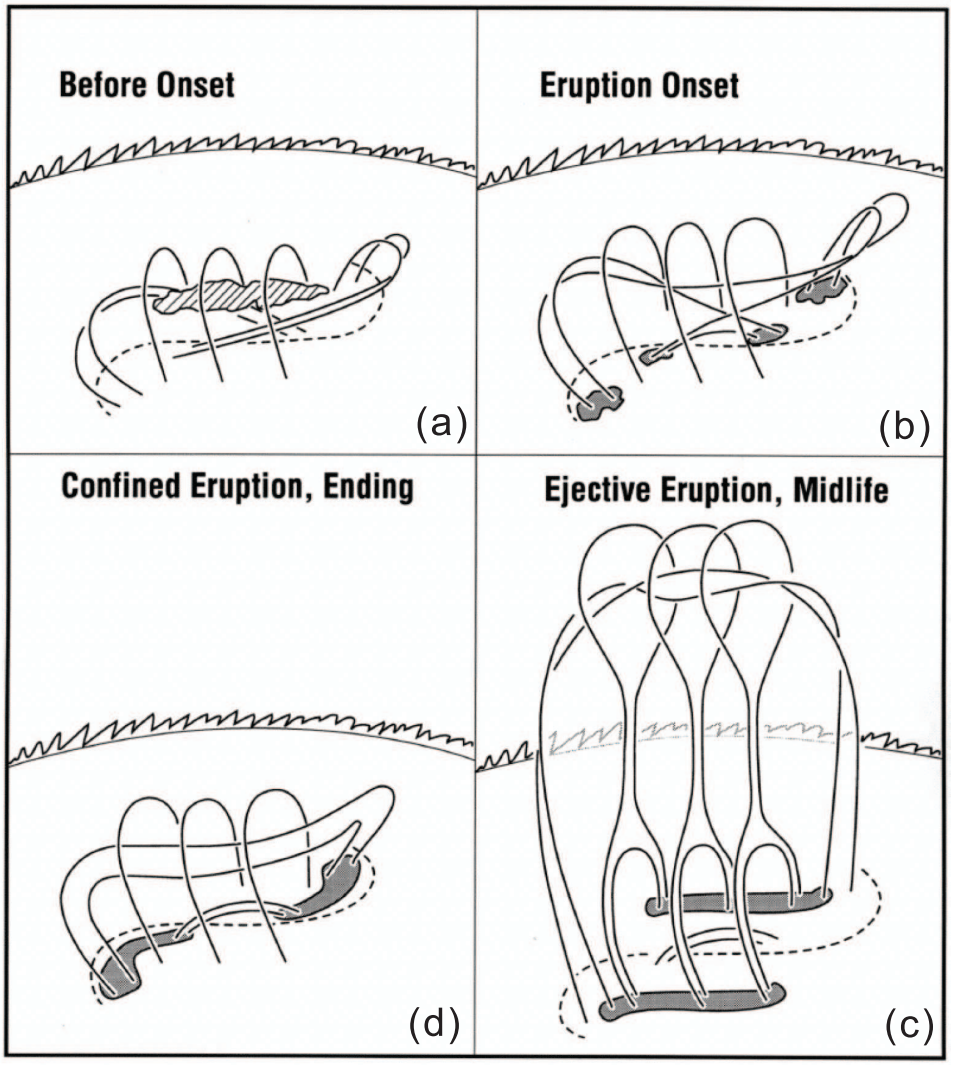

Figure 1.6 The dashed curve is the photospheric neutral line, the dividing line between the two opposite-polarity domains of the bipole's magnetic roots. The ragged arc in the background is the chromospheric limb. The gray areas are bright patches or ribbons of flare emission in the chromosphere at the feet of reconnected field lines, field lines expected to be illuminated in SXT images. The diagonally lined feature above the neutral line in the top left panel is the filament of chromospheric temperature plasma that is often present in sheared core fields (courtesy of Moore et al. (2001)).

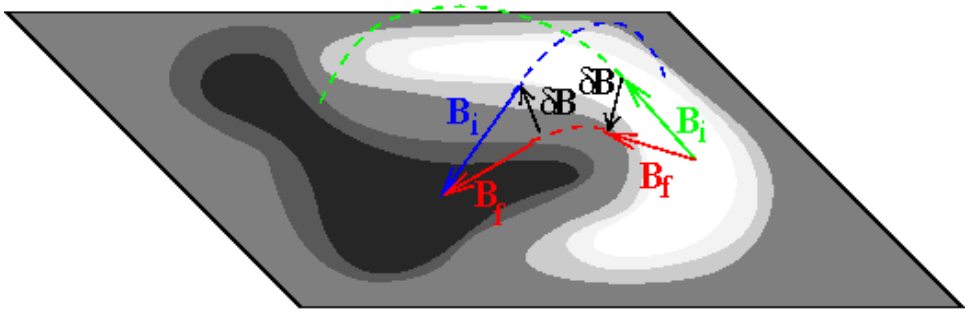

Figure 1.7 Sketch showing how the initial photospheric field vectors, denoted $\mathbf{B}_i$ tilt by $\delta\mathbf{B}$ as a result of coronal restructuring during a flare/CME, denoted here by changes in the connectivity of the coronal field (dashed lines) to final states $\mathbf{B}_f$ (courtesy of Hudson et al. (2008)).

tying photospheric magnetic field would not have rapid response to flares. However, more and more evidence demonstrates that photospheric magnetic fields can have permanent changes after flares (Kosovichev & Zharkova 2001; Wang et al. 2002, 2004a,b; Liu et al. 2005; Sudol & Harvey 2005; Wang et al. 2007; Wang & Liu 2010).

The irreversible changes of magnetic fields after flares is a solid observational phenomenon that has been identified for many events. Over a decade ago, the BBSO group discovered rapid and permanent changes of the photospheric vector magnetic fields associated with flares, which is also often accompanied by an increase of magnetic shear (Wang 1992; Wang et al. 1994; Cameron & Sammis 1999). Kosovichev & Zharkova (2001) studied high resolution Michelson Doppler Imager (MDI) magnetogram data of the 2000 July 14 "Bastille Day Flare" and located regions with permanent decrease of magnetic flux, which were related to the release of magnetic energy. Using 1 min cadence GONG data, Sudol & Harvey (2005) surveyed rapid and permanent changes of the line-of-sight (LOS) magnetic fields that are indeed associated with almost all the X-class flares studied. Earlier, the BBSO group published a number of papers describing the sudden appearance of unbal-

anced magnetic flux that is associated with flares (Spirock et al. 2002; Wang et al. 2002; Yurchyshyn et al. 2004). All these observations indicate that the flaring process, due to its magnetic nature, has a direct observable impact down to the photosphere. More recently, they presented a new observational result associated with rapid changes of sunspot structure associated with a substantial fraction of flares (Wang et al. 2007; Wang & Liu 2010). Such indirect evidence as the evolution of white-light (WL) sunspot structure (Wang et al. 2004a; Deng et al. 2005; Liu et al. 2005), changes in the LOS magnetic field (Wang & Liu 2010), and changes in the penumbral evershed flow (Deng et al. 2011), have also been found. Wang et al. (2012) presented the first solid evidence of flare-induced changes of the photospheric magnetic field using the SDO/HMI observations. Figure 1.8 displays the unambiguous enhancement of horizontal field at the surface which strongly suggested that the photospheric magnetic field could respond to the coronal field restructuring by tilting toward the surface.

However, from the viewpoint that observations and models should yield the same conclusions in all aspects, results reported in the literature thus far have not yet converged, especially regarding how the observed changes of photospheric magnetic fields due to flares could reconcile in the two-stage magnetic reconnection scenario, and more importantly, could be understood in the context of coronal magnetic field restructuring. Further investigation of individual events should be accumulated to advance the understanding of flaring processes.

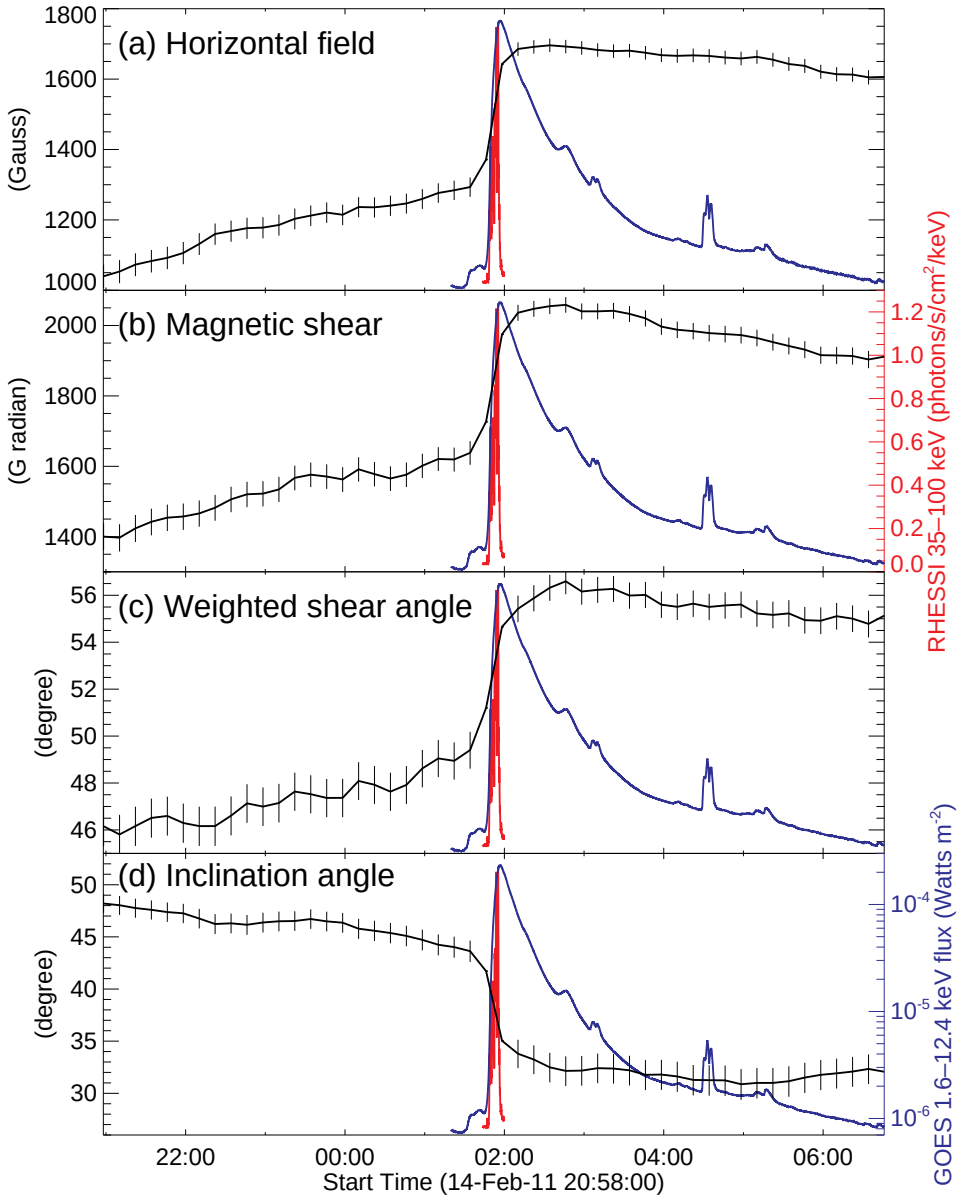

Figure 1.8 Temporal evolution of various magnetic properties of the enhanced region at the PIL, in comparison with the light curves of the RHESSI HXR flux in the 35-100 keV energy range (red) and GOES flux in 1-8 Å (blue). The vertical error bars indicate 3σ level (courtesy of Wang et al. (2012)).

1.5 Scientific Goal and Dissertation Outline

As mentioned, solar flares are explosive solar events that directly effect space weather. The solar magnetic field is the fundamental source of the phenomena of solar activity. Therefore, a deep understanding of the properties and behaviors of the solar magnetic field is essential to a space weather program. Although the evolution of the magnetic fields have been studied for a long time, the rapid changes of photospheric magnetic fields associated with flares were only discovered only recently. Furthermore, magnetic field changes in three-dimensions (3-D) are seldom explored due to lack of quantitative measurements of coronal fields. The scientific goal of this dissertation is to explore changes in the magnetic field properties associated with flares, e.g., magnetic inclination angle, transverse magnetic field, Lorentz force and FP motions, and to compare the flare observations with theoretical models and numerical simulations to understand the flare/CME scenarios.

The context of this work is arranged as follows:

Chapter 1: *Introduction.* This introductory chapter contains a general description of the Sun (section 1.1), an overview of solar active regions and sunspots (section 1.2), solar flares and theoretical models (section 1.3) and flare related rapid changes of photospheric magnetic fields (section 1.4).

Chapter 2: *Data Source and Data Processing Tools.* In this chapter, a description of many ground and space based instruments which are the primary data source of this dissertation is given. Data processing tools and relevant definition and calculation of magnetic parameters are also explained.

Chapter 3: *Rapid Changes of Magnetic Setting in Flare-Productive Active Regions.* This chapter contains the detailed study of rapid changes of magnetic field structure and properties associated with three major flares. The main results have been published in *Science in China Series G: Physics Mechanics and Astronomy, 2009, 52, 1702* and *New Astronomy, 2011, 16, 470*.

Chapter 4: *Comparison Between Simulation and Observation.* In this chapter, a comparison between the numerical MHD simulation of solar eruptions and the observations has been carried out to investigate the flare-associated change of magnetic settings. The main results have been published in *Astrophysical Journal Letters, 2011, 727, 19*.

Chapter 5: *3-D Emerging Magnetic Structure of Active Region 11158 Leading to a Flare on Feb 15 2011.* In this chapter, the long-term magnetic field evolution of NOAA active region 11158 during five days from February 12 to 16, 2011 has been studied and a model of emerging twisted flux rope has been proposed to interpret the observational result.

Chapter 6: *Radio Emission from Acceleration Sites of Solar Flares.* In this chapter, two competing electron acceleration models for radio emission from acceleration sites of solar flares have been calculated. Certain observational differences have been discovered. The main results have been published in *Astrophysical Journal Letters, 2009, 701, 52*.

Chapter 7: *Summary of the Dissertation.*

CHAPTER 2

DATA SOURCES AND DATA PROCESSING TOOLS

The 3-D magnetic topology of active regions from the photosphere to the corona is of fundamental importance to the understanding of the energy storage and release processes that account for flares and CMEs. To investigate the 3-D magnetic topology, the information on the 3-D magnetic field is needed, which is not directly accessible from observations but can be reconstructed using a technique called nonlinear force free (NLFF) coronal field extrapolation. The unique opportunity to study the magnetic configuration comprehensively is obtained now, as the high cadence, full disk vector magnetograms from the newly launched SDO mission, the unprecedented vector magnetogram data obtained from the Hinode mission, the more than 8 years archive of vector magnetograph observations at BBSO covering the maximum of solar cycle 23. Last but not least, the tools for NLFF coronal magnetic field extrapolation have matured.

2.1 Data Sources for Current Study: Hinode/SDO/BBSO

• *Solar Dynamics Observatory (SDO)*

The Solar Dynamics Observatory (SDO) launched on February 11, 2010, was the first mission for NASA's Living With a Star (LWS) Program. It is designed to advance the knowledge of solar activity and its influence on Earth and near-Earth space, by studying the solar atmosphere with high resolution and high cadence data at many wavelengths simultaneously. Three instruments onboard SDO deliver a huge number of images in a continuous data stream. The instruments are: (1) Atmospheric Imaging Assembly (AIA),

(2) Extreme Ultraviolet Variability Experiment (EVE), and (3) Helioseismic and Magnetic Imager (HMI). The former two use multiple (E)UV wavelengths to image the Sun's photosphere, chromosphere, transition region, corona and flaring region. HMI is an instrument designed to study oscillations and the magnetic field at the solar surface, i.e., photosphere, which extends the capabilities of the SOHO/MDI instrument with continuous full-disk coverage at 6173 Å with higher spatial resolution ($1''$) and temporal cadence (90 s) vector mangetograms. HMI observations expand current data-base significantly because of its full disk coverage. HMI vector magnetograms are used to investigate the longterm evolution of NOAA active region 11158 in Chapter 5.

• *Hinode*

Hinode, formerly known as Solar-B, is the follow-up to the Yohkoh mission (Tsuneta et al. 2008) to explore the Sun. This mission contains a coordinated set of optical, X-ray, and EUV telescopes. The 0.5 meter Solar Optical Telescope (SOT) consists of Broadband Filter Imager (BFI) and Narrowband Filter Imager (NFI). The field of view (FOV) of SOT is about $300'' \times 160''$, while the angular resolution is about $0.2''$ and the cadence is 2 minutes or less. The BFI produces photometric images with broad spectral resolution in 6 bands, i.e., G-band, CN band, CaII H line and three continuum bands, at the highest spatial resolution available from the SOT ($0.0541''$/pixel) and at a rapid cadence (<10 s) over a $218'' \times 109''$ FOV. The spectro-polarimeter (SP) provides a spectral resolution about 30 mÅ. The filter-based observation and SP observation are complementary. While the magnetic fields are measured in high cadence by NFI, high precise polarization measurements and spectral diagnosis have been provided by the SP observation. Combination of two data

sets obtained, for the first time, a continuous series of high-precision vector magnetograms, Dopplergrams, and filtergrams with sub-arcsecond resolution. Hinode has been operated for almost five years after its launch on September 2006 and has obtained unprecedented data. The strength of the Hinode observations is not only the high quality of the data, but also its uninterrupted coverage of active regions with high cadence. However, some hardware difficulty in Hinode/NFI prevents the high cadence vector magnetogram observations until now. Hinode/SP vector magnetograms are the key data set for this dissertation.

• *Big Bear Solar Observatory (BBSO)*

Big Bear Solar Observatory (BBSO) is a ground-based observatory which is capable of making high-resolution observations. It is well known for its high resolution Hα full disk system with one minute cadence. Meanwhile, BBSO started operation of Digital Vector Magnetograph (DVMG) in 1999 after many years of observations with Video Magnetograph. The data were obtained by a filtergraph-based system. It used the Ca I line at 6103 Å. The bandpass of the birefringent filter is 1/4 Å. The FOV of the instrument is $360'' \times 360''$ and the spatial resolution is $0.6''$ per pixel (Spirock et al. 2002). The cadence is typically 1 minute for a complete set of Stokes I, Q, U, V. There is no other vector magnetograph system with one-minute cadence that is operating routinely. The complete set of vector magnetograms during the maximum of solar cycle 23 consisting of over 100 events have been accumulated. Recently, BBSO has installed its 1.6 m clear aperture new solar telescope (NST) and first light has been attained at the Nasmyth focus.

2.2 Data Processing Tools: Ambiguity Resolution and NLFF Magnetic Field Extrapolation

The understanding of the 3-D magnetic configuration and its evolution would lead to a fundamental improvement of the knowledge about solar explosive phenomena. In order to streamline the analysis of the vector magnetogram data, data processing tools, including the 180° ambiguity resolution and NLFF coronal magnetic field extrapolation, have been developed and implemented.

The 180° azimuthal ambiguity in the transverse magnetograms is resolved using the "minimum energy" algorithm that simultaneously minimizes both the electric current density J and the field divergence $|\nabla \cdot \mathbf{B}|$ (Metcalf 1994). Minimizing $|\nabla \cdot \mathbf{B}|$ gives a physically meaningful solution and minimizing the J provides a smoothness constraint. A magnetogram is first broken into small sub-areas to compute a force free α parameter. Then a linear force-free field is effectively constructed with which to infer the vertical gradients needed to minimize the divergence. Since the calculation of J and $|\nabla \cdot \mathbf{B}|$ involves derivatives of the magnetic field, the computation is not local, the number of possible solutions is huge, and the solution space has many local minima. The "simulated annealing" algorithm (Kirkpatrick et al. 1983) is used to find the global minimum. This "minimum energy" algorithm is the top-performing automated method among state of the art algorithms used for resolving the 180° ambiguity (Metcalf et al. 2006).

In this study, NLFF coronal magnetic field extrapolation has been applied to construct the 3-D magnetic field. Extrapolating the coronal magnetic field from the photospheric vector magnetogram data is a complex task, primarily because the observable photospheric field is intrinsically inconsistent with the force-free field assumption. In the

measured region, the plasma β in the photosphere is of the order of one and the pressure and gravity forces are not negligible. However, in the corona, the plasma $\beta \approx 10^{-4}$ and consequently the magnetic field should be close to force-free in a stationary situation. To deal with this problem, Wiegelmann et al. (2006) developed a preprocessing procedure that refines the observed non-force-free data towards suitable boundary conditions for the force-free extrapolation. The preprocessing routine minimizes a functional $L_{prep} = \mu_1 L_1 + \mu_2 L_2 + \mu_3 L_3 + \mu_4 L_4$. The L_1 and L_2 terms contain force-free and torque-free consistency integrals, the L_3 term controls how close the preprocessed data are compared to the original magnetogram (noise-level), and the L_4 term controls the smoothing. A strategy on how to choose the parameters μ_i was described by Wiegelmann et al. (2006). The preprocessing method described above removes the net force and torque from the photosphere boundary, and hence provides an improved input for the subsequent NLFF field extrapolation (Metcalf et al. 2008).

Schrijver et al. (2006) and more recently Metcalf et al. (2008) quantitatively evaluated the performance of several state-of-art NLFF field extrapolation algorithms in comparison with some analytically known NLFF field solutions. Particularly, the numerical solution used by Metcalf et al. (2008) includes realistic photospheric Lorentz forces and several interesting topological features one expects to see in the solar atmosphere, such as a coronal null, a separatrix surface, and a S-shaped flux bundle. It was found that the optimization algorithm, originally proposed by Wheatland et al. (2000) and implemented by Wiegelmann (2004), combined with the preprocessing procedure performs well in reconstructing the coronal magnetic field.

To extrapolate the NLFF field from the photospheric vector magnetogram, Wiegel-

mann's multigrid version of the optimization code has been applied. The "multigrid" means that computation is carried out serially on a number of different horizontal grid scales. The solution from the coarser grid is interpolated into finer grids as the initial state for the next, finer solution (Wiegelmann 2004). This method involves minimizing a joint measure (L) for the normalized Lorentz force and the divergence of the field throughout the volume of interest V:

$$L = \frac{1}{V}\int_V [\omega_f(\mathbf{r})B^{-2}\,|(\bigtriangledown \times \mathbf{B}) \times \mathbf{B}|^2 + \omega_d(\mathbf{r})\,|\bigtriangledown \cdot \mathbf{B}|^2]dV \tag{2.1}$$

where $B = |\mathbf{B}|$, and ω_f and ω_d are weighting functions for the force and divergence terms, respectively. The weighting functions ω_f and ω_d are position-dependent. Both of them are chosen to be 1.0 in the center of the computational box and drop to 0 with a cosine profile in a buffer boundary region towards the side and top boundaries.

2.3 Definition and Calculation of Magnetic Parameters

To study changes in the magnetic field topology associated with eruptive events in both observational and simulated data, several quantities and properties of magnetic field must be defined.

2.3.1 Calculation of Magnetic Inclination Angle

From an observational point of view, the magnetic inclination angle θ is defined as the angle between the magnetic field lines and the local horizontal plane. It can be measured by:

$$\tan\theta = \frac{|B_z|}{\sqrt{B_x^2 + B_y^2}} \tag{2.2}$$

where B_x, B_y and B_z are x, y and z components of the magnetic fields in heliocentric-cartesian coordinates, respectively. A larger θ means that the magnetic field lines are more vertical to the horizontal solar surface. It is conceivable that to compare the magnetic inclination angle θ before and after flares would be the most straightforward way to describe the evolution of magnetic field line topology, with which to test the reconnection picture.

2.3.2 Calculation of Lorentz Force Change

Hudson et al. (2008) quantitatively assessed the force on the solar surface and interior resulting from the coronal field evolution required to release energy and made the prediction that after flares, the photospheric magnetic fields become more horizontal. The basic reason for this is that the release of magnetic energy leads to an implosion of the magnetic field. Given a change of the magnetic field just above the photosphere $\delta\mathbf{B}$, they estimate the change in Lorentz force per unit area acting on the photosphere as follows:

$$\delta f_z = (B_z\delta B_z - B_x\delta B_x - B_y\delta B_y)/4\pi \tag{2.3}$$

This idea was further exploited by Fisher et al. (2012) who noted that, based on Newton's 3rd law, the upward momentum of a CME should be balanced by a downward momentum so the fields in the surface are pushed to become flaten. Similar to what was presented by Hudson, Fisher and Welsch (2008), the Lorentz force integrated over the strong magnetic field area acting on the surface is downward, which has to be the same as

the upward Lorentz force needed to accelerate CME.

To adapt equation 2.3 in the numerical MHD simulation by Fan (2010), the relevant magnetic parameters are derived in the following. The electric current density is calculated by Ampère's law $\mathbf{J} = \frac{1}{\mu_0} \bigtriangledown \times \mathbf{B}$, where B is the magnetic field produced in the MHD simulation.

With Maxwell's equations and some vector manipulation, the Lorentz Force exerted on a volume V bounded by a surface S is given by (Franklin 2005, Eq (9.79))

$$\mathbf{F} = \int_V \mathbf{J} \times \mathbf{B} dV = \int_V \bigtriangledown \cdot \mathbb{T} dV = \oint_S \mathbb{T} \cdot \hat{n} d\mathbf{s} \tag{2.4}$$

where the Maxwell stress tensor $\mathbb{T}$ is defined as

$$T_{ij} = \frac{1}{4\pi}(B_i B_j - \frac{1}{2} B^2 \delta_{ij}) \tag{2.5}$$

and $\hat{n}$ is the unit vector normal to the surface.

A schematic illustration of the volume is shown in Figure 2.1. Under the assumption that the upper and side surfaces of the Gaussian volume V are sufficiently distant from the active region, the magnetic field integrated over these surfaces is negligible. The only surface that will contribute to the integration is the photosphere underneath the active region of interest. Fisher et al. (2012) deduced the radial and the horizontal components of the Lorentz force acting on the interior and the solar atmosphere in Cartesian coordinates:

$$F_r = \frac{1}{8\pi}\int_{A_{ph}} dS(B_r^2 - B_h^2) \tag{2.6}$$

$$\mathbf{F}_h = \frac{1}{4\pi}\int_{A_{ph}} dS B_r \mathbf{B}_h \tag{2.7}$$

Here, B_r and B_h are the radial and horizontal field component, respectively, and A_{ph} is the area of the photospheric domain containing the active region.

To address the change of Lorentz force, Fisher et al. (2012) take the time derivative of Equations 2.5 and 2.6, and integrate the temporal derivatives over a time duration δt. Then the change in the radial and horizontal components of the Lorentz force acting on the interior of the Sun is given by:

$$\delta F_r = \frac{1}{8\pi}\int_{A_{ph}} dS(\delta B_r^2 - \delta B_h^2) \tag{2.8}$$

$$\delta \mathbf{F}_h = \frac{1}{4\pi}\int_{A_{ph}} dS \delta(B_r \mathbf{B}_h) \tag{2.9}$$

Fan (2010) presented 3-D MHD simulations of the evolution of the magnetic field in the corona where the emergence of a twisted magnetic flux tube is driven at the lower boundary into a pre-existing coronal potential arcade field. The detailed description of this simulation and the comparison with observational data will be discussed in Chapter 5. The MHD 3-D simulation is carried out in a spherical domain. To get the Lorentz force in spherical coordinates, the area element in term of r, θ, and ϕ is interpreted as:

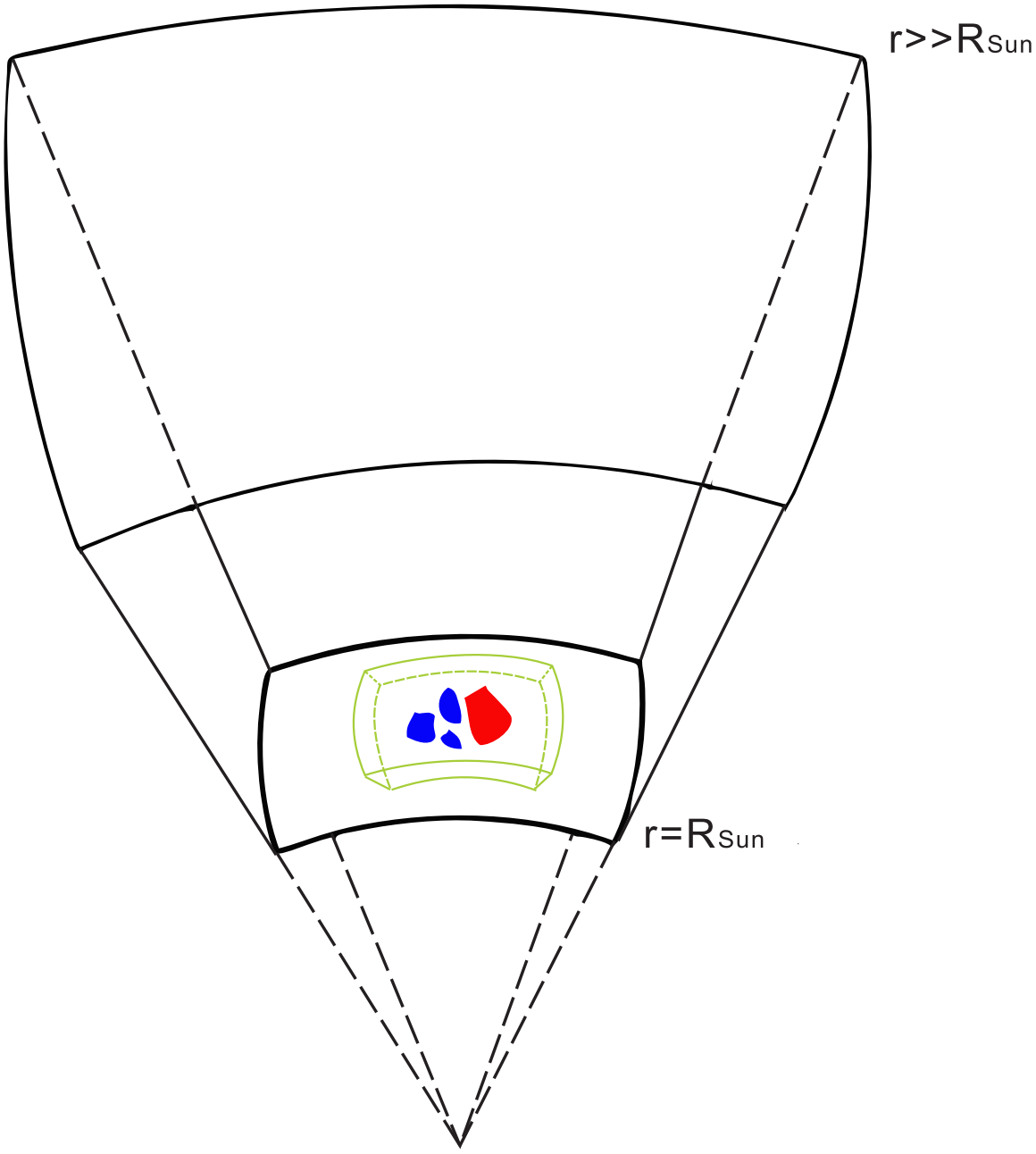

Figure 2.1 Schematic illustration of the Gaussian volume in which a bipolar active region is included.

$$ds = r^2 sin\theta d\theta d\phi \tag{2.10}$$

Then the components of the net Lorentz force are computed as

$$\delta F_r = \frac{1}{8\pi}\int_{A_{ph}} (B_r^2 - B_\theta^2 - B_\phi^2) r^2 sin\theta d\theta d\phi \tag{2.11}$$

$$\delta F_\theta = \frac{1}{4\pi}\int_{A_{ph}} (B_r B_\theta) r^2 sin\theta d\theta d\phi \tag{2.12}$$

$$\delta F_\phi = \frac{1}{4\pi}\int_{A_{ph}} (B_r B_\phi) r^2 sin\theta d\theta d\phi \tag{2.13}$$

Considered another small Gaussian volume shown as the green lined box in Figure 2.1, in which only a thin layer of the photospheric portion of the active region is considered, the contribution from the upper surface to the integrations on Equations 2.11, 2.12, and 2.13 could not be neglected. Note that the layer could be made as thin as possible so that the integration on the sides of this Gaussian volume is negligible. In this study, level 1 and level 3 in radial direction of the simulation domain are selected as the bottom and upper surfaces, respectively. The detailed description of the simulation is shown in Section 4.2. The Lorentz forces exerted on this Gaussian volume near photosphere are as follows,

$$\delta F_r = \frac{1}{8\pi}\int_{level1}(B_r^2 - B_\theta^2 - B_\phi^2)r^2 sin\theta d\theta d\phi - \frac{1}{8\pi}\int_{level3}(B_r^2 - B_\theta^2 - B_\phi^2)r^2 sin\theta d\theta d\phi \tag{2.14}$$

$$\delta F_\theta = \frac{1}{4\pi}\int_{level1}(B_r B_\theta)r^2 sin\theta d\theta d\phi - \frac{1}{4\pi}\int_{level3}(B_r B_\theta)r^2 sin\theta d\theta d\phi \tag{2.15}$$

$$\delta F_\phi = \frac{1}{4\pi}\int_{level1}(B_r B_\phi)r^2 sin\theta d\theta d\phi - \frac{1}{4\pi}\int_{level3}(B_r B_\phi)r^2 sin\theta d\theta d\phi \tag{2.16}$$

CHAPTER 3

RAPID CHANGES OF MAGNETIC SETTING IN FLARE-PRODUCTIVE ACTIVE REGIONS

A consistent pattern of changes in the sunspot structure associated with major flares has been discovered in recent studies. In this chapter[1], three flare events are analyzed and several interesting properties of the observed manifestations are found: (1) part of the peripheral penumbral region vanishes during flares, while the umbral cores and/or inner penumbral regions are darkened; (2) the transverse magnetic field increases rapidly near the magnetic PIL after flares; (3) the separation of the flare ribbons has a slow and a fast phase, and the flare hard X-ray emission appears in the later fast phase; (4) the Lorentz force near the flaring PIL drops after the flare. The evidences of remote brightenings and transverse magnetic field enhancement fit the tether-cutting reconnection model and the prediction by Hudson et al. (2008) and Fisher et al. (2012) that after a flare the magnetic fields near the umbral core turn to a more horizontal configuration.

3.1 Introduction

There are a number of models that can explain some aspects of observed properties of solar flares. One way or another, most flare models still contain a key component of Kopp-Pneuman's original theory to explain two-ribbon flares: flare ribbon emissions are due to magnetic reconnection of overlying arcade fields that are opened by the erupting flux ropes,

[1]This chapter is based on the following papers:
Li, Y., Jing, J., Tan, C., & Wang, H. 2009, Science in China Series G, 52, 1702.
Wang, P., Li, Y., Ding, M., Ji, H., & Wang, H. 2011, New Astronomy, 16, 470.

and the ribbons move away from the magnetic PIL as successive reconnections occur at higher and higher latitudes (Kopp & Pneuman 1976). This and modified models of this kind tend to predict that photospheric magnetic fields do not change after flares. However, more and more evidence demonstrates that photospheric magnetic fields can have permanent changes after flares (Cameron & Sammis 1999; Kosovichev & Zharkova 2001; Wang et al. 2002, 2004a,b; Liu et al. 2005; Sudol & Harvey 2005). It is noticeable that building on the Kopp-Pneuman scenario, many recent models of flares/CMEs exhibit signatures of two-stage magnetic reconnection. Taking the well received break-out model (Antiochos et al. 1999) as an example, the flares/CMEs occur in multipolar topologies in which reconnection between a sheared arcade and neighboring flux systems triggers the eruption, and this initial external reconnection could be related to remote brightenings (Liu et al. 2006). Another instance is the tether-cutting model, which was proposed by Moore & Labonte (1980) and further elaborated by Moore et al. (2001). This is one of the very few models that imply that the near-surface magnetic fields could have flare-associated changes, and it also proposes a two-step reconnection leading to flares/CMEs. At the eruption onset, the first stage reconnection near the solar surface produces a low-lying shorter loop across the PIL and a longer twisted flux rope connecting the two far ends of a sigmoid. The second stage reconnection begins when the formed twisted rope subsequently becomes unstable and erupts outward, distending the larger scale envelope field that overarches the sigmoid. The opened legs of the envelope field subsequently reconnect back to form an arcade structure and the ejecting plasmoid escapes as a CME. The tether-cutting model may potentially explain other observational facts including: (1) transverse magnetic fields at the flaring PIL increase rapidly following flares (Wang et al. 2004b); (2) penumbral decay occurs in the

outer border of a δ configuration, indicating that the peripheral field lines turn more vertical after flares (Liu et al. 2005; Wang et al. 2004a); (3) multiwavelength signatures (including hard X-rays) of preflare activities develop prior to the impulsive phase of flares (Fárník et al. (2003) and references therein); (4) hard X-ray (HXR) images show a change of the source morphology from a confined FP structure to an elongated ribbon-like structure after the flare maximum (Liu et al. 2007).

The irreversible changes in magnetic fields after flares is a solid observational phenomenon that has been identified for many events. Over a decade ago, the BBSO group discovered rapid and permanent changes of the photospheric vector magnetic fields associated with flares (Wang 1992; Wang et al. 1994; Cameron & Sammis 1999), which have already been confirmed by recent observations. Kosovichev & Zharkova (2001) studied high resolution MDI magnetogram data of the 2000 July 14 "Bastille Day Flare" and located regions with permanent decrease of magnetic flux, which were related to the release of magnetic energy. Using 1 min cadence GONG data, Sudol & Harvey (2005) surveyed rapid and permanent changes of the LOS magnetic fields that are indeed associated with almost all the X-class flares studied. Earlier, the BBSO group published a number of papers describing the sudden appearance of unbalanced magnetic flux that is associated with flares (Spirock et al. 2002; Wang et al. 2002; Yurchyshyn et al. 2004). All these observations indicate that the flaring process, due to its magnetic nature, has a directly observable impact down to the photosphere. More recently, they presented a new observational result of rapid changes of sunspot structure associated with a substantial fraction of flares (Wang et al. 2004a; Deng et al. 2005; Liu et al. 2005). In particular, Liu et al. (2005) studied the relationship between the change in δ spot structures and associated major flares for seven

events. The results are quite consistent for all the events: part of the penumbral segments in the outer δ spot structure decays rapidly after major flares; meanwhile, the umbral cores and/or inner penumbral regions around the flaring PIL become darker. The rapid changes, which can be identified in the time profiles of WL mean intensity, are permanent, not transient, and thus are not due to transient flare emission. To explain these observations, Liu et al. (2005) proposed a reconnection picture in which the two components of a δ spot become strongly connected after the flare. The penumbral fields change from a highly inclined to a more vertical configuration, which leads to penumbral decay. At the same time, the penumbral region near the flaring PIL becomes darker as a result of increasing transverse magnetic field components.

Recently, the two-stage nature of magnetic reconnection involved in major flares is further evidenced by observational studies. Xu et al. (2010) presented HXR observations of the 2003 October 29 X10 flare obtained with RHESSI (Lin et al. 2002), and identified two pairs of HXR conjugate FPs at the flare early impulsive phase that are shown to have different temporal evolutions. By carrying out magnetic sequence analysis, Qiu (2009) made a comprehensive study of the 2004 November 7 X2.0 flare and revealed that the flare ribbons first spread along then separate away from the PIL. Guo et al. (2008) and Cheng et al. (2010) found reconnection and brightening in the core field followed by the final eruption for the 2006 December 13 flare and the 2008 April 26 CME/flare, respectively. All these results strongly suggest that two distinctly separate reconnection processes could occur in succession during a single event. Theoretical progress in the study of magnetic reconnection made by Cassak et al. (2006) shows that slow and collisional reconnection in sheared magnetic fields in the corona can exist for a long time. When the dissipation

region becomes thinner and the resistivity drops below a critical value, fast, collisionless reconnection sets in abruptly, increasing the reconnection rate by many orders of magnitude in a very short time. It is possible that the contracting phase of flares, which is observed to be correlated with rapid unshearing and abnormal temperature structures of hard X-ray looptops of a number of flares (e.g., Ji et al. (2006); Shen et al. (2008)), corresponds to the first stage, while the ribbon expansion corresponds to the second stage.

In this chapter, three flare events that were well observed by BBSO and Hinode have been studied, with a focus on the flare-related photospheric magnetic field changes and the flare ribbon dynamics. The observational results are presented in the following sections and further discussion on the comparison with modeling is in Chapter 5.

3.2 The Change of Magnetic Field Associated with the X3.4 Flare of 2006 December 13

3.2.1 Data Sets

For this X3.4 event, the Hinode SOT vector magnetograms taken before and after the flare were used to study the changes of magnetic fields. This event occurred in NOAA active region 10930 with the peak GOES soft X-ray emission at 02:40 UT on 2006 December 13. The vector magnetograms and other thermodynamic parameters were obtained in two time bins, 20:30-21:33 UT on 2006 December 12 (before the flare) and 4:30-5:36 UT on 2006 December 13 (after the flare). Photospheric vector magnetograms were obtained from the Stokes profiles of the two magnetically sensitive Fe lines at 630.15 and 630.25 nm with a Milne-Eddington Stokes inversion (Kubo et al. 2008). The pixel resolution of the magnetograms is 0.16" pixel^{-1}. Combined with the corresponding G-band (430nm)

data obtained with BFI of SOT with a spatial resolution of ~ 0.2" and temporal resolution of 2 minutes, the decayed and the enhanced regions of the spot were identified. The 180° ambiguity in vector magnetograms was resolved with the "minimum energy" method (Metcalf 1994). Since the active region is not located at the center of solar disk, the projection effect was corrected with coordinate transformations. Next, to be consistent with the force-free assumption, the photospheric vector magnetograms were preprocessed with a preprocessing scheme developed by Wiegelmann et al. (2006) (see details in 2.2). Then these preprocessed vector magnetograms were used as the boundary conditions to extrapolate the coronal magnetic fields before and after the flare. The 3-D NLFF fields and the potential fields are computed with the "weighted optimization" method (Wheatland et al. 2000; Wiegelmann 2004) and a Green's function method (Metcalf et al. 2008), respectively.

3.2.2 Observational Analysis

Figure 3.1 compares the sunspot structures before and after the flare. The brightened or darkened areas in the difference image obtained by subtracting the preflare state from the postflare state in Hinode G-band (*bottom panel in the left column*) represent the decayed/enhanced penumbral regions. The dashed box marks a region where neither decay nor enhancement occurred. The two right panels show the temporal evolution of the mean G-band intensity in the decayed area (*top*) and in the enhanced area (*bottom*) during a 3.5 hr time period around the flare. The G-band intensity in the control region fluctuates and shows no obvious changes after the flare, while the G-band intensity in the decayed/enhanced region increases/decreases significantly after the flare.

After aligned the G-band images with the corresponding spectro-polarimeter (SP)

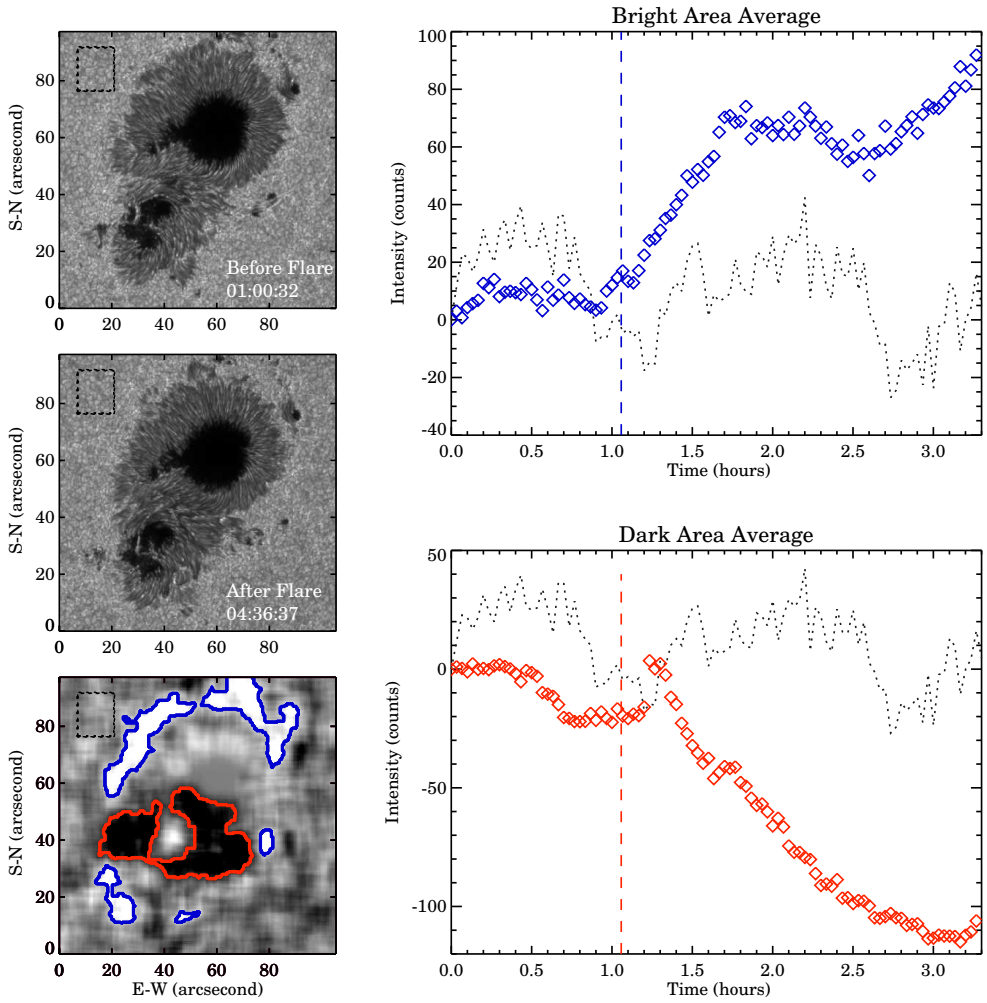

Figure 3.1 The left column shows Hinode G-band images taken before (*top*) and after the flare (*middle*), and their difference image (the post-flare image minus the pre-flare image;*bottom*). The FOV is about 100"×100". In the difference image, the brightened area and the darkened area are outlined with blue and red contours, respectively. The dashed black box indicates the control region where neither decay nor enhancement occurred. In the right column, *Top Panel:* Evolution of the mean G-band intensity of the decayed region comparing to the starting time 01:10 December 13, 2006; *Bottom Panel:* Evolution of the mean G-band intensity of the enhanced region. The dotted line shows the evolution of the mean G-band intensity of the control region. The vertical dashed lines indicate the flaring peak time of hard X-rays.

vector magnetograms, the changes of the photospheric magnetic parameters in the decayed and enhanced penumbral areas were studied. Figure 3.2 compares the pre-flare and the post-flare distributions of magnetic inclination angle $\theta(\theta = \tan^{-1}\frac{|B_z|}{\sqrt{B_x^2+B_y^2}})$, horizontal field strength in the decayed region(*top row*), the enhanced region (*middle row*) and the control region(*bottom row*). The mean values of these parameters before and after the flare are indicated by the vertical green and orange lines, respectively. The 95% confidence interval of each parameter is shown in the corresponding panel. Evidently, the inclination angle increases by $\sim 3.3^\circ$ after the flare in the decayed region, and decreases by $\sim 5^\circ$ in the enhanced region. The horizontal magnetic field strength within the centered enhanced region increased by 20% after the flare, meanwhile falls by 16% in the peripheral decayed region. In the control region, there is no distinct change in either magnetic inclination angle or the horizontal field strength.

The further comparison is the height variations of the magnetic inclination angle calculated in the pre- and post-flare 3-D NLFF fields. Using the 3-D NLFF fields (Figure 3.3). Figure 3.4 shows the magnetic inclination angle in the decayed (*top*), enhanced (*middle*) and control (*bottom*) regions as a function of altitude for the two time bins, 20:30-21:33 UT on 2006 December 12 (before the flare) and 4:30-5:36 UT on 2006 December 13 (after the flare). The decayed, enhanced and control regions are mapped upward from the surface to higher altitudes vertically. From the photosphere boundary to an altitude of ~ 40 Mm, the magnetic inclination angle in the decayed region increases after the flare. In the enhanced region, the angle deceases in all levels.

The altitude variation of magnetic inclination angle θ of the potential field is also plotted in Figure 3.4 as a reference. Beyond ~ 70 Mm, the field of both decayed and

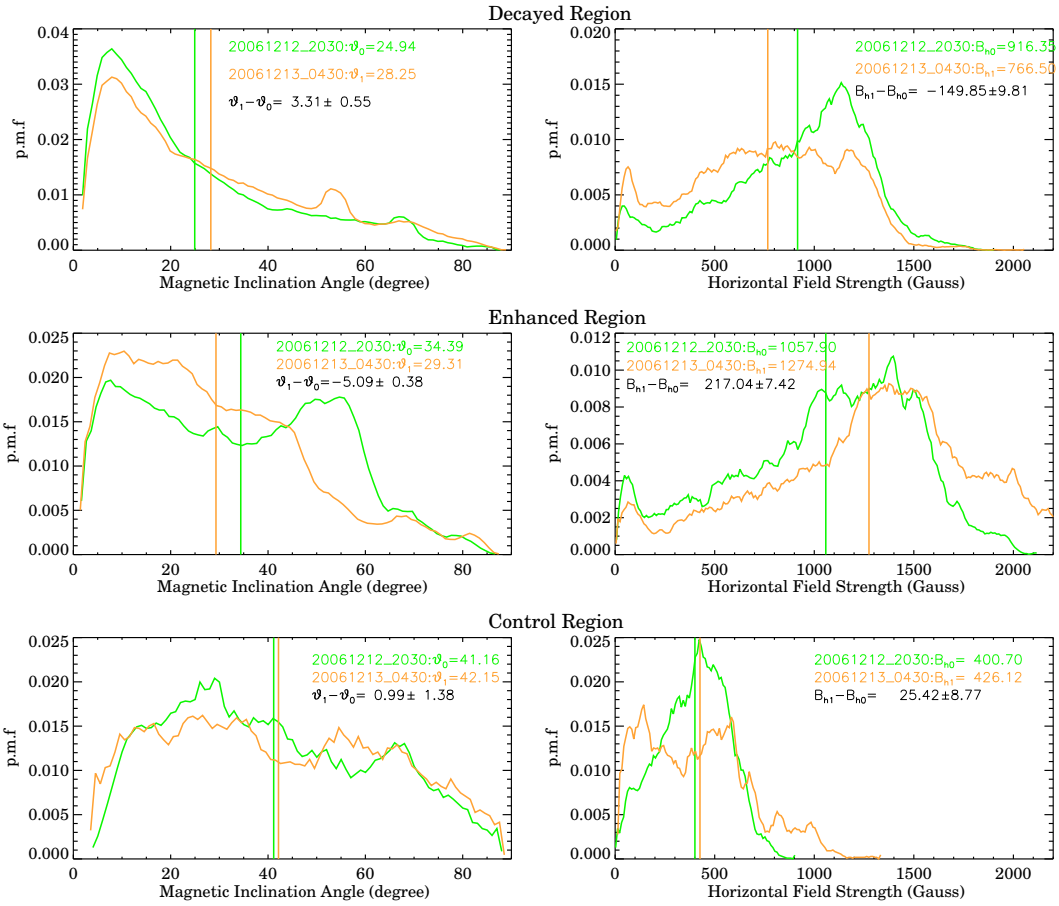

Figure 3.2 The pre-flare (*green lines*) and the post-flare (*orange lines*) distributions of magnetic inclination angle, horizontal field strength in the decayed (*top row*), the enhanced (*middle row*) and the control (*bottom row*) areas. The vertical green lines indicate the mean value of parameters before the flare, while the vertical orange lines indicate that after the flare. The 95% confidence interval of each parameter was shown in corresponding panel. p.m.f stands for probability mass function.

enhanced regions approach the potential state. The assumed line-tying lower boundary condition in the simulation implies the same potential field configuration before and after the flare. Note that as the observed LOS magnetogram changes, there is usually a corresponding change in the 3-D potential field. It is postulated that the change of potential field is contributed by gradual evolution of the active region during the 8-hour time gap between Hinode/SP observations. Furthermore, the difference in θ between the NLFF field and the potential field is more obvious in the enhanced region in comparison with the decayed region, suggesting that the result of the enhanced region is more meaningful. This is also consistent with observation and simulation to be described later: the field change is more evident in the enhanced region than the decayed region.

3.3 The Change of Magnetic Field Associated with X2.6 Flare of 2005 January 15

For this event, Liu et al. (2010) reported an asymmetric filament eruption. The asymmetric filament eruption is a kind of eruption with one point fixed and flare brightening propagates along the PIL together with the expansion/separation from the PIL, as reported by Tripathi et al. (2006). For this event, Liu et al. (2010) found that magnetic reconnection proceeds along the PIL toward the regions where the overlying field decreases with height more rapidly. The main goal here is to provide further evidence reflecting physical properties of the rapid photospheric magnetic field changes and the two-stage magnetic reconnection, especially, the physical mechanisms for initiating the filament eruption.

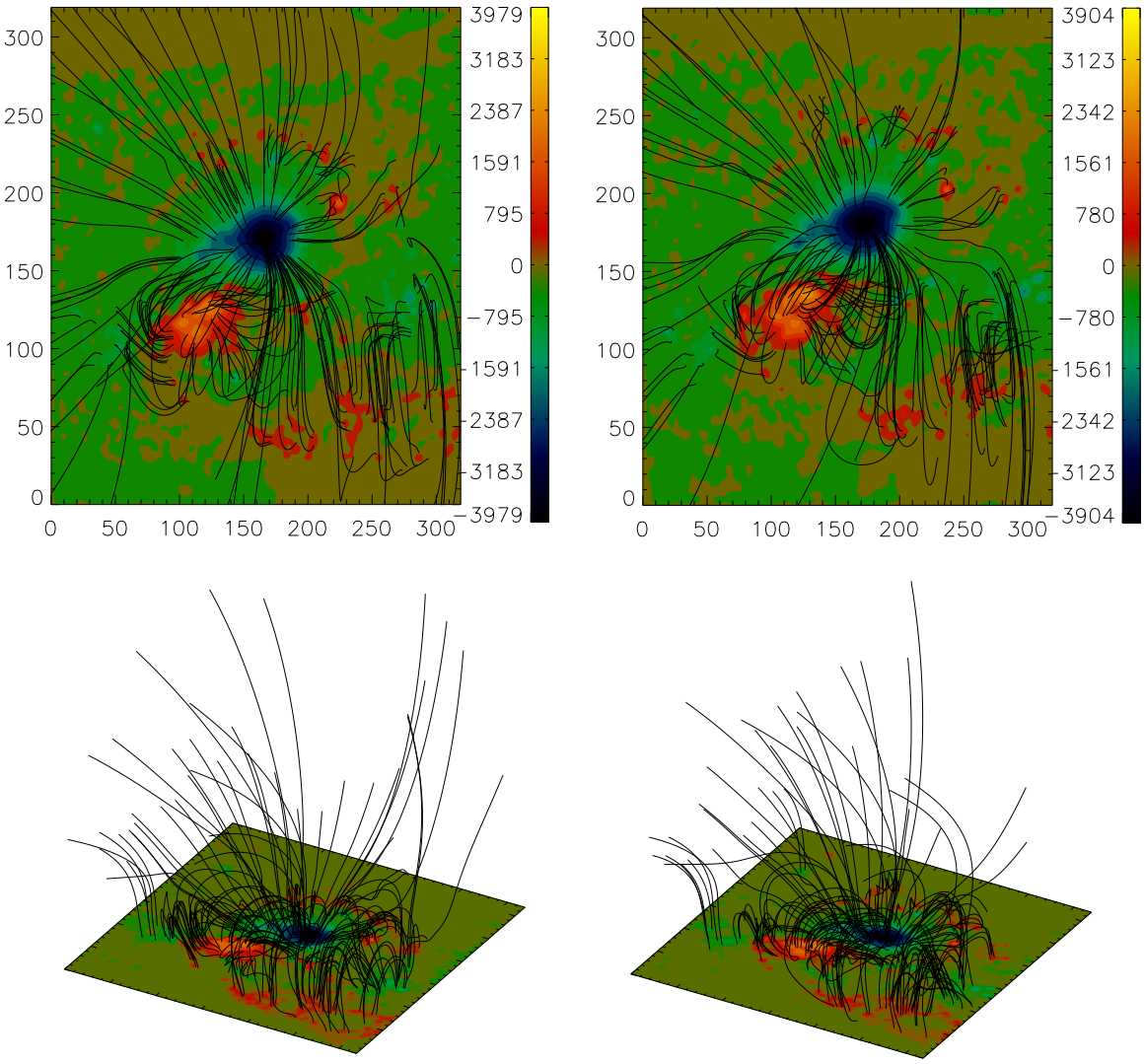

Figure 3.3 Visualizations of the NLFF magnetic fields over the active region before and after the X3.4 flare. Background shows LOS magnetograms taken before and after the flare. The FOV is 320"×320".

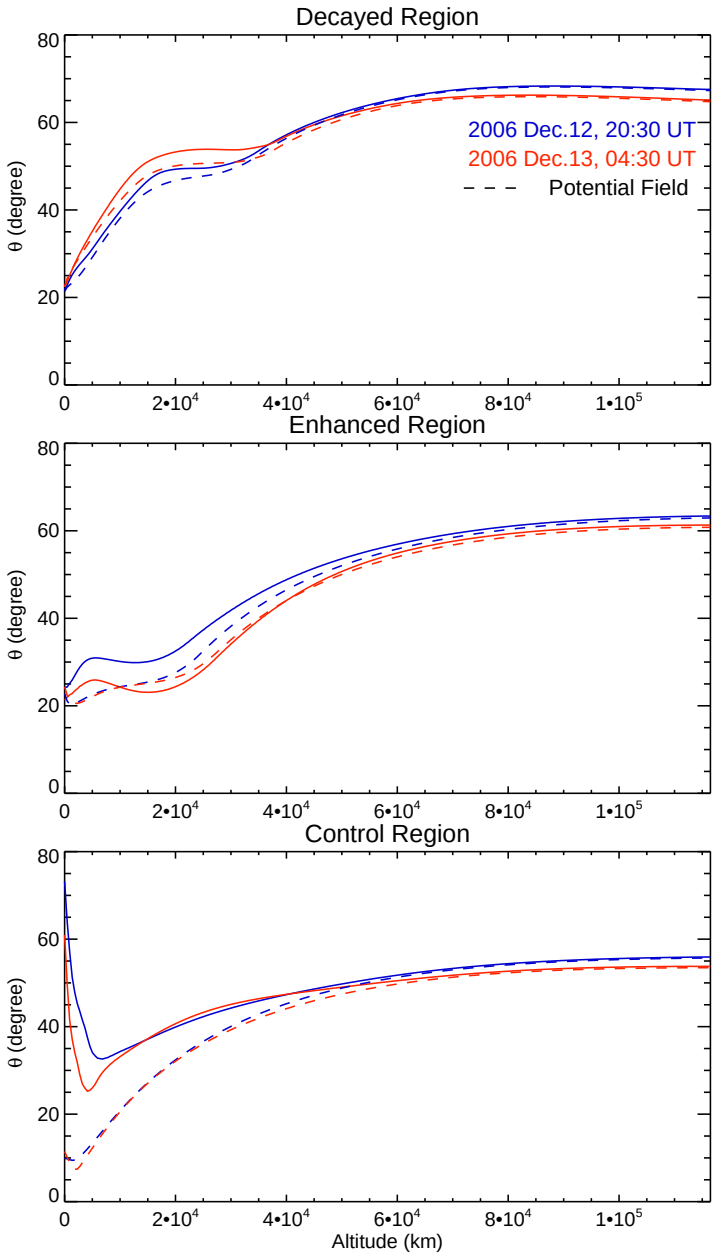

Figure 3.4 The mean value of magnetic inclination angle in the decayed *(top)*, the enhanced *(middle)*and the control *(bottom)* areas as a function of altitude for two time bins. *Blue*: Before the flare. *Red*: After the flare. Values were derived using NLFF extrapolation.

3.3.1 Data Sets

The source active region, NOAA 10720, produced many X-class flares in 2005 January. As BBSO routinely monitors the activity of the solar chromosphere, the X2.6 flare of January 15 that peaked at 23:02 UT in the GOES soft X-ray flux was fully covered by its full-disk Hα observation with a cadence of 1 min and a pixel scale of $\sim$ 1". Moreover, vector magnetograms were obtained by the DVMG system at BBSO with a field of view of about 300" $\times$ 300" targeted at this active region. The hardware of DVMG, consisting of a 1/4 Å band pass filter, a 12-bit 1024 $\times$ 1024 CCD camera, and three liquid crystals acting as polarization analyzers, has been described in detail by Spirock et al. (2002). Each complete set of Stokes data has typically a 1 min cadence and comprises four images: 6103 Å filtergram (Stokes I), LOS magnetogram (Stokes V), and the transverse magnetogram (Stokes U and Q) (Wang et al. 2002). For each of Q, U, V, the integration was applied over about 4s. The pixel scale of vector data is $\sim$ 0.6" after rebinning to increase the sensitivity of the magnetograms, which is approximately 2 and 20 Gauss for the LOS and transverse magnetic fields, respectively (Spirock et al. 2002; Wang et al. 2002). To fully utilize the vector magnetograms, the 180° azimuthal ambiguity in the transverse fields was resolved by using the "minimum energy" method (Metcalf et al. 2006) and the projection effects were removed by transforming the observed vector magnetograms to heliographic coordinates.

To understand the relationship between the evolution of magnetic fields and primary energy release sites, the time profiles as well as images of HXR emissions taken by RHESSI were used. The decayed and enhanced regions were identified by the difference images obtained with TRACE WL observation. Aligning images from different sources has been a challenging task. The pointing information of the RHESSI instrument was used, and the

BBSO data was aligned with the LOS magnetograms from MDI on board the Solar and Heliospheric Observatory by feature matching, the accuracy of which is estimated to be $\sim$ 5".

3.3.2 Observational Analysis

Permanent Changes of Photospheric Magnetic Fields after the Flare

There is excellent coverage of vector magnetic field observation to study this event in detail. Figure 3.5 shows a preflare vector magnetogram taken at 21:43 UT. The X2.6 flare mainly occurred in the tongue-shaped west part of the active region, where there are strongly sheared magnetic fields involving long-term flux emergence.

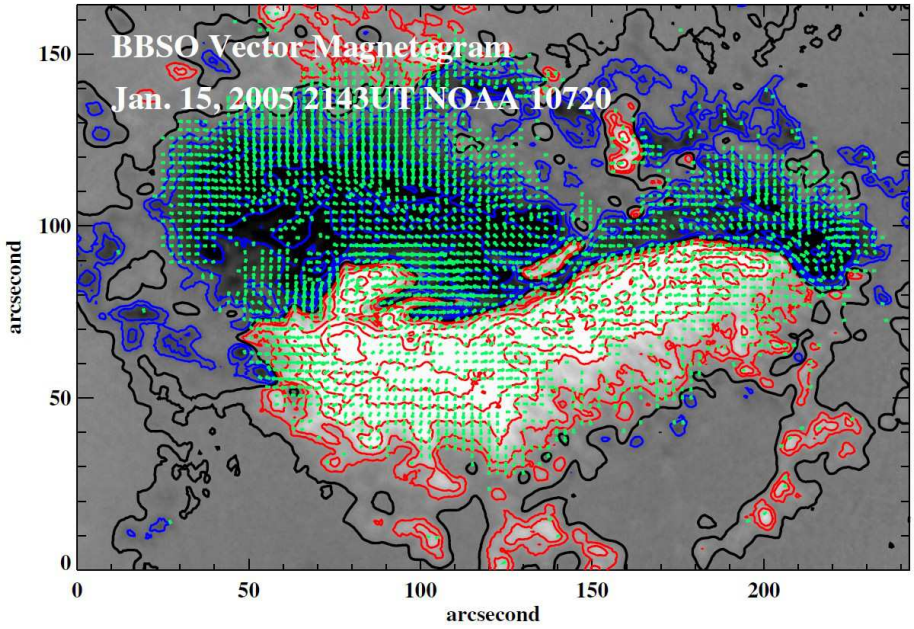

Figure 3.5 A BBSO vector magnetogram at 2005 January 15 21:43 UT before the X2.6 flare. Green arrows indicate the transverse fields. Red and blue contours are for negative and positive LOS magnetic field strength, respectively. The thick, solid black lines are the PILs of the LOS magnetic field.

The location of flare-related enhancement of transverse field strength is identified at

the flaring PIL by examining a time-lapsed movie compiled using transverse field strength. The bottom panel in Figure 3.6 shows the difference map of transverse field between the pre- and postflare states, and Figure 3.7 shows the time profile of the transverse field strength and the corresponding mean inclination angle in the most prominently enhanced area (indicated by the arrow in Figure 3.6). After the flare the mean transverse field suddenly increased from 450 to 550 Gauss in a section of PIL connecting HXR FP emissions, and the mean inclination angle decreased about by 5° accordingly. This kind of enhancement can be explained in one of two ways: either there is a rapid new flux emergence after flares (Wang et al. 2002), or the connectivity at flaring PIL is enhanced after flares. For this event, the former explanation can be rejected due to lack of evidence of increase of LOS flux right after the flare. On the other hand, the latter explanation could be linked to the change of magnetic connectivity in the first phase of the two-stage reconnection.

Flare Remote Brightening

Although flare energy release may mainly stem from its core emission, study of large-scale structure of flares can help to better understand the magnetic topology of the flaring active region. In a previous work, Liu et al. (2006) summarized the studies of remote brightening, which can be primarily due to hot particles traveling from the flare core to a remote site along large-scale magnetic field lines (Tang & Moore 1982; Kundu et al. 1983; Nakajima et al. 1985; Hanaoka 1999, e.g.). In this case, remote brightening can be an important tracer for such a large-scale magnetic field connecting the flare core and the distance place, which is also substantiated by the finding of subsequent formation of transient coronal holes (dimmings) above the remote brightening regions (Manoharan et al. 1996). In some other cases,

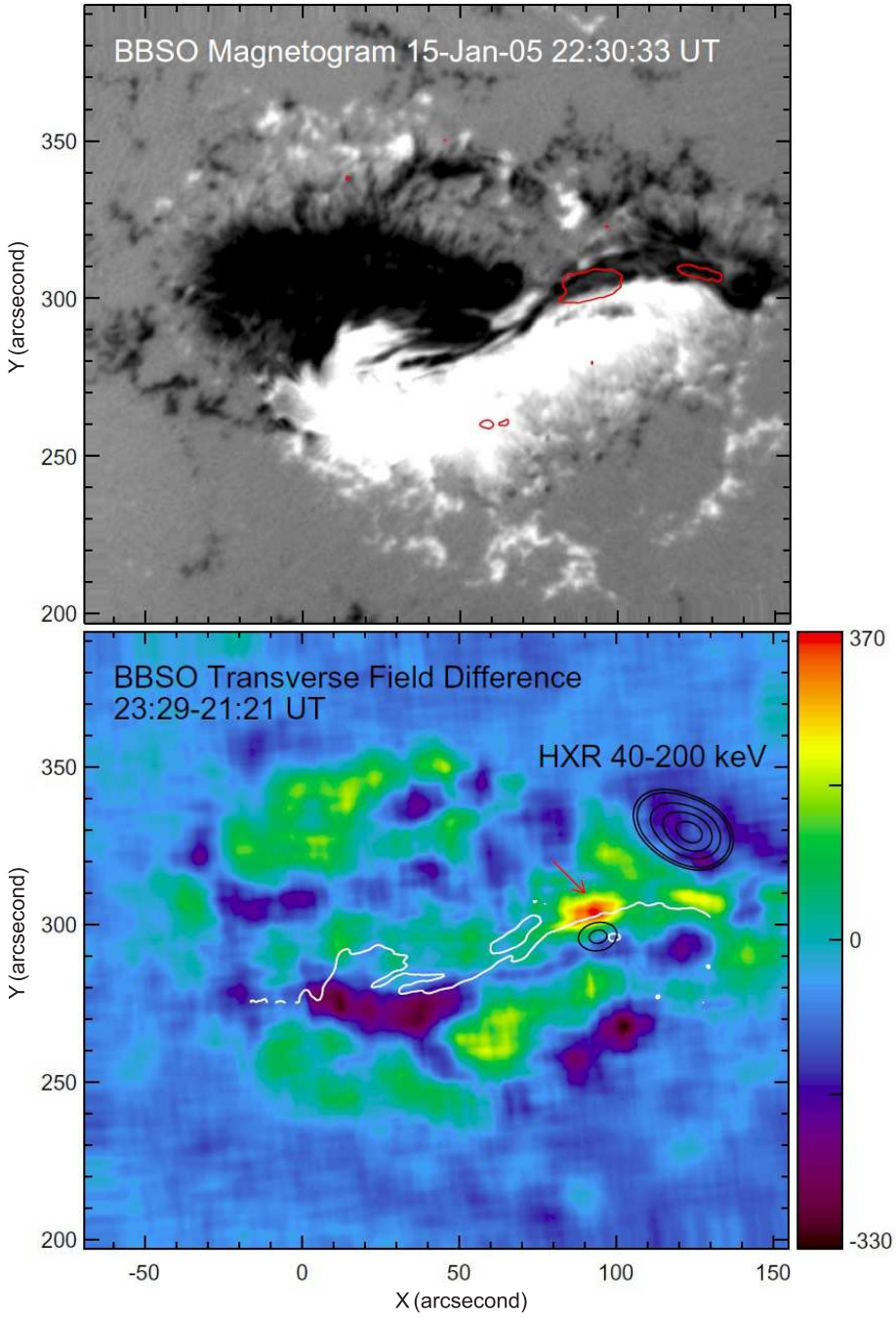

Figure 3.6 Top: BBSO LOS magnetogram before the X2.6 flare. Bottom: difference map of transverse field strength before and after the flare. Regions in *Red* indicate an increase of transverse field, with the most prominent area pointed by an arrow. The strongly enhanced regions are also outlined and superposed in the top panel. The cleaned RHESSI image was reconstructed using detectors 3-8 (9.8" FWHM resolution) and 60s integration time centered on 22:49:18 UT and is shown as contours at levels of 25%, 30%, 50%, 70%, and 90% of the maximum flux. The white line denotes the main PIL of this δ spot.

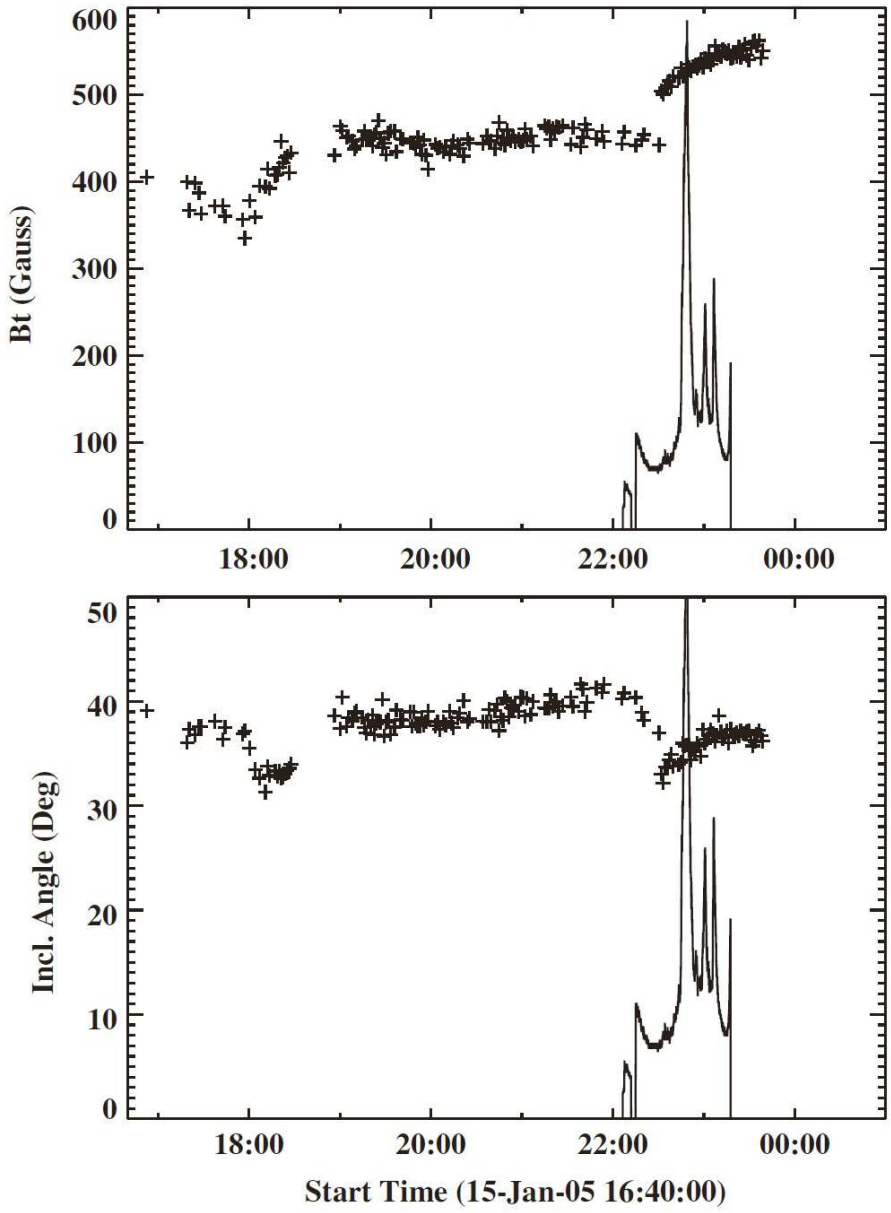

Figure 3.7 Transverse field strength (top) and corresponding inclination angle (bottom) as a function of time for the arrow pointed region in Figure 3.6. The 100-300 keV HXR light curve is over plotted. The mean transverse field strength suddenly increased from 450 to 550 Gauss in a section of PIL connecting HXR FP emissions; meanwhile, the mean inclination angle decreased about 5°.

remote brightenings can be interpreted as disturbances propagating outward from the flare site in the form of Moreton waves (Moreton & Ramsey 1960; Uchida 1974b,a). Observational analyses of remote brightenings have been advanced in recent years. Balasubramaniam et al. (2005) researched them as sequential chromospheric brightenings, which are observed to travel from the flare site outwards. Liu et al. (2006) made a detailed study of an X-class flare and found close correlation among flare initiation, Moreton wave, coronal dimming, and remote brightening. In short, the remote brightenings have been considered as the consequence of eruption that spreads toward the non-flaring regions.

Figure 3.8 shows the time sequence of Hα images across the flaring interval of the present event. Besides the two prominent flare ribbons, remote brightenings and their northward propagation are very evident. Three of the strongest patches are labeled as 1, 2, and 3 (see the image at 22:47:48 UT). What is striking is that the remote brightenings were launched $5-10$ min before the peak of HXR emission, which can be unambiguously recognized in Figure 3.9, where the time profiles of the Hα intensity of the three patches were compared to that of the HXR emission. With the ordinary remote brightenings in mind, this unusual temporal property leads to the conjecture that these Hα emitting patches have different physical implication and could stand for FPs corresponding to the initial stage of magnetic reconnection with respect to the subsequent onset of main flare HXR emissions.

In order to shed more light on the role of the remote brightenings, the position of a section of the main flare ribbon that has the highest speed of separation motion away from the flaring PIL is traced. This speed is closely associated with the magnetic reconnection rate of flares. Forbes & Priest (1984) supplemented the classical flare model with a

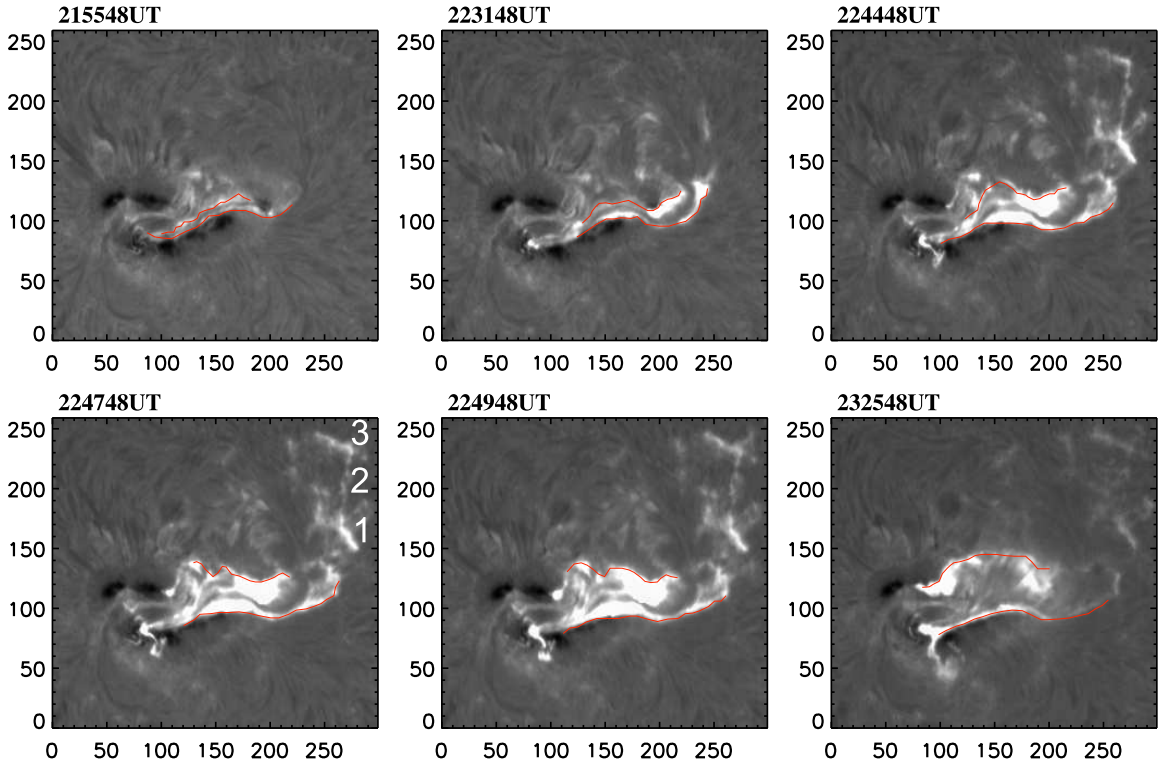

Figure 3.8 Time sequence of Hα images of the 2005 January 15 X2.6 flare. Three remote brightenings under discussion are marked as 1, 2 and 3. The images are centered on the point (80", 350") with solar west to the right and north up. The field of view is $\sim$ 320" $\times$ $\sim$ 260". The ribbons' moving fronts are marked by the over-plotted lines.

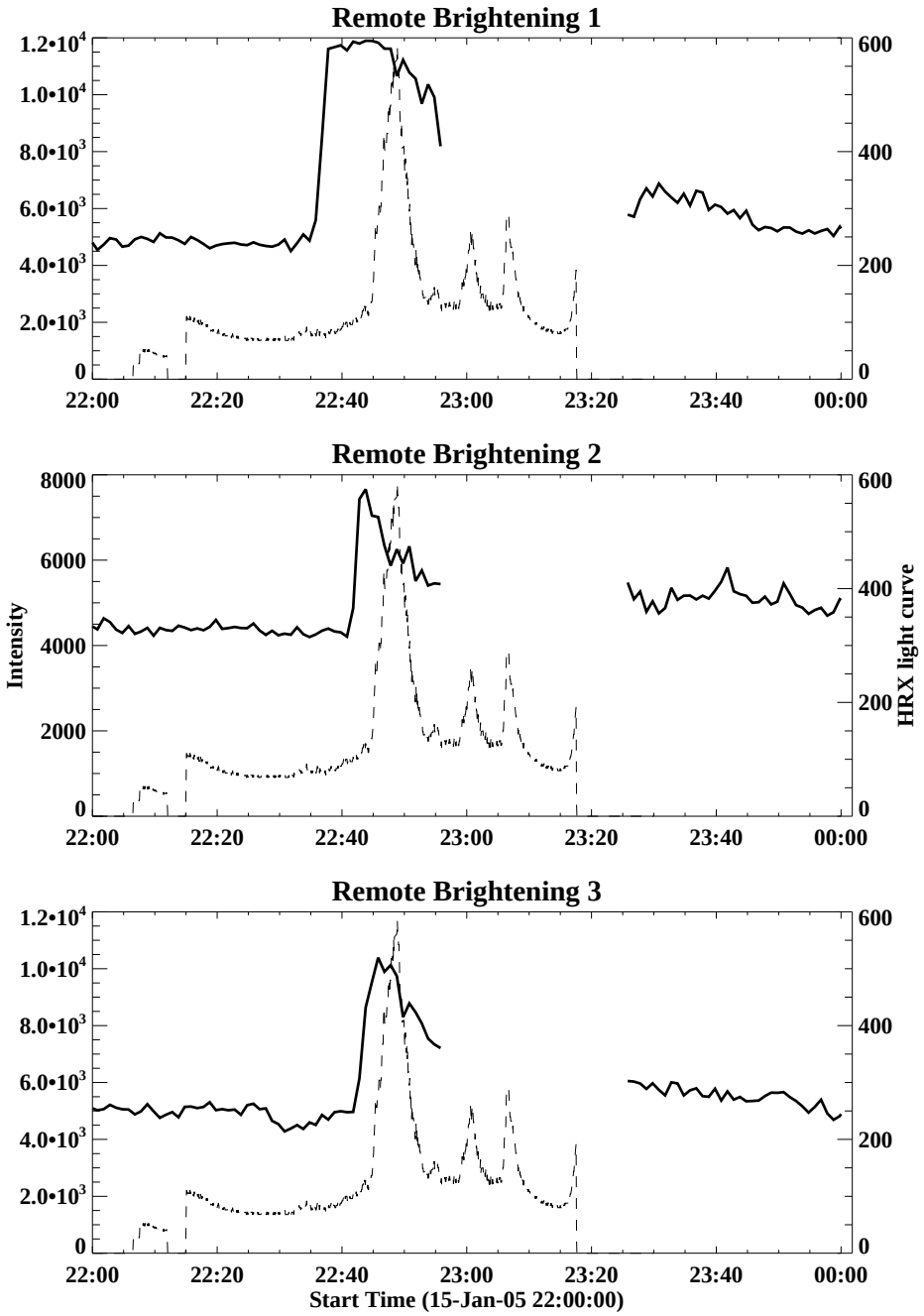

Figure 3.9 Time profile of the Hα (bandwidth: 0.25 Å intensity (thick lines) of the three remote brightenings as marked in Figure 3.8, with RHESSI 100-300 keV HXR light curve overplotted (dashed lines). It is obvious that the Hα remote brightenings occurred 5-10 min before the main HXR phase of the flare, which suggests that they may be FPs corresponding to the first stage of reconnection.

quantitative estimate of the magnetic reconnection rate in the coronal reconnecting current sheet (RCS) from observable quantities, i.e., $\varphi_{rec} = \int V_r B_n dl = \frac{\partial}{\partial t} \int B_n da$, where V_r is the ribbon separation velocity, B_n is the normal component of the local magnetic field strength measured in the ribbon location, dl is the length along the ribbons, and da is the newly brightened area swept by the flare ribbons. In particular, $E = V_r B_n$ is the convective electric field, often taken as a measure of a reconnection rate. In Figure 3.10 the ribbon position is illustrated as a function of time, which clearly shows two stages of ribbon motion: the slower motion ($8 kms^{-1}$) from $\sim 22:30 - 22:49$ UT and a faster motion ($33 kms^{-1}$) from $\sim 22:49 - 22:54$ UT. This can also be seen in Figure 3.5 in Liu et al. (2010). There is a slight difference in the timing of the two stages shown in their paper and the present study. Changing from stage one to two appears at 22:45 UT in Liu et al. (2010) and 22:49 UT here. The difference is due to the fact that they used kernels (centroid), while in this chapter the front edge is used. Based on the timing of the HXR emission, a conclusion can be readily drawn that all the Hα remote brightenings occurred before the fast reconnection phase and hence belong to the first stage of the eruption. Later on (see the image at 23:25:48 UT), loops of an arcade are seen overlying the active region, similar to what was observed as a result of sigmoid eruption (Liu et al. 2007, e.g.). In Figure 3.10, the entire flaring period has been divided into two phases according to the different speed of the ribbons front edge before and after 22:49.

The Change of Lorentz Force

Hudson et al. (2008) quantitatively assessed the back reaction on the photosphere and solar interior based on the coronal field evolution required to release flare energy, and made the

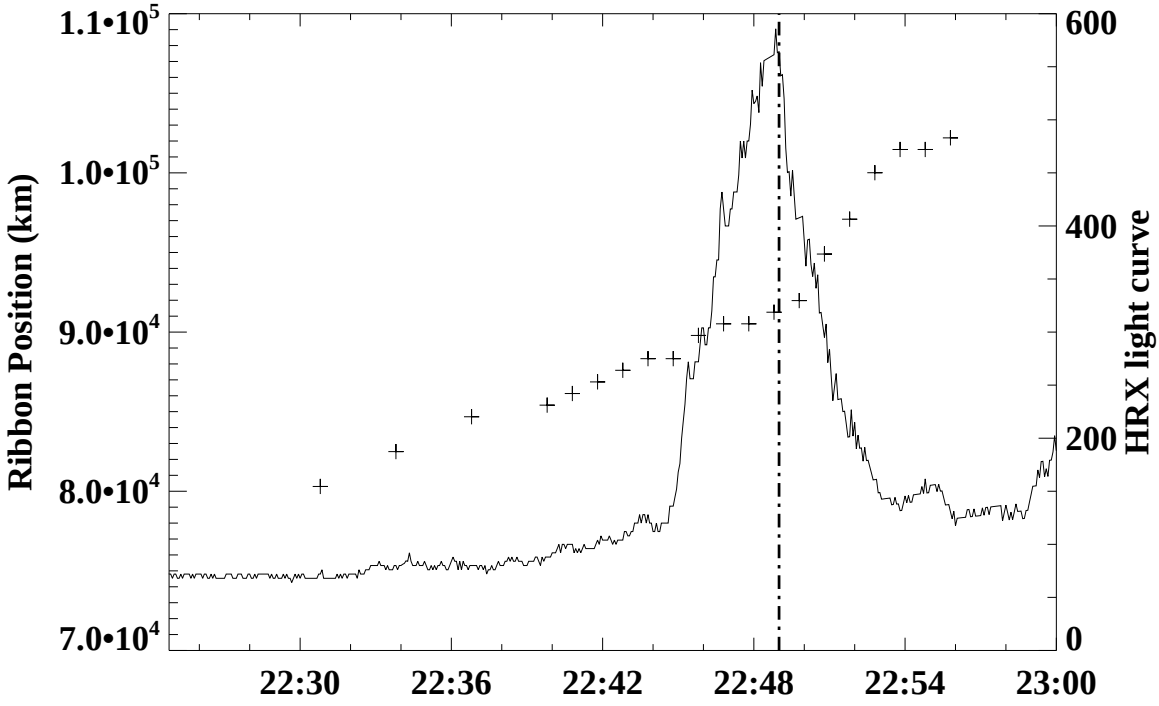

Figure 3.10 Position of fastest moving ribbon as a function of time ("+"), in comparison with 100-300 keV RHESSI HXR light curve. Two stages of ribbon separation motion are evident, as marked by the vertical dash-dot line.

prediction that the postflare photospheric fields will become more horizontal. Based on the study of sudden motion of a sunspot (Anwar et al. 1993), Hudson et al. (2008) introduced the concept of "jerk" produced by coronal restructuring, which may be linked to helioseismic waves found in powerful impulsive flares (Kosovichev & Zharkova 1998) as suggested by further evidence (e.g. Martínez-Oliveros & Donea 2009). As related to the evolution of vector magnetic fields, Hudson et al. (2008) shows that the near surface Lorentz force should have a sudden drop associated with flares. Wang & Liu (2010) surveyed more than 20 X-class flares and provide direct and indirect evidence of field line changes to more horizontal topology after eruptions.

To compare the prediction made by Hudson et al. (2008) with observations of the flare in the current study, the change of Lorentz force is calculated in equation 2.3. Figure 3.11 shows the mean change of Lorentz force per unit area as a function of time for the area marked by the arrow in Figure 3.6. Indeed, the Lorentz force has an irreversible and sudden change associated with the flare, with a drop of magnitude of 6000 dyne$\cdot$ cm^{-2}. Integrating over the area of interest yields a change of Lorentz force of 1.0×10^{22} dyne consistent with what was approximated in Hudson et al. (2008). Moreover, the more inclined magnetic configuration after flare eruption is in agreement with the physical picture. It is possible that this kind of sudden loss of energy balance may be responsible for the excitation of seismic waves.

Unfortunately, there has been no report of a seismic wave for this particular event due to lack of Doppler observations. Martinez-Oliveros and Donea, 2009 studied an X1.2 flare accompanied by well-observed seismic waves, which occurred 20 h earlier in the same active region. It is demonstrated that the flare is located in the same site as the X2.6 flare in

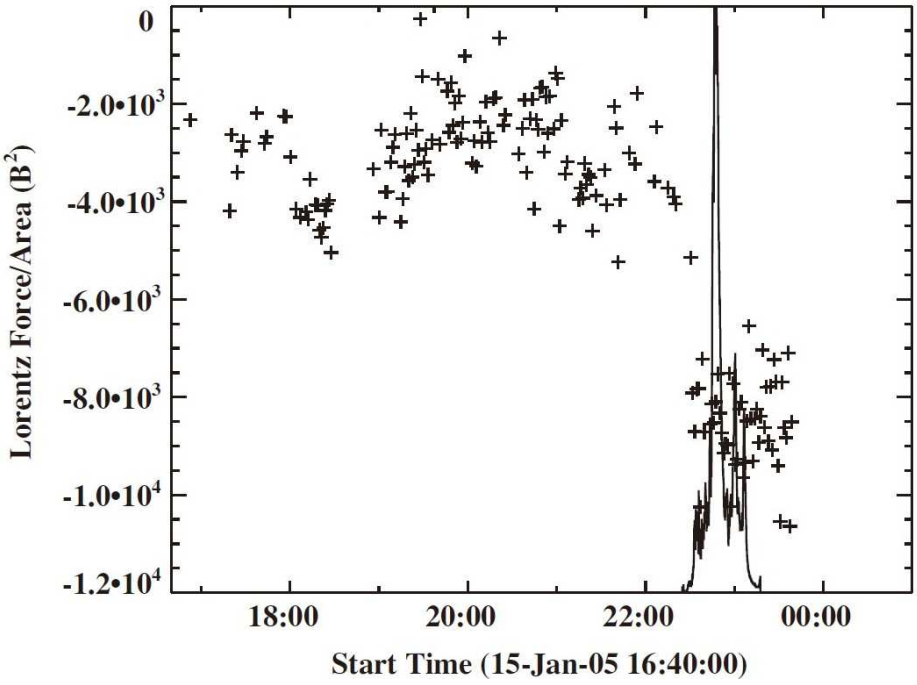

Figure 3.11 The change of Lorentz force per unit area in the region pointed by arrow in Figure 3.6, which has the strongest transverse field enhancement after the flare.

this study. These will motivate future studies to link several aspects of flares, such as two-stage reconnection, rapid change of magnetic fields, loss of force balance, and excitation of seismic waves, towards a full understanding of the flaring phenomenon.

3.4 The Change of Magnetic Field Associated with X5.3 Flare of 2001 August 25

To show the temporal evolution of the magnetic inclination angles associated with flares, another event that occurred on 2001 August 25 was studied. For this event, there were DVMG data taken at BBSO. The DVMG magnetogram typically covers an area of about 300" $\times$ 300" with 0.6" pixel resolution and 1 minute cadence. The decayed and enhanced regions were identified by the difference images obtained with TRACE WL observation. To link the temporal evolution of the flare, the derivative of the soft X-ray light curve was

superposed onto the time profiles of the magnetic inclination angle change.

This event occurred in active region 9591, with the peak GOES soft X-ray emission at 16:45 UT on 2001 August 25. The upper panel in Figure 3.12 shows the morphology of the preflare and the postflare states in TRACE WL for this X5.3 event and the difference image of these two states. The penumbral decayed regions and the center darkened regions were indicated by the blue and red contours, respectively. In the middle panel of Figure 3.12 the mean magnetic inclination angle evolution of the decayed and enhanced areas was analyzed, and the time profile of the mean transverse field strength was shown in the bottom panel. The derivative of the soft X-ray light curve was superposed onto the time profiles of the magnetic inclination angle and the transverse field strength. It is found that the magnetic inclination angle in the penumbral decayed region increased about 9° after the flare, while that in the umbral enhanced region decreased by about 4°.

3.5 Summary

The high-cadence and high-resolution observations obtained with Hinode/SOT and BBSO provide an excellent opportunity to study the flare-associated changes on magnetic structures. In this chapter, the pre- to post-flare changes on magnetic inclination angle and transverse magnetic field strength are presented. The results of three case studies are listed in Table 3.1.

All three events demonstrate some consistent changes of magnetic settings associated with flares and are summarized as follows: (1) The penumbral segments in the peripheral sunspot region, identified by WL or G-band observations, show rapid decay after the major flares. (2) In the central umbral or inner penumbral close to the flaring magnetic PIL,

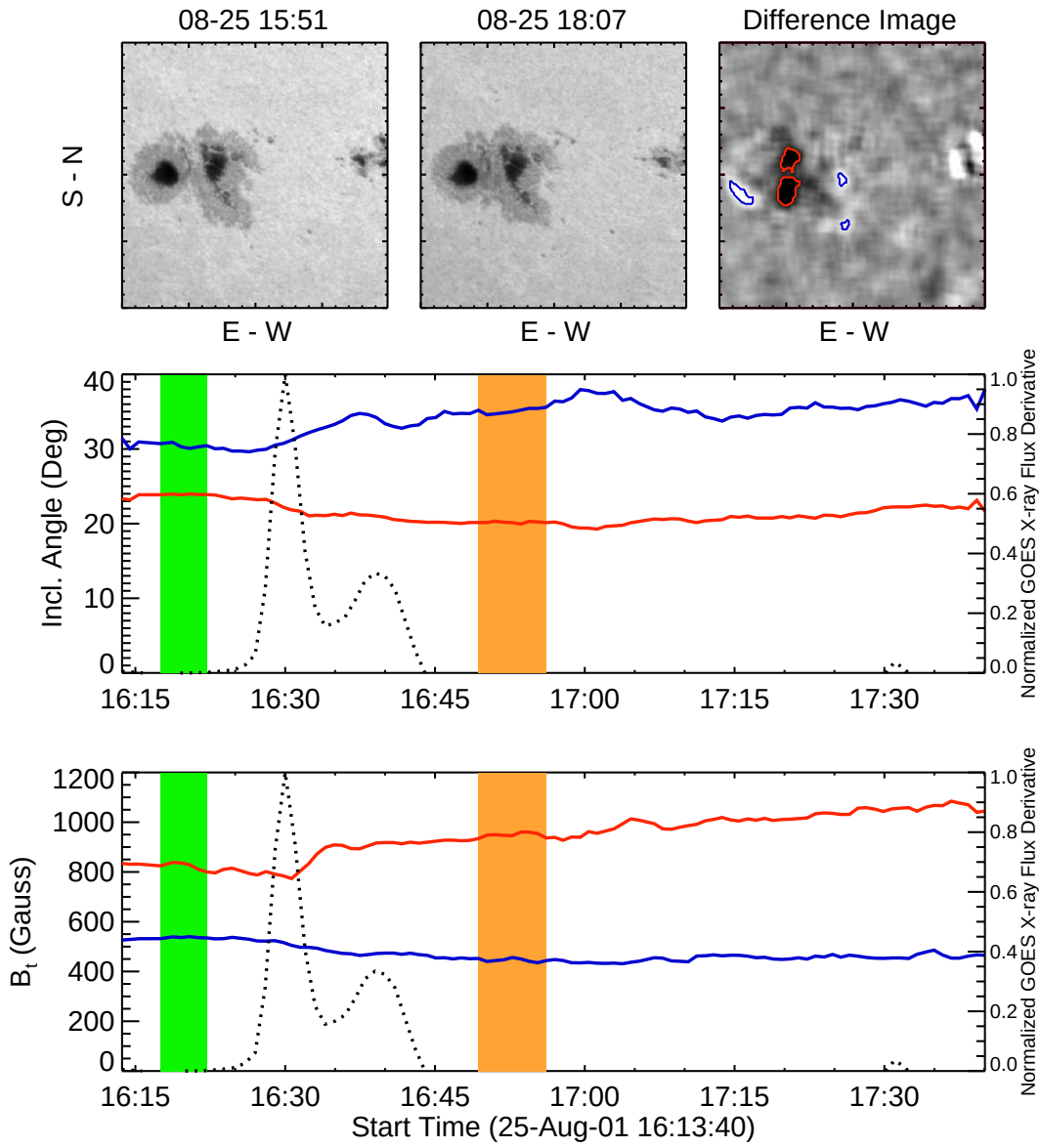

Figure 3.12 *Top panel*: TRACE WL images taken before *(left)* and after *(middle)* the X5.3 flare, and the difference image *(right)*. The decayed and enhanced regions are marked with the blue and red contours, respectively. The FOV is 160"×180". *Bottom panel*: The time variation of the mean magnetic inclination angle in decayed area (*blue*) and enhanced area (*red*). The dotted curve is the time derivative of GOES X-ray flux. The vertical green and orange lines indicate the time ranges chosen to calculate the mean values before and after the flares.

magnetic inclination angle decreases and transverse magnetic field increases after the major flares. (3) There is an obvious sudden enhancement of downward Lorentz force exerted on the flaring region. (4) The remote brightenings that occur before the main HXR emissions signify the beginning of magnetic reconnection between magnetic elbows of the sigmoid. The remote brightening areas that appear as additional flare ribbons, together with the ribbons at the flare core region, outline the overall sigmoidal configuration. (5) Flare ribbon separation starts with a slow phase co-temporal with remote brightenings (the first stage of reconnection), followed by a fast phase when HXR emissions peaked (the second stage of reconnection). This two-stage magnetic reconnection accounts for the sigmoid-to-arcade transformation and is discernible in Hα images.

Motivated by these results, Wang et al. (2012); Liu et al. (2012) further investigated the flare-related magnetic changes with the HMI observation of NOAA active region 11158, and also found the rapid and irreversible enhancement in the horizontal magnetic field at the flaring magnetic PIL. It is found that the photospheric field becoming more inclined is unequivocally associated with the flare occurrence. In sigmoidal active regions, the enhancement areas are located between the two chromospheric flare ribbons and the initial conjugate hard X-ray FPs. These results strongly support the conjecture that the photospheric magnetic field near the PIL must become more horizontal after eruptions. This rapid and permanent magnetic field change could be related to the newly formed low-lying fields in the tether-cutting reconnection model and the implosion of the coronal field due to the energy release as proposed in the recent modeling of Fisher et al. (2012).

Table 3.1 The Change of Different Parameters

Parameters		θ (Degree)[a]	B_t (Gauss)[b]
2006 Dec. 13	Decayed Regions	$\uparrow\sim$ 3.3 degree	$\downarrow\sim$ 16%
X3.4 Event	Enhanced Regions	$\downarrow\sim$ 5 degree	$\uparrow\sim$ 20%
2001 Aug. 25	Decayed Regions	$\uparrow\sim$ 5 degree	$\downarrow\sim$ 17%
X5.3 Event	Enhanced Regions	$\downarrow\sim$ 4.8 degree	$\uparrow\sim$ 15%
2005 Jan. 15	Decayed Regions	$\downarrow\sim$ 1.8 degree	$\downarrow\sim$ 10%
X2.6 Event	Enhanced Regions	$\downarrow\sim$ 5 degree	$\uparrow\sim$ 22%

[a] θ Magnetic Inclination Angle.

[b] B_t Transverse Field Strength.

CHAPTER 4

COMPARISON BETWEEN SIMULATION AND OBSERVATION

It has been a long-standing question in solar physics how magnetic field structure changes during eruptive events (e.g., flares and CMEs). In this chapter[1], the eruption-associated changes are compared in the magnetic inclination angle, the horizontal component of magnetic field vectors, the FPs distance and the Lorentz force between the observation discussed in previous chapter and the numerical simulation of Fan (2010). Both observation and simulation show that (1) the magnetic inclination angle in the decayed peripheral penumbra increases, while that in the central area close to the flaring PIL deceases after the flare; (2) the horizontal component of magnetic field increases at the lower altitude near the flaring PIL after the flare; (3) a de-shearing and diverging motion of the flare ribbon/FPs followed by the converging motion during the eruption; (4) The result of Lorentz force change suggests that the field lines at the flaring neutral line turn to more horizontal near the surface, that is in agreement with the prediction of Hudson et al. (2008).

4.1 Introduction

Solar eruptions, including flares, filament eruptions, and CMEs have been understood as the result of magnetic reconnection in the solar corona (e.g., Kopp & Pneuman 1976; Antiochos et al. 1999). Although surface magnetic field evolution (such as new flux emergence and shear motion) plays important roles in building energy and triggering an eruption, most

[1]This chapter is based on the following paper:
Li, Y., Jing, J., Fan, Y., & Wang, H. 2011, Astrophys. J., 727, L19.

models of flares and CMEs have assumed rigid anchoring of magnetic fields at the photosphere, which implies that the normal magnetic field on the photosphere does not change during the eruption. The key reason behind this assumption is that the photosphere has a much higher density and gas pressure than the corona. Recently, Hudson et al. (2008) quantitatively assessed the back reaction on the solar surface and interior resulting from the coronal field evolution required to release energy, and made the prediction that after flares, the photospheric magnetic fields become more horizontal. Their analysis is based on the simple principle that any change of magnetic energy must lead to a corresponding change in magnetic pressure.

From the observational side, various properties of photospheric magnetic field changes associated with large flares have been studied. For instance, magnetic shear angle has been observed to increase after major flares (Wang et al. 1994). With the vector magnetogram from Hinode (Kosugi et al. 2007) and the advanced NLFF field modeling techniques (Wiegelmann et al. 2008), Jing et al. (2008) investigated the altitude variation of magnetic shear associated with the X3.4 flare of 2006 December 13. It was shown that magnetic shear increased after the flare below $\sim$ 8 Mm and decreased from that height to $\sim$ 70 Mm. With BBSO and MDI magnetograms, Wang et al. (2002) investigated the magnetic flux which shows an increase in the leading polarity and a decrease of smaller magnitude in the following polarity. Kosovichev & Zharkova (2001), Sudol & Harvey (2005) and Petrie & Sudol (2010) also provided comprehensive evidence of flare-related magnetic field changes. In particular, Sudol & Harvey (2005) conducted a survey of 15 X-class flares, and found that abrupt and persistent changes in the photospheric longitudinal magnetic fields are common features associated with X-class flares. At least two-thirds of these field changes occurred

in the penumbral regions of sunspots. Furthermore, recent WL observations demonstrated a consistent pattern of changes in sunspot structures: part of the penumbral segments in the outer δ spot vanish rapidly after flares, and meanwhile, the umbral cores and/or inner penumbral regions are darkened (Wang et al. 2004a; Deng et al. 2005; Liu et al. 2005). Wang & Liu (2010) synthesized many aspects of observations and concluded that magnetic field lines near the flaring PIL turn to a more horizontal direction, in agreement with the prediction of Hudson et al. (2008).

To understand the flare-associated magnetic changes observed at the photosphere level as reported above, it is crucial to have a complete picture of the 3-D structure of the magnetic fields and their evolution associated with flares. Although the coronal imaging contributes to the solution of this problem to a certain degree, it lacks the crucial quantitative magnetic measurements. At present NLFF magnetic field extrapolations and numerical simulations are critical to quantitatively study the 3-D structure of magnetic fields and their evolution.

Furthermore, it is extremely important that the observations and models be compared quantitatively in the context of evolution of 3-D magnetic fields. In this chapter, the comparison will be explored using the recent work of Fan (2010), which presents 3-D MHD simulations of the evolution of the magnetic field in the corona where the emergence of a twisted magnetic flux tube is driven (kinematically) at the lower boundary into a pre-existing coronal potential arcade field. This approach is based on the supposition that a twisted magnetic flux rope containing helical field lines is an appealing candidate for the basic underlying magnetic field structure for CME precursors (e.g., Gibson & Fan 2006), and that such a coronal flux rope can form as a result of active region flux emergence from

the interior (e.g., Lites et al. 1995).

4.2 Model Description

The MHD numerical simulation used for comparison was constructed by Fan (2010). A sequence of simulations of the magnetic field in the corona was carried out, where the emergence of a twisted flux tube is driven (kinematically) through the lower boundary into a pre-existing corona arcade. Note that in the simulation, the imposed (kinematic) emergence of a twisted flux tube through the lower boundary is not a direct model for the observed event and it does not use the actual observed photospheric magnetic field as the lower boundary driving condition, however it is a means to obtain a sequence of near-force-free coronal flux rope equilibria with an increasing amount of locally detached, twisted flux.

The detailed magnetic field structure in the domain was obtained by solving the following isothermal MHD equations in a spherical domain representing the solar corona, given by $r \in [R_\odot, 5.496R_\odot], \theta \in [5\pi/12, 7\pi/12], \phi \in [-\pi/9.6, \pi/9.6]$ (Fan 2010).

$$\begin{aligned}
\frac{\partial \rho}{\partial t} + \nabla \cdot (\rho \mathbf{v}) &= 0 \\
\rho\left(\frac{\partial \mathbf{v}}{dt} + (\mathbf{v}\cdot\nabla)\mathbf{v}\right) &= -\nabla p - \rho \frac{GM_\odot}{r^2}\hat{\mathbf{r}} + \frac{1}{4\pi}(\nabla \times \mathbf{B}) \times \mathbf{B} \\
\frac{\partial \mathbf{B}}{\partial t} &= \nabla \times (\mathbf{v} \times \mathbf{B}) \\
\nabla \cdot \mathbf{B} &= 0 \\
p &= a_s^2 \rho
\end{aligned} \tag{4.1}$$

where, $\mathbf{v}, \mathbf{B}, \rho, p, a_s, G, M_\odot$ denote respectively the velocity field, the magnetic field, the density, the pressure, the isothermal sound speed, the gravitational constant and the mass

of the Sun. The equations are discretized in the simulated spherical domain which have been resolved by a $432 \times 192 \times 240$ grid. The grid is uniform in the θ and ϕ directions, but non-uniform along the radial direction, with a finer step size in the range from $r = R_s$ to about $r = 1.788\ R_s$ of $dr = 0.0027271\ R_s$, and a geometrically increasing grid spacing above $r = 1.788\ R_s$, reaching about $dr = 0.09316\ R_s$ at the outer boundary.

The initial state of this simulation is assumed to contain a pre-existing potential arcade field in a hydrostatic isothermal atmosphere domain, which is considered as the flare site. Figure 4.1 shows the initial configuration of the simulation in which the red lines indicate the pre-existing potential arcade field. At the lower boundary $r = R_s$, the emergence of a twisted and arched flux tube is imposed by specifying a time-dependent transverse electric field $\mathbf{E}_{\perp|r=R_s}$ with an upward advection velocity:

$$\mathbf{E}_{\perp|r=R_s} = \hat{\mathbf{r}} \times \left[(-\frac{1}{c}\mathbf{v}_0 \times \mathbf{B}_{tube}(R_s, \theta, \phi, t)) \times \hat{\mathbf{r}} \right] \tag{4.2}$$

here, the imposed velocity field is constant $\mathbf{v}_0$ (small compared to the Alfvén speed) in the area where the emerging tube intersects the lower boundary and zero in the rest of the area. After the emergence is stopped and the time-dependent transverse electric field $\mathbf{E}_{\perp|r=R_s}$ is set to zero, a quasi-equilibrium of coronal flux rope with an underlying sigmoid shaped current sheet is established immediately. Subsequently, the flux rope continues to build up due to reconnections in the current sheet and the ejective eruption is triggered when the flux rope exceeds a critical height. The magnetic reconnection is facilitated by numerical resistivity. This study is concentrated on the evolution of the magnetic field immediately above the line-tying lower boundary, i.e., at the grid level 2 corresponding to 4.745 Mm above photosphere.

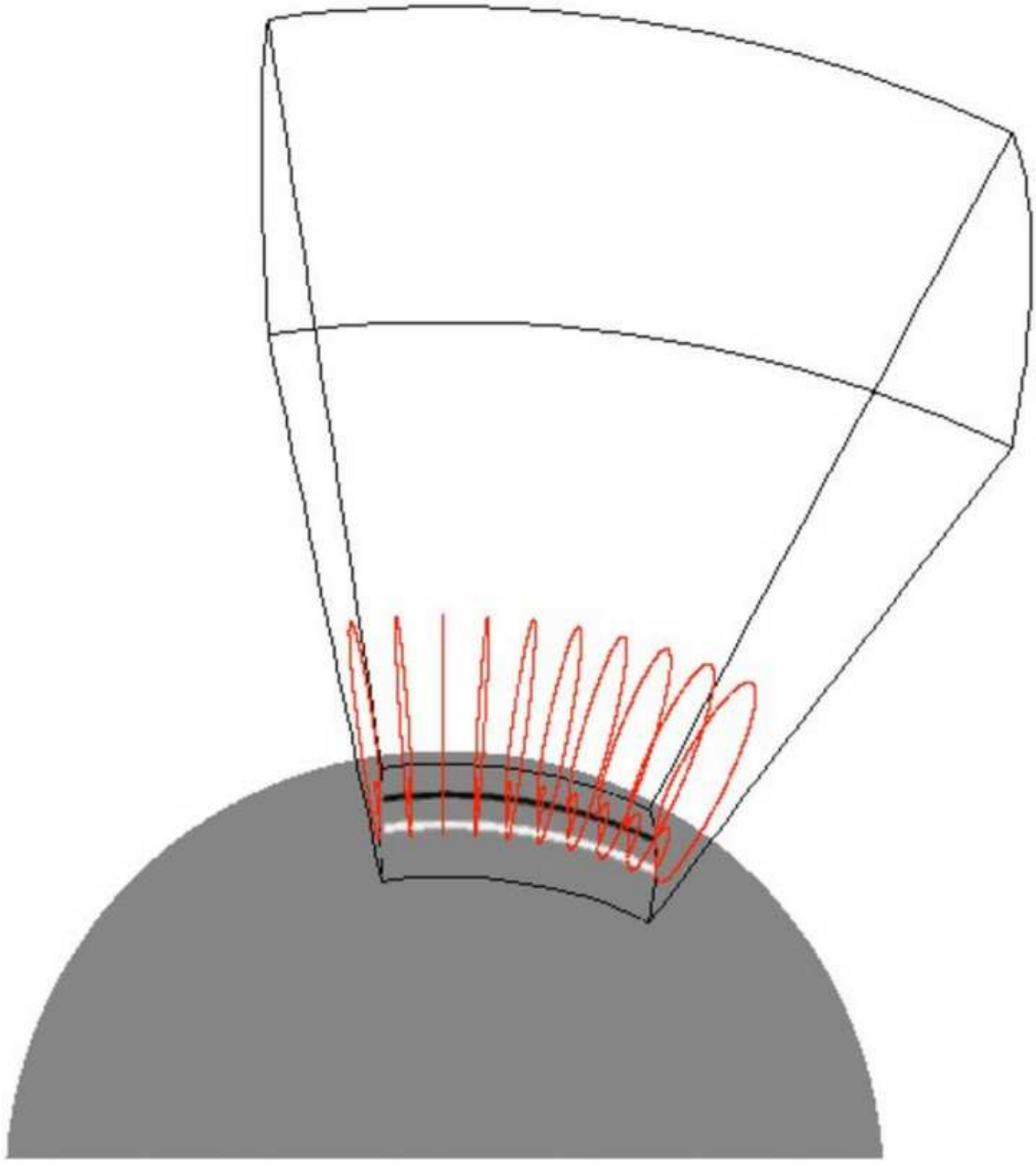

Figure 4.1 Initial configuration of the simulations (see the text for details).

4.3 Result of MHD Simulation

4.3.1 General Magnetic Properties

The data of the MHD simulation are analyzed and compared with the observational results in previous chapter. Note that here the simulation assumes an idealized configuration of an arched coronal flux rope driven into a pre-existing coronal arcade field. It is not a direct modeling of the observed event and it does not use the actual observed photospheric magnetic field as the lower boundary driving condition. Instead, the simulation gives a general description of the characteristic magnetic field changes resulting from the ejection of a line-tied coronal flux rope previously confined in equilibrium. In Figure 4.2, the left two columns compare the magnetic horizontal field and the LOS field taken before and after the eruption in the second layer of the grid along r, which is about 4.745 Mm above the solar surface. The blue boxes indicate the enhanced areas after the eruption, corresponding to the darkening inner penumbra, whereas the red boxes correspond to the outer decaying penumbra. The right panels (from top to bottom) show respectively the time profile of the magnetic inclination angle, the horizontal field strength, and the change of Lorentz force comparing to the pre-eruptive state at $t = 150\tau$ (the unit for time is τ =356.8 s). The dashed lines indicate the flaring time. It is evident that the inclination angle increases and the B_h decreases after the flare in the outer decayed region, while the inclination angle decreases and the B_h increases at the flaring PIL. The change of Lorentz force is calculated by integrating the δf_z in equation 2.3 over an area around the flaring PIL, as suggested by Fisher et al. (2012). The sudden enhancement of the downward Lorentz force after the flare, which indicates the back reaction on the photosphere and solar interior due to releasing of flare energy, is consistent with the prediction by Hudson et al. (2008).

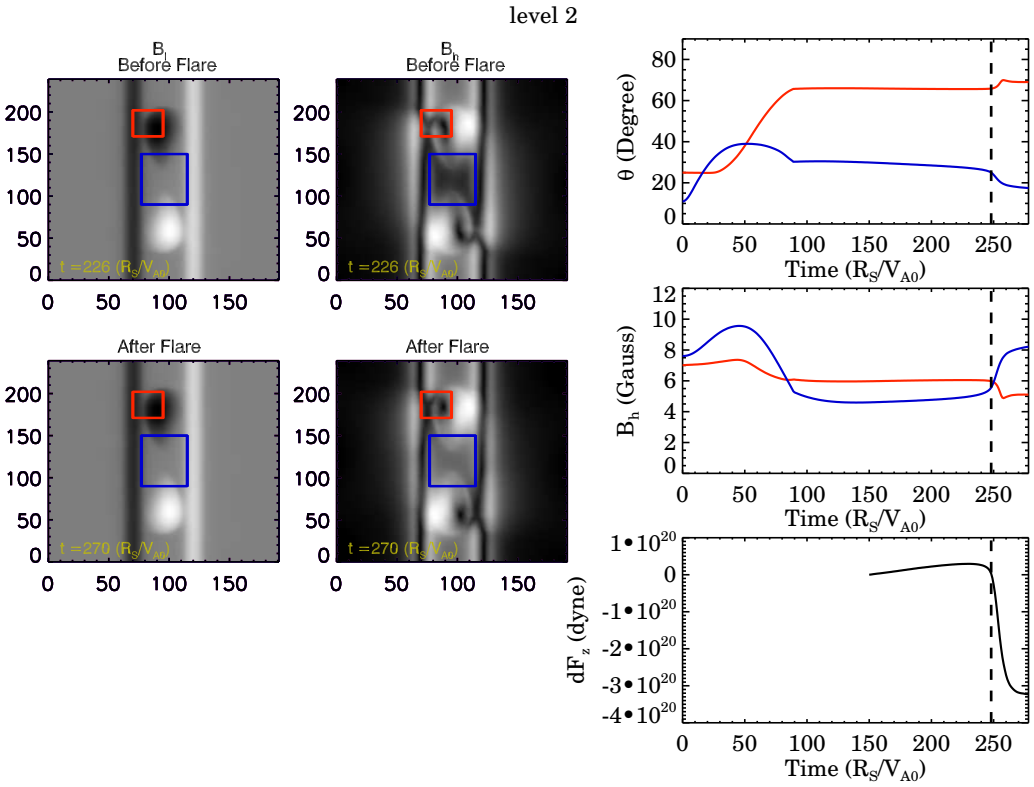

Figure 4.2 MHD simulation result. *Left two columns:* The LOS (B_l) and the horizontal (B_h) magnetic fields before and after the eruption with the red and blue boxes indicating the decayed and enhanced regions, respectively. *Right column:* The time profile, from top to bottom, of the magnetic inclination angle, the horizontal field strength, and the change of Lorentz force compared to the pre-eruptive state at $t = 150\tau$, where $\tau \equiv R_s/V_{A0} = 356.8s$, R_s is the radius of the solar surface, and V_{A0} is the Alfvén speed at the FP of the arcade field.

Recently, Petrie & Sudol (2010) estimated the size of Lorentz force change only using the longitudinal photospheric magnetic measurements. They found that the changed force is associated more with decreases than increases in the longitudinal field. They also found a more tilted photospheric field after the flare. Since the simulated magnetic fields are about one order of magnitude weaker than the real solar data, the Lorentz force change derived from the simulated data should be two orders of magnitude smaller than that derived from the real solar field strength. It is concluded that the order of magnitude of force changes is $\sim 10^{22}$ dynes, which is comparable to the force change predicted by Hudson, Fisher & Welsch to power a subsurface seismic wave.

Figure 4.3 shows the average magnetic inclination angle in the decayed and enhanced areas as a function of altitude for two time points (before and after the eruption). The decayed and the enhanced regions are extended radially from the line-tied lower boundary to the upper atmosphere. The average magnetic inclination angle at various altitudes was averaging over an area. In the enhanced area, the magnetic inclination angle decreases in all heights after the flare. Meanwhile, the angle in the decayed area increases after the flare from the photosphere boundary to 60 Mm. Beyond 60 Mm, a decrease in the decayed region is seen. The observed data presented in Chapter 3.2 manifests a similar trend of changes along altitude in both decayed and enhanced areas after the flare.

4.3.2 The Change of the Flare Footpoint Separation Distance

Ji et al. (2008) studied the sigmoidal structure of the 2003 October 29 X10 flare event. According to the temporal evolution (Figure 4.4) of the X-ray morphological structure, they divided the entire flaring process into two different phases. During phase 1, the configura-

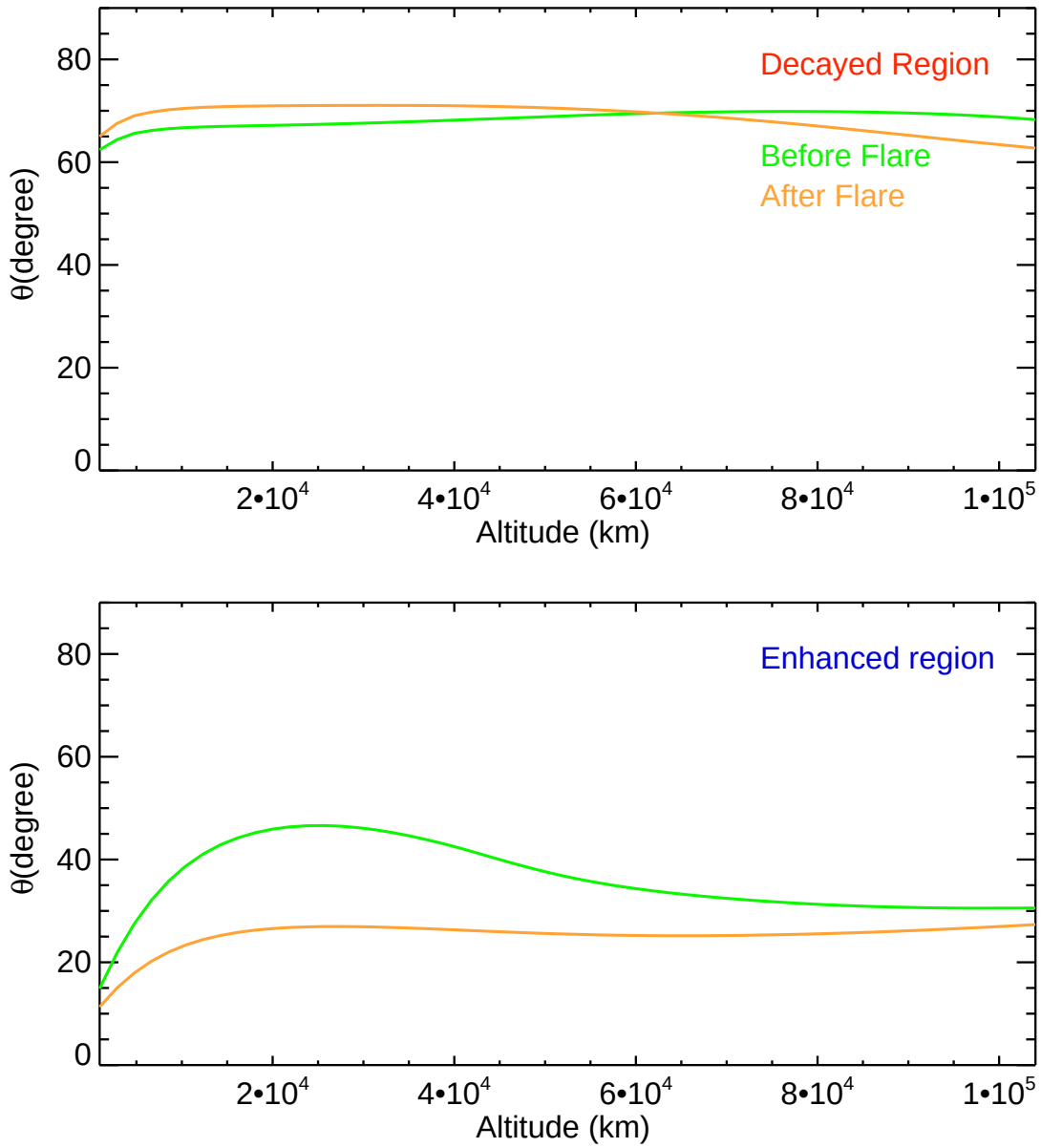

Figure 4.3 The mean value of magnetic inclination angle from the simulation in the decayed *(top)* and enhanced *(bottom)* areas as a function of altitude for two time points. *Green*: Before the flare. *Orange*: After the flare.

tion of HXR at different energy bands resembled the initial sigmoidal structure, therefore this phase is referred to as the sigmoid phase. The overall FPs motion in the sigmoid phase is converging to make the sigmoidal source much more compact. During phase 2 which is referred to as the arcade phase, two FPs move apart.

To compare the FP motion in the simulation, Figure 4.5 shows the snapshots of the LOS current density field with the red plus and blue minus signs indicating the centroid of the positive and negative LOS current density, respectively. The current sheets form due to the interaction between the emerging twisted flux and the pre-existing coronal potential arcade field. The relative motion of centroid points of the LOS current density outlines the motion of the current sheet cores. It is assumed that the field lines go through the areas near the centroid points of positive and negative LOS current density have just undergone reconnection. The plasma along these field lines is expected to be heated due to the magnetic energy dissipation. Therefore, the location of the centroid points of current density is used to indicate the location of the FP brightening, corresponding to the locations of the chromospheric flare ribbons. In Fan (2010), the field lines that go through the current layers outlined by the J/B iso-surface have been traced out in Figure 4.6. When viewing from the above, the flare loops display a narrow sigmoid brightening at the onset of eruption and later broaden into a curved row of bright loops with increasing height, which is consistent with the commonly observed sigmoid-to-arcade transition during eruptive flares (Fan 2010).

Figure 4.7 shows the LOS magnetic field before the eruption at $t = 226\tau$ with the PIL in red. The magnetic PIL is simplified to a straight line, which is a linear fit of the PIL shown as the blue dotted line in Figure 4.7.

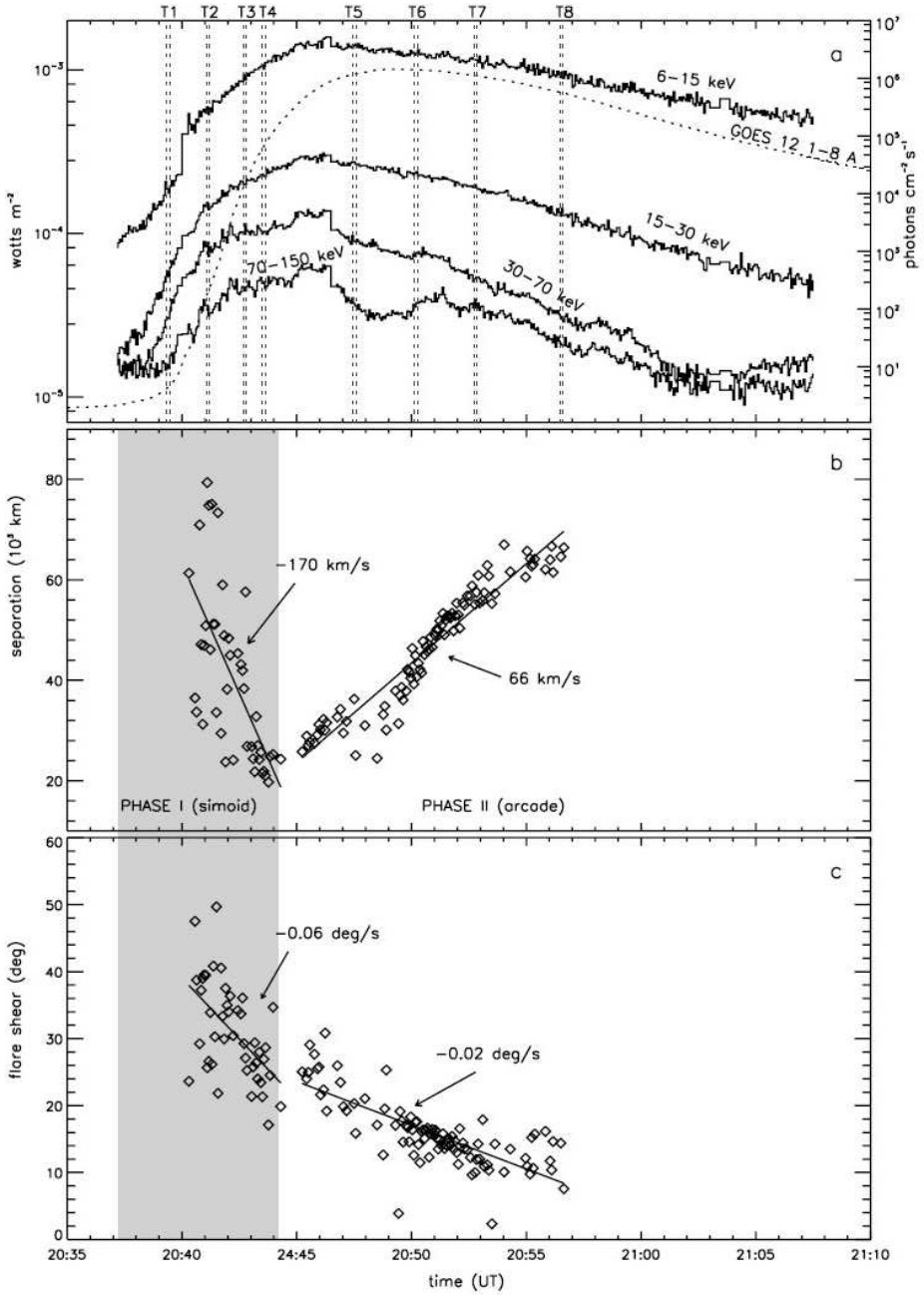

Figure 4.4 (a) GOES SXR light curve and RHESSI HXR light curves for the flare. (b, c) Time profiles of FP separation and flare shear measured with the FPs in the energy range of 70-150 keV. Shaded area corresponds to the sigmoid period. (From Ji et al. (2008).)

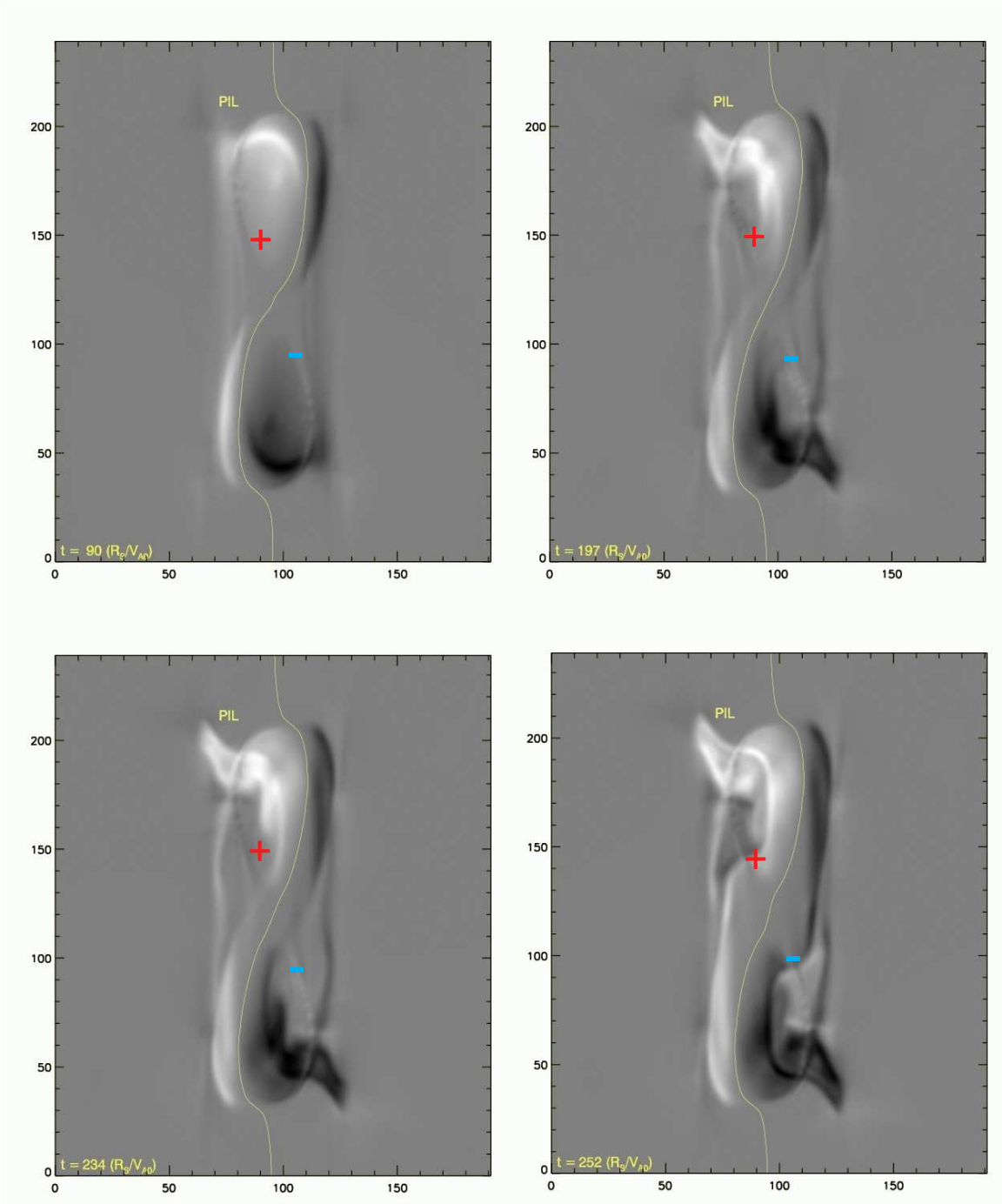

Figure 4.5 Snapshots of the LOS current density. The red plus sigh indicates the centroid point of the positive current density, while blue minus sign indicates that of the negative current density. The thin yellow lines show the PIL at each time point.

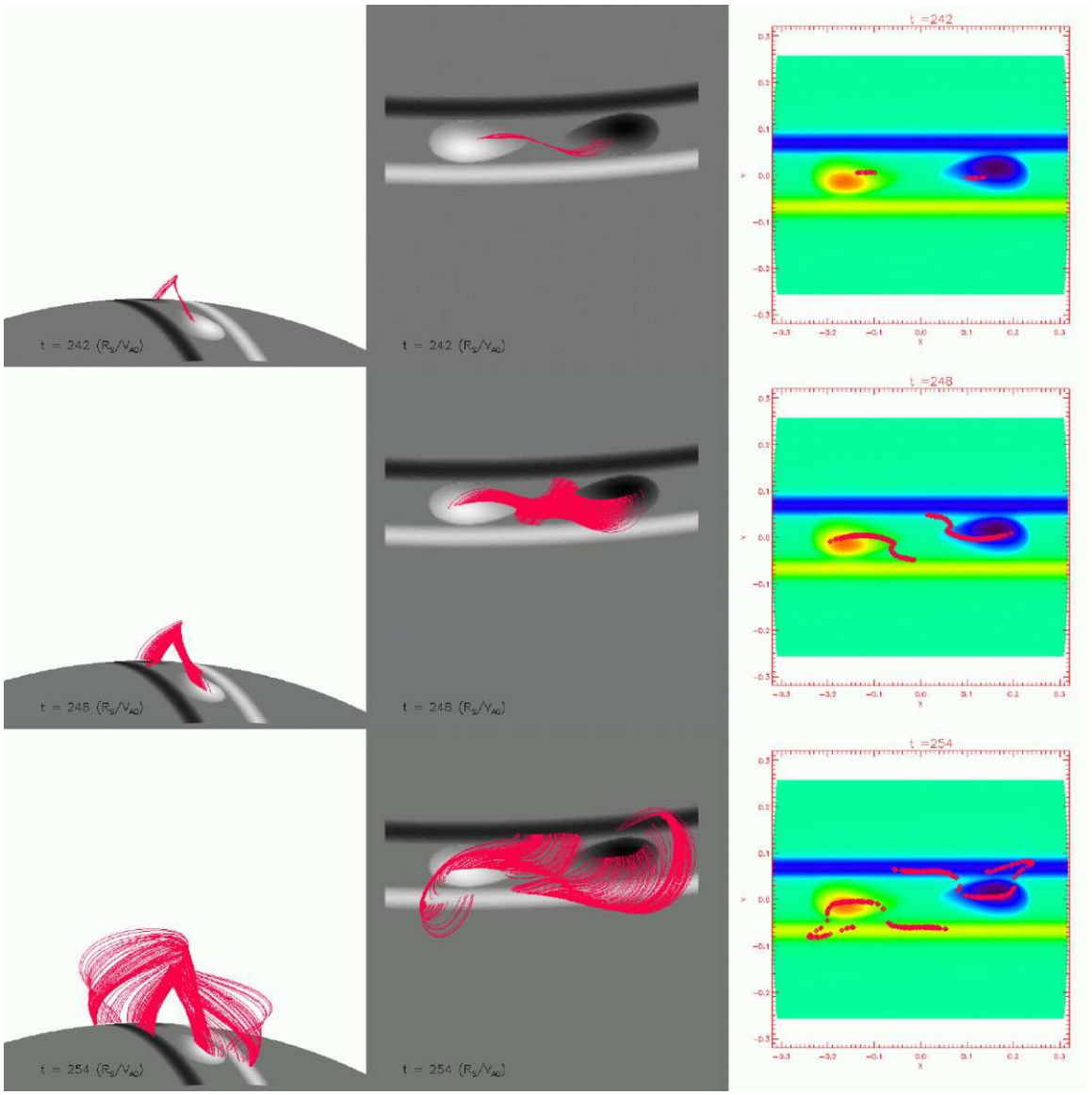

Figure 4.6 Two perspective views (left and middle columns) of sampled field lines (red field lines) whose tops are in the most intense part of the current layer , at three time instances during the eruption, indicating the morphology of the post-flare loops which have just undergone reconnection in the most intensely driven part of the current layer and whose FPs correspond to the location of the chromospheric flare ribbons (red points in the right column panels). The gray-scale images in the left and middle column panels and the color images in the right column panels show the normal magnetic field distribution B_r on the lower boundary with white and yellow-red representing positive B_r , and black and blue-black indicating negative B_r. (Courtesy of Fan (2010).)

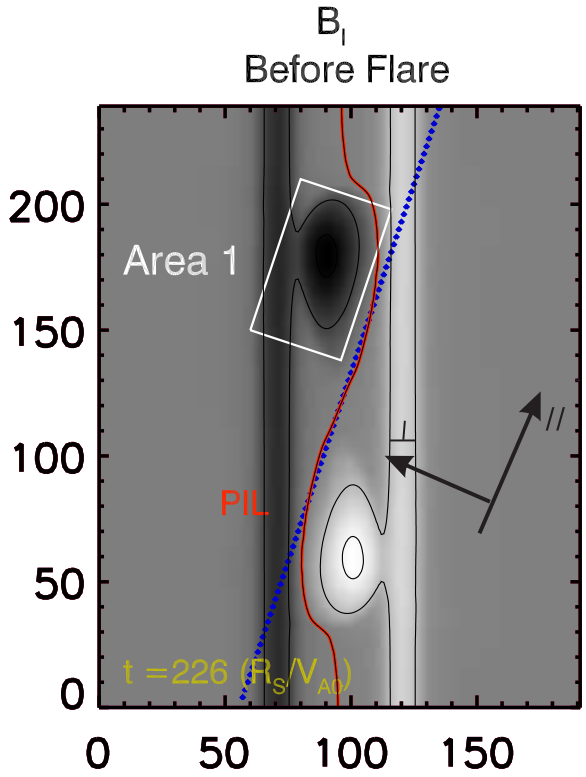

Figure 4.7 The LOS (B_l) magnetic field before the eruption at$t = 226\tau$ with the PIL in red and the fitted PIL in dotted blue. The white box Area 1 indicating the Gaussian Box of interest. Here $\tau \equiv R_s/V_{A0} = 356.8s$, R_s is the radius of the solar surface and the V_{A0} is the *Alfvén* speed at the FP of the arcade field.

In this simulation, as the emerging flux tube enters into the lower boundary, a portion of the twisted flux of the torus is transported into the corona. Based on the description in Fan (2010), during the emergence phase from $t = 0$ to 89.125τ, the distance between the positive and negative centroid points of current density increases gradually in both perpendicular and parallel directions to the fitted PIL, indicating the accumulation of magnetic shearing and energy. From $t = 90\tau$ to about $t = 197\tau$, the emergence stops and the coronal flux ropes settle into a quasi-static rise. In this stage, the simulated FPs show a steady evolution with slight deceasing in distance. Then the flux rope reaches a critical height after which it accelerates and eventually erupts. This stage exhibits a distinct increase of the centroid point distance in perpendicular and parallel directions.

Comparing the simulation results with the aforementioned observation by Ji et al. (2008), in the MHD simulation, the whole flaring process evolves in the similar two steps: phase 1 (from $t = 248\tau$ to $t = 257\tau$) and phase 2 (from $t = 257\tau$ to $t = 265\tau$). In order to show the two kinds of motion, i.e., the converging and separating motion, the distance between the positive and negative centroid points is projected in the directions perpendicular and parallel to the fitted PIL, and their temporal evolution is shown in Figure 4.8. There is a clear converging motion in phase 1 and the separation in phase 2. The estimated converging rate in phase 1 is 1.5 km s^{-1} and the diversing rate in phase 2 is 2.3 km s^{-1}. During the entire flaring process, the value of flare shear, represented by the shear angle between the positive and negative centroid points of current density deceases steadily. The unshearing rate in phase 1 is larger than that in phase 2. Table 4.1 compares the change rate of shear angle and separation distance between simulation and observation reported by Ji et al. (2008). It is found that the simulation is strikingly similar to the observation and well

manifests the two-stage characteristics of the FP motion in observation, i.e., converging in the initial sigmoid phase and separation in the arcade phase after flaring.

4.3.3 The Change of Horizontal Lorentz Force

The calculation method of horizontal Lorentz force has been discussed in detail in chapter 2.3.2. In Figure 4.7, Area 1 indicates the Gaussian box of interest, whose bottom and upper boundaries correspond to level 1 and level 3 of the simulation data, respectively. The sketch of this Gaussian box is shown as the green lined box in Figure 2.1. This volume mainly contains the negative polarity of the emerging flux in lower solar atmosphere. The directions parallel and perpendicular to the fitted PIL are indicated in Figure 4.7, where the arrows define the positive directions of the Lorentz force components. The upper panel of Figure 4.9 shows the time profile of the horizontal Lorentz force exerted on the Gaussian box. The bottom panels focus on the time interval as indicated by the yellow region in the top panels.

In this plot, the horizontal Lorentz Force parallel ($F_{\parallel}$) and perpendicular ($F_{\perp}$) to the PIL show a synchronous variation in magnitude. Before the emergence stops at $T_{stp} = 89.125\tau$, both the twisted flux accumulated in the corona and the net Lorentz Force in the parallel direction increase before $t = 30\tau$ and decrease thereafter. On the contrary, the net

Table 4.1 Comparison of the FPs Shear and Separation Change Rate between MHD Simulation and Observation

Data	Shear	Angle	Separation	Distance
	Phase 1	Phase 2	Phase 1	Phase 2
Observation	-0.06°s^{-1}	-0.02°s^{-1}	-170 $km\ s^{-1}$	66 $km\ s^{-1}$
Simulation	-0.003°s^{-1}	-0.001°s^{-1}	-1.5 $km\ s^{-1}$	2.3 $km\ s^{-1}$

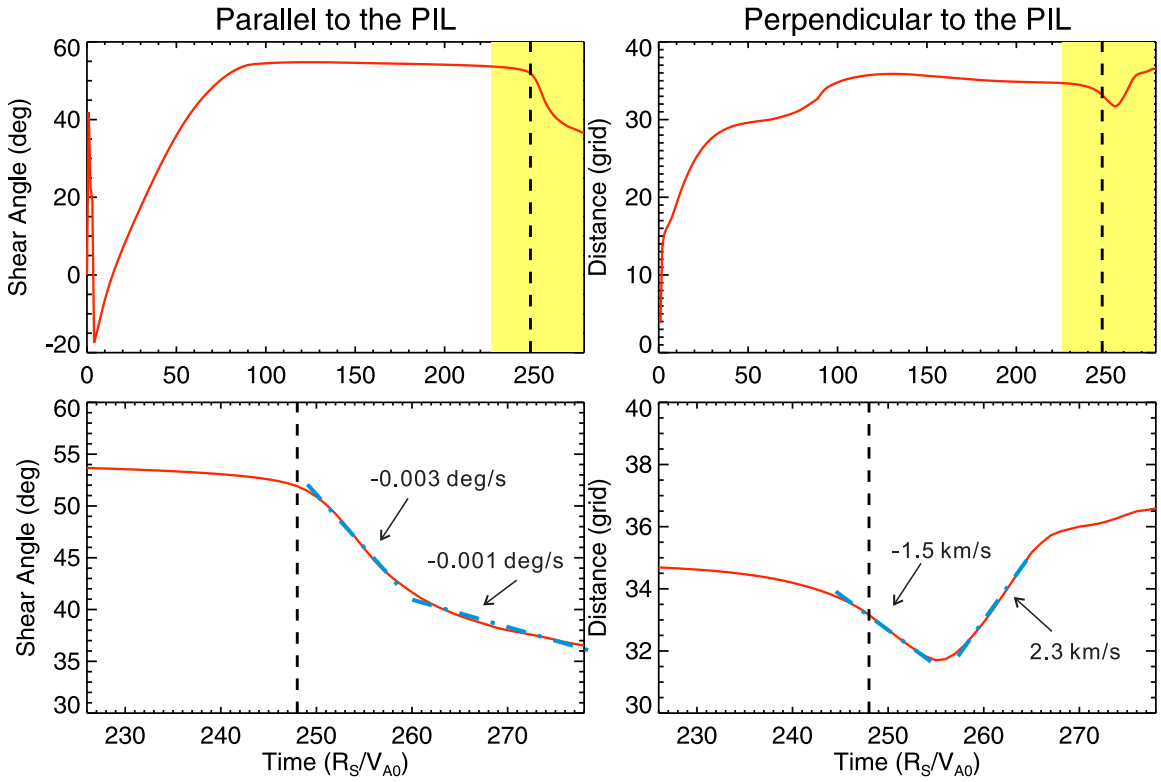

Figure 4.8 The upper panel shows the time profiles of the whole simulated time range, with FPs shear angle on the left and perpendicular direction distance to the fitted PIL on the right. While the bottom panels show the same as the top panels but only focus on the period around the eruption, indicated by the yellow region in the top panels, which are strikingly similar to Figure 4.4 from Ji et al. (2008).

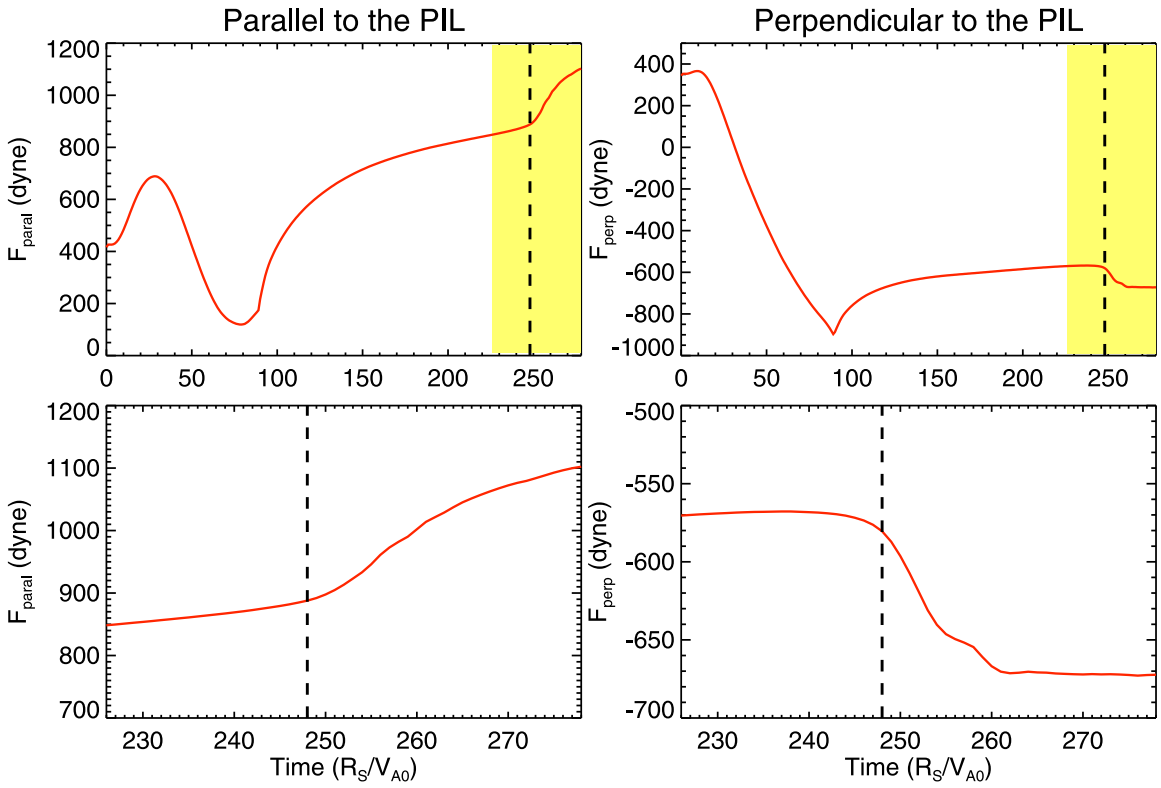

Figure 4.9 The time profiles of the horizontal Lorentz Force exerted on the Gaussian box shown as Area 1 in Figure 4.7. The positive direction is defined in the coordinate of Figure 4.7. *Left:* in the direction parallel to the fitted PIL. *Right:* in the direction perpendicular to the fitted PIL. The bottom panel focuses on the period around the eruption, indicated by the yellow region in the top panel.

Lorentz Force in the perpendicular direction is steady for a short period of time at first and then increases. After the flux emergence stage is over, the magnetic configuration displays a quasi-static rise. In this stage, $F_{\parallel}$ increases gradually and $F_{\perp}$ varies steadily with a little deceasing. During the dynamic ejection phase of the simulation, both $F_{\parallel}$ and $F_{\perp}$ sharply increase. There is an evident and irreversible enhancement of Lorentz force in both perpendicular and parallel directions. This implies that the net Lorentz force acting on the sunspot increases as a result of the flare, which may be associated with the McClymont jerk as reported in Hudson et al. (2008).

4.4 Summary

The flare-associated change of the magnetic inclination angle, the horizontal magnetic field strength, the Lorentz force and the FPs motion in the MHD simulation have been investigated. Both observation and the simulation show: (1) an increase in the magnetic inclination angle in the decayed peripheral penumbra and a decrease in the magnetic inclination angle in the central area close to the flaring PIL; (2) an enhancement in the horizontal magnetic field near the flaring PIL; (3) an enhancement of the downward Lorentz force; (4) a unshearing and diverging motion of the flare ribbon FPs followed by the converging motion. All these results are consistent with the prediction by Hudson et al. (2008). These changes are natural consequences of the lift-off of the pre-existing coronal flux rope, and the subsequent implosion of the magnetic field with the inward collapsing of the post-reconnection loops above the PIL. Moreover, recently a contracting motion of flare loops has been observed in many flares (e.g. Ji et al. 2008). That is, during the early impulsive phase of solar flares, Hα ribbons or HXR FPs are converging. The converging motion are

related to the descending or shrinking motion of HXR looptop sources or radio/EUV flaring loops. Only after the impulsive phase, there begins to appear a outward motion (the usual separation motion) for the flare ribbons or FPs. The strong unshearing motion occurring on the same phase of the converging motion, suggests that the contraction is apparently associated with the release of non-potential magnetic energy inside the sheared core.

The expression for the horizontal components of the Lorentz force acting on a Gaussian box, in which one polarity of the sunspot in lower solar atmosphere is included, is derived. The horizontal Lorentz force integrated over the Gaussian box displays an obvious enhancement in both directions parallel and perpendicular to the PIL. Compared with the unshearing and diverging FPs motion during the phase 1 of the eruption period, the horizontal Lorentz force performs an opposite effect onto the Gaussian box. It is concluded that the flare ribbon FPs motion are due to the upward moving flux rope stretched the overlying sheared magnetic field lines and subsequent reconnections. The enhancement of the horizontal Lorentz force would be related to the release of the coronal energy, which may result in an acceleration of the photosphere material. Originally this phenomenon is explained by electron precipitation. Recently Kosovichev & Zharkova (1998) used data from SOHO and discovered that the seismic waves similar to earthquakes are generated by flares reacting on solar interior and atmosphere. The enhancement of horizontal Lorentz force in this simulation reflects possible inner driver of a seismic wave caused by flares.

It came to the attention that some of these findings are in agreement with the tether-cutting model proposed by Moore et al. (2001). In this reconnection model, a short and flat loop forms near the photosphere after the eruption. The expected change of magnetic field from this model is also consistent with the enhanced horizontal field near the flaring PIL as

obtained from both observation and simulation results.

In addition, note that the spacing of the grid points in the simulation caused a gap in the simulated magnetic field at the photosphere. Although simulated magnetic field at the level 2 which is just above the line-tied bottom boundary is employed, the height of the level 2 field is 4.745 Mm, indicating that it is at the low corona. The field strength there is low, so is the calculated Lorentz force.

CHAPTER 5

3-D EMERGING MAGNETIC STRUCTURE OF ACTIVE REGION 11158 LEADING TO A FLARE ON FEB 15 2011

It is believed that twisted magnetic field is the source of most (if not all) solar energetic events such as flares and CMEs. Several detailed studies have demonstrated that the emergence of twisted flux ropes are highly related to flare occurrence. Tanaka (1991) examined the evolution of a flare-active δ sunspot and proposed a model of an emerging twisted magnetic knot to explain the observed sunspot evolution. From detailed analyses of sunspot evolution, Kurokawa et al. (2002) constructed the emerging twisted flux rope formed by the kink instability of magnetic field through convection zone, and pointed out the twisted flux ropes must be the source of the strong magnetic shear development in a sunspot region to produce a strong flare activity. The evolution of magnetic fields in NOAA active region 11158 over 5 days, was observed by HMI on board SDO. The striking flux emergence and strong shearing motion were detected. These resulted in a quadrupolar sunspot complex that produces several major eruptions, including the first X-class flare of Solar Cycle 24. In this chapter, based on a series of HMI vector magnetograms, the attempt to explain the major evolutional characteristics of NOAA 11158 has been made. In particular, assuming that observation at different time corresponding to different vertical structure of emerging magnetic field, the schematic model was constructed to qualitatively describe the emerging twisted magnetic flux rope.

5.1 Data Sets

NOAA active region 11158 is well observed with 12-minute cadence HMI vector magnetograms over a 5-day period from 2011 February 12-16. The HMI instrument obtains filtergrams in six polarization states at six wavelengths along the Fe I 6173 Å spectral line to compute I, Q, U, V. The vector photosphere magnetic field is retrieved by the Very Fast Inversion of the Stokes Vector (VFISF) algorithm (Borrero et al. 2011) based on the Milne-Eddington approximation. The 180° azimuthal ambiguity is resolved by the "minimum energy" method (Metcalf et al. 2006; Leka et al. 2009). To remove the projection effects, the observed fields are transformed to the heliographic coordinates using a Lambert equal area projection (Calabretta & Greisen 2002). The resulting magnetograms have a 12 minute cadence and 0.5" spatial resolution. The first X-class flare of the solar cycle 24 started at 01:44 UT February 15 2011 on NOAA active region 11158 which was located close to the disk center (S21°, W21°) at that time, and peaked at 01:56 UT, ended at 02:06 UT in GOES 1–8 Å flux.

5.2 Observation and Analysis

NOAA active region 11158 underwent a rapid growth and exhibited complex emerging sunspot motion and interaction during its disk passage. Four emerging bipoles P0/N0, P1/N1, P2/N2 and P3/N3 were identified. The preceding (positive) sunspots are denoted as P, while the following (negative) ones are denoted as N. Based on HMI magnetogram movies, P0/N0 and P1/N1 first appeared on February 10 at around 04:00 UT and 21:00 UT, respectively. The evolution of magnetic field over five days are described in more detail in Sun et al. (2012). Top two rows of Figure 5.1 show the early stage of the AR

development featured with fast emergence for about 1 day. Between P1 and N0 there exists strong shearing motion and a few newly emerging pores. Magnetic field reconnection occurs when P1 and N0 converge to each other, corresponding to the frequent brightenings in AIA images. P2/N2 and P3/N3 started to emerge inside P0/N0 and P1/N1 after around 14:30 and 23:30 UT on February 12, respectively. The merged P2 started to rotate at about 06:00 UT on February 14. Jiang et al. (2012) investigated the rotation of this active region and found out that this clockwise rotating P2 underwent cancellation and collision with small sunspots when it moved toward the northeast. In the third row of Figure 5.1, P2/N2 experienced fast shearing and rotation and the coronal field was reconfigured. Fast sunspot rotation and flux cancellation are observed between P1 and N3. The whole active region has been expanded rapidly. The bottom two rows of Figure 5.1 indicate the evolution towards the end of the 5-day period. The shearing between N0 and P1 continues and the flux emergence becomes periodical. The active region was simplified to a bipolar structure with the converging motion between sunspots of the same polarity.

5.3 Model of Twisted Flux Rope

From the observational results discussed in the previous section, the most important evolutional features of the sunspots and the magnetic field configuration in NOAA active region 11158 are summarized in the following: (1) at first, this active region mainly consisted of two bipoles P0/N0 and P1/N1; (2) the newly emerged pores P2/N2 and P3/N3 underwent fast shearing and rotating motion; (3) the P2 underwent clockwise rotation with N2 and emerged into elongated P1, while N2 converged into N1; (4) P3 merged into P0 while N3 moved towards P1 and the flux cancellation is observed between P1 and N3.

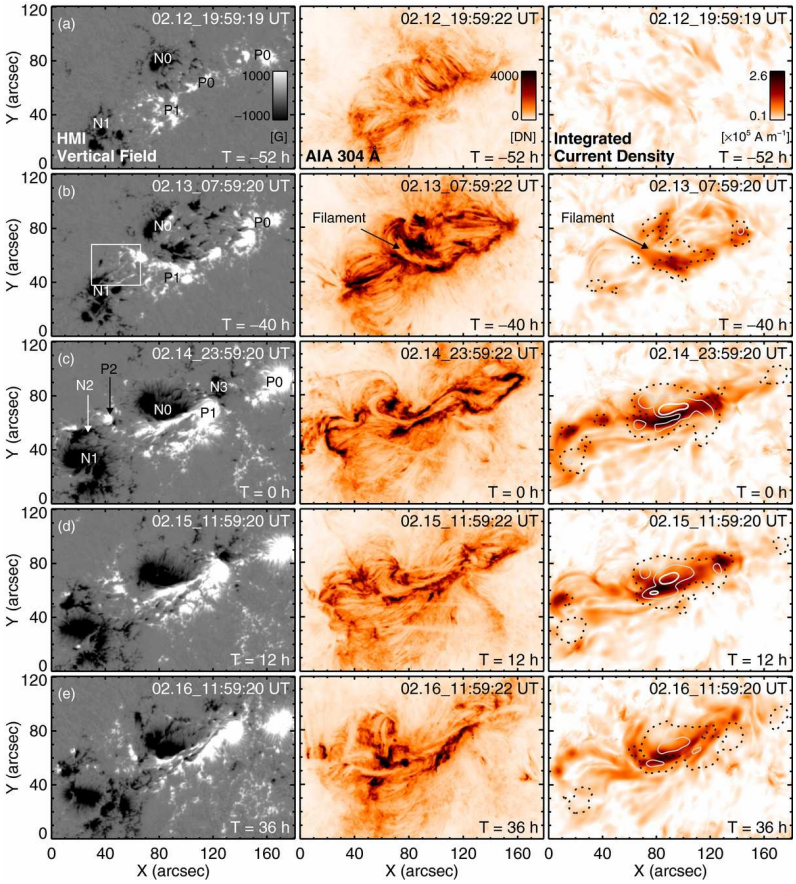

Figure 5.1 Five snapshots of the evolving AR11158. They are taken at about T = -52 h, -40 h, 0 h, 12 h, and 36 h, with February 15 00:00 UT as time 0. Left column: HMI B_z as in native coordinate (as recorded by camera). Middle column: negative AIA 304 Å image showing chromosphere and transition region structures in which the AR filament is best discernible. Right column: vertical integrated current density from NLFFF extrapolation over the lowest 10 Mm. Images are remapped back to the native coordinate for direct comparison of HMI and AIA observations. Features of interest are marked in some panels. (Courtesy of Sun et al. (2012))

Based on these observational features, an emerging twisted flux rope scenario was proposed for this active region in a manner similar to the studies of Tanaka (1991) and Kurokawa et al. (2002). Figure 5.2 is the schematic drawing of the twisted flux rope. At three successive times from T1 to T3, the photospheric surface cuts the ends of the flux rope and the locations of the sunspots are shown. The evolutional features of the sunspots suggest that the rotation might result from the emergence of pre-twisted magnetic flux rope. Two right-handed flux knots were made in this model. The magnetic tension contained in this flux rope forces the knot parts rising slowly. As the flux rope emerging up, the polarities rotated due to the corresponding twisted knot structure. As the rising process continues, the knot reaches a threshold depth and the restored magnetic free energy is released and transferring into kinetic energy due to the sudden untied of the twisted flux. The relaxed flux may erupt and produce flares because of the kink instability. The rotation and emerging properties could also be explained by this model.

5.4 Discussion

The study of the evolution of magnetic field in NOAA 11158 in 5 days around a big X-class flare activity are presented. The gradual flux emergences were observed, accompanied by many drastic changes in the sunspot structures and the magnetic field configuration. The opposite magnetic polarity intrusion and rotation are the essential features of the emerging motions of a twisted magnetic flux rope, which are simultaneously constructed by the proposed model. It is postulated that the acceleration of the sunspot motion, flux emergence and rotation of opposite polarity spots could be the precursory phenomena for eruption, and contain important characteristic of energy release and triggering mechanism of flares.

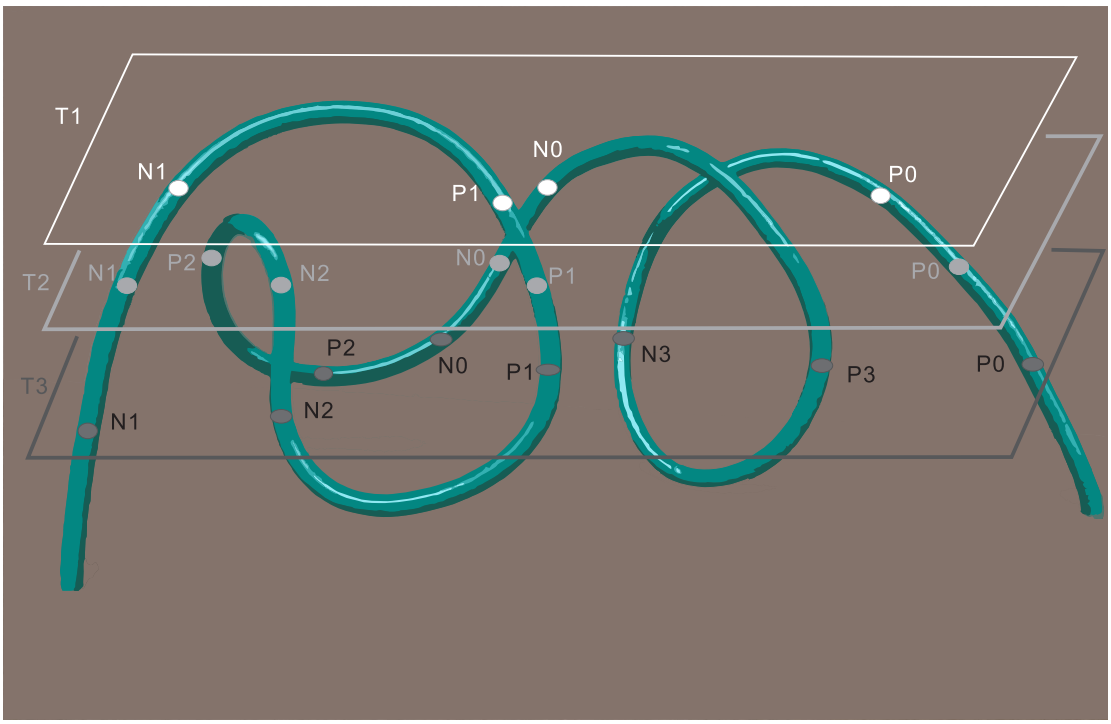

Figure 5.2 Schematic drawing of an emerging twisted flux rope. The photospheric surfaces relative to the emerging flux rope are drawn at three successive times, T1, T2 and T3, and the locations of the sunspots or the cut ends of the flux rope at the photospheric surface.

CHAPTER 6

RADIO EMISSION FROM ACCELERATION SITES OF SOLAR FLARES

In addition to study the triggering mechanism of flares, the study of the subsequent electron acceleration of flares has also been carried out. The Chapter[1] takes up a question of what radio emission is produced by electrons at the very acceleration site of a solar flare. Specifically, the incoherent radio emission produced within two competing acceleration models—stochastic acceleration by cascading MHD turbulence and regular acceleration in collapsing magnetic traps has been calculated. This analysis clearly demonstrates that the radio emission from the acceleration sites (1) has sufficiently strong intensity to be observed by currently available radio instruments and (2) has spectra and light curves which are distinctly different in these two competing models, which makes them observationally distinguishable. In particular, it is suggested that some of the narrowband microwave and decimeter continuum bursts may be a signature of the stochastic acceleration in solar flares.

6.1 Introduction

Acceleration of charged particles is an internal property of energy release in solar flares, which has not yet been fully understood in spite of the significant progress achieved recently (e.g., Aschwanden 2002; Vilmer & MacKinnon 2003). A traditional way of getting information on the accelerated electrons in flares is the analysis of the HXR emission produced by nonthermal bremsstrahlung. However, because the bremsstrahlung intensity

[1]This chapter is based on the following paper:
Li, Y., & Fleishman, G. D. 2009, ApJ., 701, L52

increases with the density of the ambient plasma, it is likely that in most cases the acceleration site and HXR emission site are spatially separated; therefore, the HXR emission does not carry direct information on the acceleration site. This concept of distinct acceleration, propagation, and emission regions was then inherited by solar radio astronomy (e.g., Fig. 9 in Bastian et al. 1998), which looks relevant to relatively weak events of electron acceleration visualized by coherent emission of type III groups and of accompanying metric spikes (e.g., Fig. 10 in Bastian et al. 1998).

However, it is well known that a charged particle produces electromagnetic emission as it moves with acceleration. Stated another way, fast electrons must produce radiation immediately at the acceleration region with intensity and other characteristics defined by the type of the acceleration, or more precisely, by the type of fast electron trajectories in the acceleration region. This Chapter shows that typically this emission has a spectral peak at the microwave range, which makes the radio observation the most suitable to studying the acceleration region in flares.

By now, a huge variety of acceleration mechanisms and models has been proposed and developed for the solar flares. Acceleration by DC electric fields, both sub-Dreicer and super-Dreicer, (Holman 1985; Tsuneta 1985; Holman & Benka 1992; Litvinenko 1996, 2000, 2003); stochastic acceleration by turbulent waves (Hamilton & Petrosian 1992; Petrosian et al. 1994; Miller et al. 1996; Miller 1997; Park et al. 1997; Pryadko & Petrosian 1998; Bykov & Fleishman 2009), the classical diffusive shock acceleration (Aschwanden 2002); the regular (betatron plus Fermi) acceleration in collapsing magnetic traps (Somov & Kosugi 1997; Somov & Bogachev 2003; Karlický & Kosugi 2004; Bogachev & Somov 2005, 2007, 2009)$---$ all currently are considered in the context of solar flares.

To illustrate potential ability of radio observations to detect the radiation from the flare acceleration site and to distinguish them between competing acceleration mechanisms, radio emission generated within two distinct acceleration models—stochastic acceleration by a turbulence spectrum and regular acceleration in collapsing traps has been calculated. Radio emission of flares is known to be produced by a variety of emission mechanisms including gyrosynchrotron (GS) emission, bremsstrahlung, transition radiation, and a number of coherent radiative processes (Bastian et al. 1998; Nindos et al. 2008). Some of the observed emission types can in fact originate from acceleration sites, while others from electrons trapped in closed magnetic loops or from electrons propagating along open field lines. Based on this analysis, it is suggested that some of the narrowband microwave and decimeter continuum bursts may be a signature of the stochastic acceleration in solar flares, while the collapsing trap acceleration must reveal itself in drifting to higher frequencies microwave GS bursts.

6.2 Radio Emission from a Region of Stochastic Acceleration

Basically, various models of stochastic acceleration differ from each other by the accelerating agent (the plasma or MHD eigen-mode responsible for the wave-particle energy exchange) and presence or absence of some pre-acceleration (injection) process. To be specific, it is assumed that a "pure" stochastic acceleration process when the electrons are accelerated directly from the thermal pool (Hamilton & Petrosian 1992; Miller et al. 1996), perhaps as a result of MHD turbulence cascading towards the smallest scales involved into resonant interaction of the waves with thermal or weakly superthermal electrons.

Within this model the MHD turbulence is created at some large scale and then a

broad spectrum of the turbulence develops due to the turbulence cascading. As soon as small-scale waves capable of resonant interaction with electrons from a Maxwellian tail are produced they start to accelerate those electrons. This process can be modeled by growing a power-law tail (cf., e.g. spectra of accelerated electrons presented by Hamilton & Petrosian 1992; Miller et al. 1996; Bykov & Fleishman 2009)

$$N(E) = (\delta(t)-1)\frac{n(>E_0)\cdot E_0^{\delta(t)-1}}{E^{\delta(t)}}\exp\left(-\frac{E}{E_{br}(t)}\right) \tag{6.1}$$

where the time-dependent acceleration is modeled by increasing the break energy $E_{br}(t)$ and hardening the energy spectrum (decreasing spectral index $\delta(t)$). This nonthermal distribution of accelerated electrons is assumed to match the original Maxwellian distribution at a certain energy E_0; $n(>E_0)$ is evidently defined by the matching condition:

$$n(>E_0) = \frac{2n_e}{\delta(t)-1}\sqrt{\frac{E_0^3}{\pi(kT_e)^3}}\cdot\exp\left(\frac{-E_0}{kT_e}\right)\exp\left(\frac{E_0}{E_{br}(t)}\right) \tag{6.2}$$

where n_e and T_e are the number density and temperature of the thermal electrons, k is the Boltzman constant. Figure 6.1 shows a sequence of the electron spectra as the electron acceleration progresses.

The radio emission produced by accelerated electrons with the spectrum (6.1) at the acceleration region is considered. GS emission by nonrelativistic and weakly relativistic electrons available during an initial phase of the acceleration modeled by Eq. (6.1) is inefficient; the flux of the GS emission remains typically very small until a sufficient number of electrons are accelerated up to a few hundred keV[2] (Bastian et al. 1998). However, along

[2]In case of big flares, large numbers of GS-producing electrons can already be generated

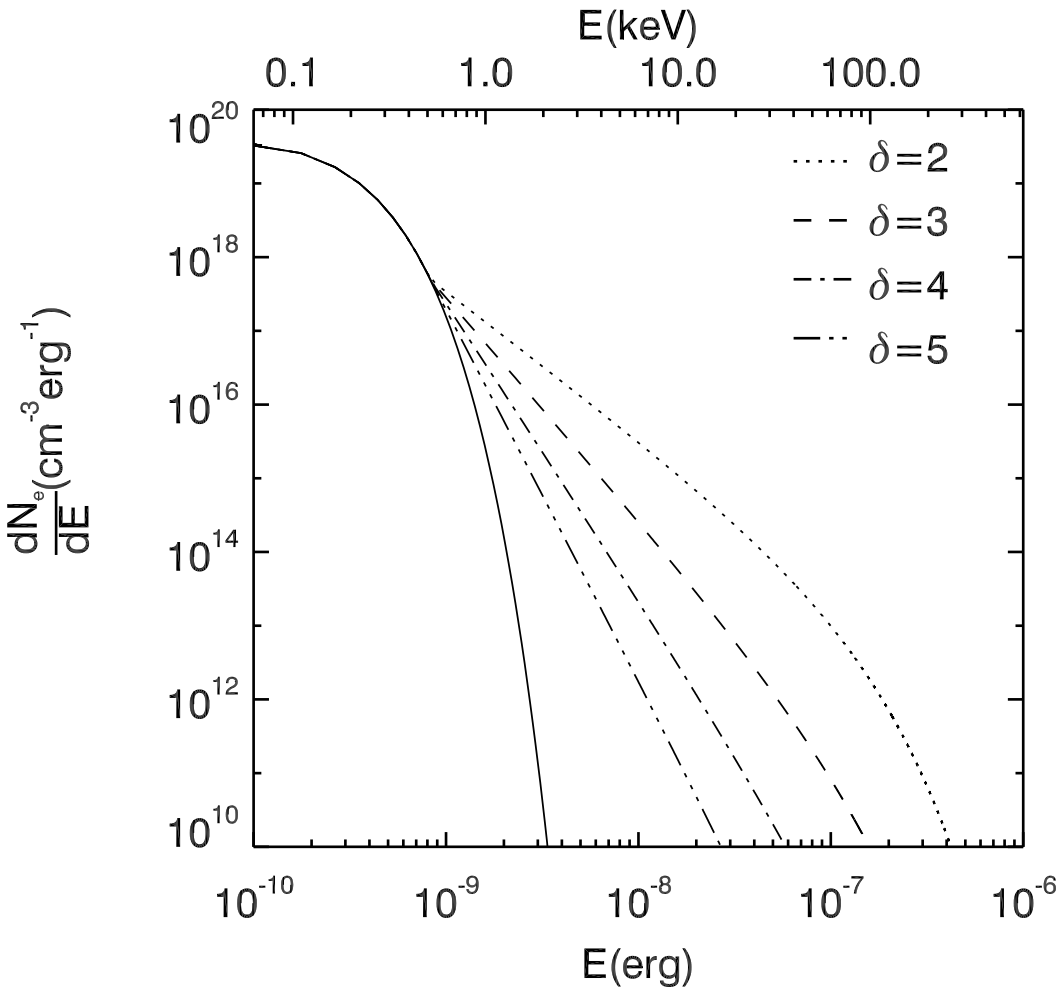

Figure 6.1 Distribution function of electrons for different δ and the following parameters: the thermal electron number density $n_e = 10^{10}$ cm^{-3}; the electron temperature $T_e = 10^6$ K; the matching energy is $E_0 = 6kT_e$. The solid curve denotes the original Maxwellian distribution.

with the regular magnetic field, there is a spectrum of turbulent waves (those accelerating the electrons) at the acceleration site. The nonthermal electrons, interacting with those random waves, experience spatial diffusion and so produce so-called diffusive synchrotron radiation (DSR, Fleishman 2006), which is calculated here.

Neglected the plasma gyrotropy for simplicity the refractive index of the radio waves can be taken in the form

$$n_\sigma = \sqrt{\varepsilon} \qquad \varepsilon = 1 - \frac{\omega_{pe}^2}{\omega^2} \qquad \omega_{pe} = \sqrt{\frac{4\pi e^2 n_e}{m}} \tag{6.3}$$

Then, the spectral and angular distribution of the energy radiated by a relativistic charged particle with a given Fourier transformed acceleration $\mathbf{w}_{\omega'}$ during time T of the particle motion in an external field is given by (Landau & Lifshitz 1971)

$$\mathscr{E}_{\mathbf{n},\omega} = \sqrt{\varepsilon}\frac{Q^2}{c^3}\left(\frac{\omega}{\omega'}\right)^4 \left|\left[\mathbf{n}\left[\left(\mathbf{n}-\frac{\mathbf{v}}{c}\right)\mathbf{w}_{\omega'}\right]\right]\right|^2 \tag{6.4}$$

where

$$\omega' = \omega\left(1 - \frac{\mathbf{nv}}{c}\sqrt{\varepsilon(\omega)}\right) \tag{6.5}$$

In the nonrelativistic case $v/c \ll 1$ ($\gamma \equiv \sqrt{1-v^2/c^2} \approx 1$) and $\omega' \approx \omega$, Equation 6.4 reduces to

---

during a preflare phase (Asai et al. 2006). In such cases an even earlier stage of acceleration (e.g., Battaglia et al. 2009), when the 100 keV electrons are not yet numerous.

$$\mathscr{E}_{\mathbf{n},\omega} = \sqrt{\varepsilon}\frac{Q^2}{c^3}\left|[\mathbf{n}\times\mathbf{w}_\omega]\right|^2 \tag{6.6}$$

where Q is the particle charge and $\mathbf{n}$ is the unit wave vector of the radiation. Equation 6.6 shows that the radiation in a given direction $\mathbf{n}$ is defined by the acceleration component $|\mathbf{w}_{\omega\perp}|^2 = |[\mathbf{n}\times\mathbf{w}_\omega]|^2$ transverse to $\mathbf{n}$. Similarly to the derivation in ultrarelativistic case (Fleishman 2006), the transverse component of the acceleration can be expressed via temporal and spatial Fourier transform of the external Lorentz force, $F^{\alpha}_{q_0,\mathbf{q}}$

$$|\,\mathbf{w}_{\omega\perp}\,|^2 = \frac{(2\pi)^3}{M^2V}\int dq_0 d\mathbf{q}\,\delta(\omega - q_0 + \mathbf{qv})(\delta_{\alpha\beta} - n_\alpha n_\beta)F^{\alpha}_{q_0,\mathbf{q}}F^{\beta *}_{q_0,\mathbf{q}} \tag{6.7}$$

where M is the mass of emitting particle and V is the source volume.

For electric component of the Lorenz force $\mathbf{F} = Q\mathbf{E}$

$$(\delta_{\alpha\beta} - n_\alpha n_\beta)F^{\alpha}_{q_0,\mathbf{q}}F^{\beta *}_{q_0,\mathbf{q}} = Q^2(\delta_{\alpha\beta} - n_\alpha n_\beta)E^{\alpha}_{q_0,\mathbf{q}}E^{\beta *}_{q_0,\mathbf{q}} \tag{6.8}$$

where

$$E^{\alpha}_{q_0,\mathbf{q}}E^{\beta *}_{q_0,\mathbf{q}} = \frac{TV}{(2\pi)^4}K_{\alpha\beta}(q_0,\mathbf{q}) \tag{6.9}$$

$K_{\alpha\beta}(q_0,\mathbf{q})$ is the correlation tensor of the random electric field, such as $\int dq_0 d\mathbf{q} K_{\alpha\alpha}(q_0,\mathbf{q}) = \left\langle E^2_{st}\right\rangle$ (Toptygin 1985).

For magnetic component of the Lorenz force the corresponding expression is different

$$(\delta_{\alpha\beta}-n_\alpha n_\beta)F^{\alpha}_{q_0,\mathbf{q}}F^{\beta *}_{q_0,\mathbf{q}}=\frac{Q^2}{c^2}\left(v^2\delta_{\alpha\beta}-v_\alpha v_\beta-[\mathbf{n}\times\mathbf{v}]_\alpha[\mathbf{n}\times\mathbf{v}]_\beta\right)B^{\alpha}_{q_0,\mathbf{q}}B^{\beta *}_{q_0,\mathbf{q}}$$

$$=Q^2\frac{v^2}{c^2}\left(n_\alpha n_\beta+\frac{(\mathbf{nv})^2}{v^2}\delta_{\alpha\beta}-(\mathbf{nv})\frac{v_\alpha n_\beta+n_\alpha v_\beta}{v^2}\right)B^{\alpha}_{q_0,\mathbf{q}}B^{\beta *}_{q_0,\mathbf{q}} \tag{6.10}$$

Similarly to Equation 6.9,

$$B^{\alpha}_{q_0,\mathbf{q}}B^{\beta *}_{q_0,\mathbf{q}}=\frac{TV}{(2\pi)^4}K_{\alpha\beta}(q_0,\mathbf{q}) \tag{6.11}$$

where $K_{\alpha\beta}(q_0,\mathbf{q})$ is the correlation tensor of the random magnetic field, such as $\int dq_0 d\mathbf{q} K_{\alpha\alpha}(q_0,\mathbf{q})=\left\langle B^2_{st}\right\rangle$. Thus, the DSR intensity, $I_{\mathbf{n},\omega}=\mathscr{E}_{\mathbf{n},\omega}/T$, of a nonrelativistic particle in the presence of a random magnetic field is

$$I_{\mathbf{n},\omega}=\sqrt{\varepsilon}\frac{Q^4v^2}{2\pi M^2c^5}\int dq_0 d\mathbf{q}\,\delta(\omega-q_0+\mathbf{qv})\left(n_\alpha n_\beta+\frac{(\mathbf{nv})^2}{v^2}\delta_{\alpha\beta}-(\mathbf{nv})\frac{v_\alpha n_\beta+n_\alpha v_\beta}{v^2}\right)K_{\alpha\beta}(q_0,\mathbf{q}) \tag{6.12}$$

This expression is valid for an arbitrary spectrum of magnetic turbulence including anisotropic distributions.

The DSR produced by accelerated nonrelativistic electrons interacting with the MHD turbulence is considered here. In MHD waves $E\sim(v_a/c)B$, where v_a is the Alfvén speed, therefore the magnetic part of the Lorenz force is larger than the electric part for all electrons with $v>v_a$. Assumed this condition to be fulfilled, only the DSR related to the magnetic field of the MHD turbulence is calculated; inclusion of electric field effect will further increase the DSR intensity.

Since the overall spectral shapes and flux level of the DSR are of interest, rather than model-dependent details of the emission, the simplest case of the isotropic MHD turbulence is considered here:

$$K_{\alpha\beta} = \frac{1}{2}\left(\delta_{\alpha\beta} - \frac{q_\alpha q_\beta}{q^2}\right) K(\mathbf{q})\delta(q_0 - q_0(\mathbf{q})) \tag{6.13}$$

As assumed $v > v_a$, i.e., the electrons move faster than the waves, the MHD turbulence to be quasi static, $q_0(\mathbf{q}) = 0$ is adopted. When the MHD turbulence is isotropic, the accelerated electrons are isotropic as well, and so the radiation produced is also isotropic. Thus, further the radiation produced into the full solid angle is considered

$$I_\omega = \int I_{\mathbf{n},\omega} d\Omega = \sqrt{\varepsilon}\frac{8Q^2}{3\pi c} \cdot q(\omega) \tag{6.14}$$

where, as in the ultrarelativistic case (Fleishman 2006), the scattering rate of the nonrelativistic particle by MHD turbulence $q(\omega)$ is introduced:

$$q(\omega) = \frac{\pi}{4}\left(\frac{Q}{Mc}\right)^2 \frac{v^2}{c^2} \int K(\mathbf{q})\delta(\omega + \mathbf{qv})\, d\mathbf{q} \tag{6.15}$$

To proceed further, the shape of the turbulence spectrum $K(\mathbf{q})$ is specified; a single power-law down to the smallest (resonant to thermal electrons) scales is applied:

$$K(\mathbf{q}) = \frac{A_\nu}{q^{\nu+2}} \qquad A_\nu = \frac{\nu - 1}{4\pi} k_0^{\nu-1} \langle B_{st}^2 \rangle \tag{6.16}$$

where $k_0 = 2\pi/L_0$ with L_0 being the largest turbulence scale, $\langle B_{st}^2 \rangle$ is the mean square of the turbulent magnetic field, and ν is the turbulence spectral index.

Then, substituting 6.15 into 6.16, integrating over $d\mathbf{q}$,

$$\int d\mathbf{q}K(\mathbf{q})\delta(\omega+\mathbf{qv}) = 2\pi\int d\cos\theta\cdot dq\frac{A_\nu}{q^\nu}\delta(\omega+qv\cos\theta) = \frac{2\pi A_\nu}{v}\int\limits_{\frac{\omega}{v}}^{\frac{\omega_{pe}}{v_{pe}}}\frac{dq}{q^{\nu+1}} \tag{6.17}$$

$$= \frac{2\pi}{\nu}\frac{A_\nu}{v}\left(\frac{v}{\omega}\right)^\nu\left(1-\left(\frac{\omega v_{pe}}{\omega_{pe}v}\right)^\nu\right)\Theta\left(\frac{\omega_{pe}}{v_{pe}}-\frac{\omega}{v}\right)$$

where

$$v_{pe} = 6.74\times10^5\sqrt{T_e} \tag{6.18}$$

is the thermal velocity of the plasma electrons, $\Theta(x)$ is the step function, and using the electron charge e and mass m for Q and M, it is found

$$q(\omega) = \frac{\pi^2 A_\nu}{2\nu}\frac{e^2\nu}{m^2c^4}\left(\frac{v}{\omega}\right)^\nu\left(1-\left(\frac{\omega v_{pe}}{\omega_{pe}v}\right)^\nu\right)\Theta\left(\frac{\omega_{pe}}{v_{pe}}-\frac{\omega}{v}\right) \tag{6.19}$$

so the DSR spectrum produced by accelerated electrons reads

$$I_\omega = \frac{8e^2}{3\pi c}\sqrt{\varepsilon}\cdot q(\omega) \tag{6.20}$$

Now the DSR power from N electrons with the spectrum described by Equation 6.1 is calculated

$$P_\omega = \int\limits_{E_0}^{\infty} I_\omega N(E)\,dE \tag{6.21}$$

In fact, the radio flux observed at the Earth is of interest. To transform this radiation

power into the flux observed at the Earth, the variable is changed $\omega = 2\pi f$, so that $I_f = 2\pi I_\omega$. Then, the flux is

$$F_f = \frac{2\pi P_\omega V}{4\pi R_{au}^2} = \frac{P_\omega L^3}{2R_{au}^2} \cdot 10^{19} \quad \text{sfu} \tag{6.22}$$

where $R_{au} = 1$ au$= 1.49 \times 10^{13}$ cm is the distance from the Earth to the Sun.

To evaluate the DSR from the acceleration region of a solar flare, some typically assumed parameters of the acceleration site are adopted as follows: (a) the size of the site $L \sim 10^8$ cm; (b) the thermal electron number density $n_e \sim 10^{10}$ cm^{-3}; (c) the electron temperature $T_e \sim 10^6$ K; (d) the energy density of the magnetic turbulence $W_{st} = \frac{\langle B_{st}^2 \rangle}{8\pi} \sim 10^3$ erg/cm^3. Accordingly, the total energy, $W_{tot} \sim W_{st} L^3 \sim 10^{27}$ ergs, corresponds to a very modest solar flare. It is assumed that the power-law tail of the accelerated electrons grows from $E_0 = (4-6)kT_e$ with $n(> E_0)$ specified by matching condition 6.2 and as the acceleration has started, the power law index δ changes from $8 \sim 3$ while the break energy E_{br} increases from $50 \sim 500$ keV.

Figure 6.2 presents the sequence of calculated DSR spectra for 11 different δ values from $7 \sim 3$; the spectra are calculated for three different ν values and for two different E_0 values. The blue curves indicate larger δ, while the red ones show smaller δ. Then, Figure 6.3(a) presents the DSR spectra for three different temperature values, $T = (1,3,10) \cdot 10^6 K$. In addition to spectrum shapes, light curves of the radiation at different frequencies can be informative. To estimate the light curve behavior a soft-hard-soft spectrum evolution is applied as follows from theory of spectrum evolution for the stochastic acceleration (Bykov & Fleishman 2009), and, as is typical for impulsive flares, with the electron energy spectral index $\delta(t)$ changing from 8 to 3 and then back to 8, while the

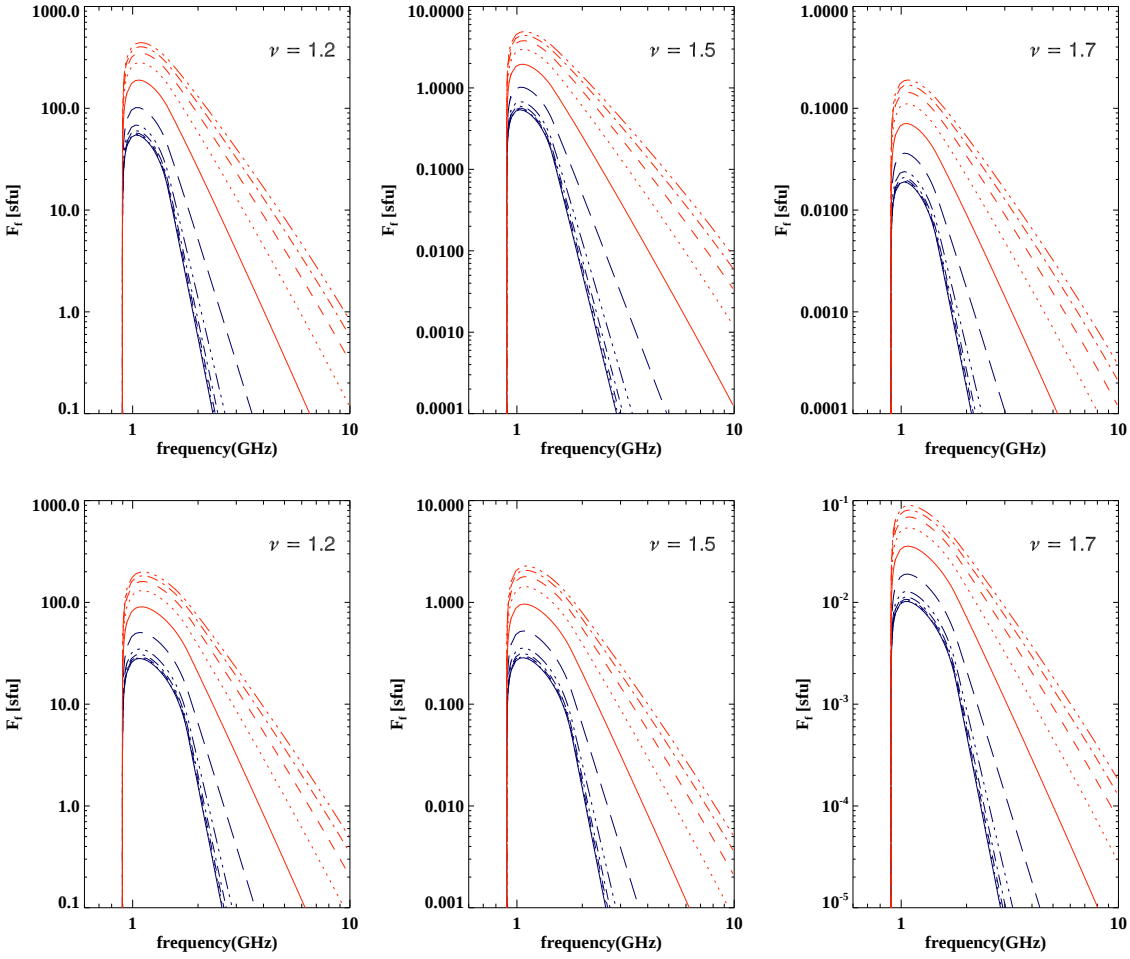

Figure 6.2 The DSR total flux density spectra calculated for the observations from the Earth surface for $E_0 = 4kT$ (upper panel) and $E_0 = 6kT$ (lower panel) for 11 different δ from $7 \sim 3$ and three different ν, indicated in the panels. The blue curves indicate larger δ, while the red ones show smaller δ.

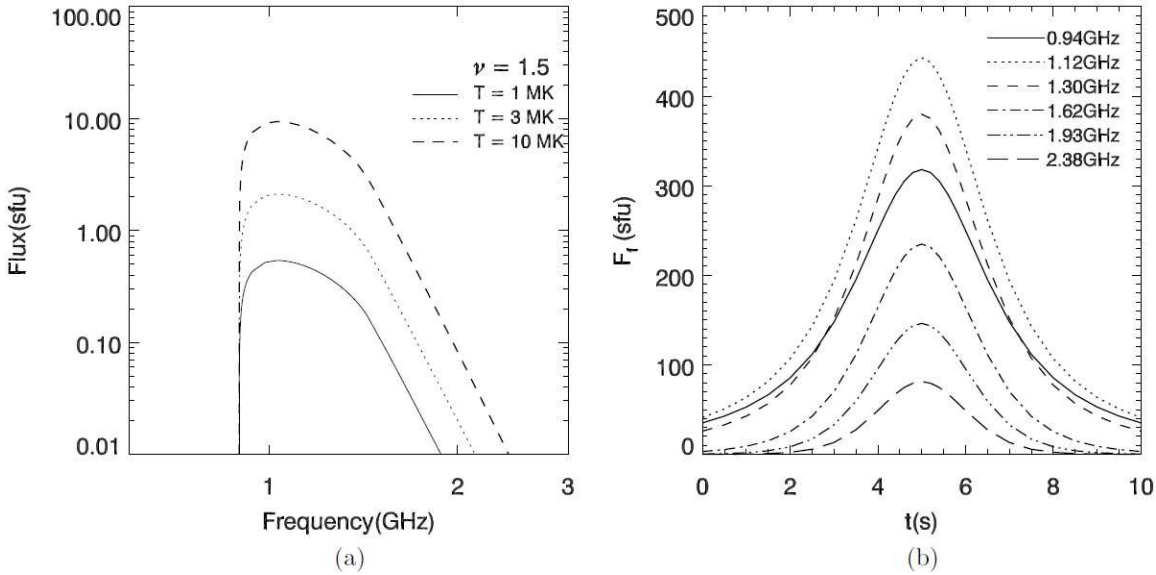

Figure 6.3 (a) DSR spectra for three sources with $\delta = 7$, $E_0 = 4kT_e$, and different electron temperatures, $T_e = (1,\ 3,\ 10) \cdot 10^6$ K; (b) DSR light curves for the case $E_0 = 4kT_e$, $\nu = 1.2$, $E_{br} = \left(E_{br}(t=0) + \frac{dE_{br}}{dt} \cdot t\right)$ keV, where $E_{br}(t=0) = 50$ keV, $\frac{dE_{br}}{dt} = 45$ keV/s, and soft-hard-soft evolution of the accelerated electron spectrum, $\delta = \delta_{\max} + a \cdot (t - t_0)^2$, where $\delta_{\max} = 3$, $t_0 = 5$ s, and $a = 0.2$ s^{-2}. The apparent symmetry of the model light curves is provided by assumed symmetry of the spectral index variation and adopted no variation of MHD spectrum; relaxing any of these assumption will result in asymmetric light curves. All the light curves peak almost simultaneously, so no "cross-correlation" delay is expected, although onset of higher frequency light curves is delayed, thus, the total duration of higher frequency emission is shorter.

break energy E_{br} increases all the way from 50 keV to $\sim$ 1 MeV. Figure 6.3(b) shows the corresponding model light curves at a few frequencies around the spectrum peak. One can note from the figure that higher frequency light curves have a somewhat shorter duration, although peaking at the same time; so no appreciable time delay between the light curves is expected.

It is noted that he DSR spectra are very narrowband, much narrower than typical GS spectra. The high frequency slope of the DSR spectrum can easily be evaluated from Equations 6.22, 6.21, 6.19, and 6.20, $F_f \propto f^{3-2\delta}$. Thus, the DSR high frequency spectral index varies from 11 to 3 as the spectral index of accelerated electrons changes from 7 to 3, while the GS spectral index would vary from 5 to 1 for the same range of δ variation. The peak flux of the DSR is highly sensitive to the turbulence spectral index (specified eventually by the MHD cascading law), while it is less sensitive to the plasma temperature and electron spectral index. The peak flux can be very large (up to a few hundred sfu), which makes it easily observable even by full sun radio instruments. If so, the corresponding radio emission must have been widely observed by available radio spectrometers working in the decimetric and/or microwave range. Indeed, there is a class of radio bursts with the properties resembling the DSR properties described here—it is the class of narrowband decimetric and microwave continuum bursts (including type IVdm), which, is suggested that, may contain burst-candidates to the radio emission from the regions of stochastic acceleration in solar flares. Although this interpretation is tempting, spatially resolved radio observations of the DSR will be needed to confirm it, to locate the region of stochastic acceleration, and study it in detail. Another plausible candidate for radio emission from stochastic acceleration episodes is so-called transient brightenings, whose radio spectra are

often narrowband (Gary et al. 1997).

6.3 Gyrosynchrotron Radio Emission from a Collapsing Trap

Another model, a collapsing magnetic trap, is considered which can efficiently accelerate charged particles. Unlike the stochastic acceleration models, no turbulence spectrum is essential to accelerate particles in the collapsing trap model; however, some spectrum of "pre-accelerated" particles is needed, otherwise, the collapse of the trap will only give rise to plasma heating without nonthermal particle generation.

Therefore, it is assumed that just before collapsing the trap contained both thermal plasma and nonthermal electron population with a power-law spectrum. To be specific, the initial conditions are adopted as follows: (a) the magnetic field strength $B_0 = 30$ G; (b) the minimum and the maximum energy of the power-law spectrum $E_{\min} = 0.01$ MeV, $E_{\max} = 1$ MeV; (c) the thermal electron density $n_{th} = 10^9$ cm^{-3} and the non-thermal electron density $n_{rl} = 10^7$ cm^{-3}; (d) the source size $L_0 = 10$".

During the trap contraction, the number of accelerated electrons evolves. For the modeling a solution obtained by Bogachev & Somov (2005) is adopted (see Figure 6.4), which takes into account the betatron and Fermi acceleration and the particle escape from the trap via the loss cone:

$$N = N_0 \frac{l\sqrt{b_m - b}}{\sqrt{1 + (b_m - 1)l^2}} \tag{6.23}$$

where

$$b = b(t) = B(t)/B_0 \tag{6.24}$$

$$l = l(t) = L(t)/L_0 \tag{6.25}$$

so $b(t)$ changes from $b(0) = 1$ to $b_m = B_m/B_0$, B_m is the largest magnetic field value at the end of the trap collapse, and $l(t)$ deceases from $l(0) = 1$ to a very low value, say, $l(t_{\max}) = 0.1$. For the sake of simplicity a self-similar contraction of the collapsing magnetic trap is assumed. In this case, evolution of all parameters of the trap is uniquely defined by their initial values and the dimensionless source scale $l(t)$. Thus, for any given contraction law, $l(t)$, the corresponding time history of all other relevant source parameters can be easily calculated, as the magnetic field, the thermal electron number density, the source volume and the projected area, and the evolution of the nonthermal electron spectrum (Bogachev & Somov 2005, 2007). For the modeling it is adopted that the trap volume V linearly decreases with time during the trap contraction from $10''^3$ to $1''^3$; 10 s for the trap collapse time is adopted, which is a few Alfven times ($\tau_a \sim L/v_a$) for the trap parameters used.

Thus, the GS spectra at different time frames and the radio light curves at different frequencies within the adopted collapsing trap model can be straightforwardly calculated. Figure 6.4 displays the GS spectra at different moments of the trap contraction. In agreement with a statement made in the previous section, at initial phase of acceleration the GS flux is small (less than 1 sfu), which can only be recorded by high sensitivity spatially resolved observations. However, during the trap contraction the magnetic field increases and

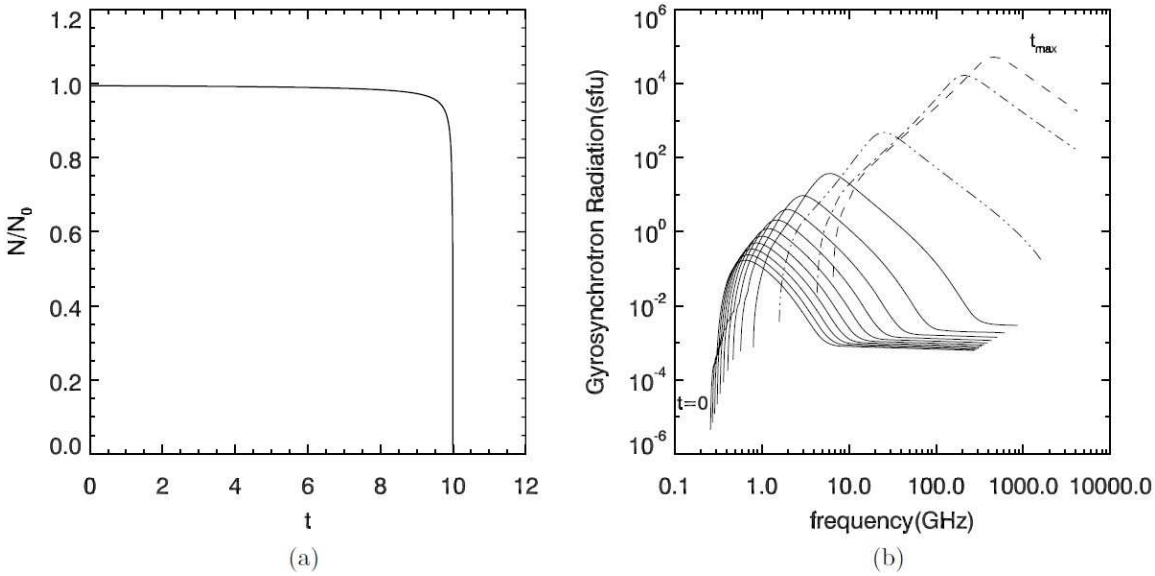

Figure 6.4 Left: The number of electrons in the trap according to the Bogachev & Somov (2005) model. Right: GS spectra in frequency range $0.1 \sim 10^4$ GHz; the solid spectra are plotted for $t = 0$, 1, ..., 9 s; the dashed-doted lines correspond to the end of collapse at $t = 9.75$, 9.975, 9.9975 s. In fact, both GS and free-free contributions to the radiation intensity are taken into account, however, the free-free component is inessential during the loop collapse: it is only noticeable at high frequency flat regions of the early spectra.

the fast electrons are accelerated, which all together lead to a significant increase of the peak flux and the peak frequency of the radio emission produced at the acceleration site; thus the radio emission becomes easily detectable by available radio instrument soon after the trap starts to contract.

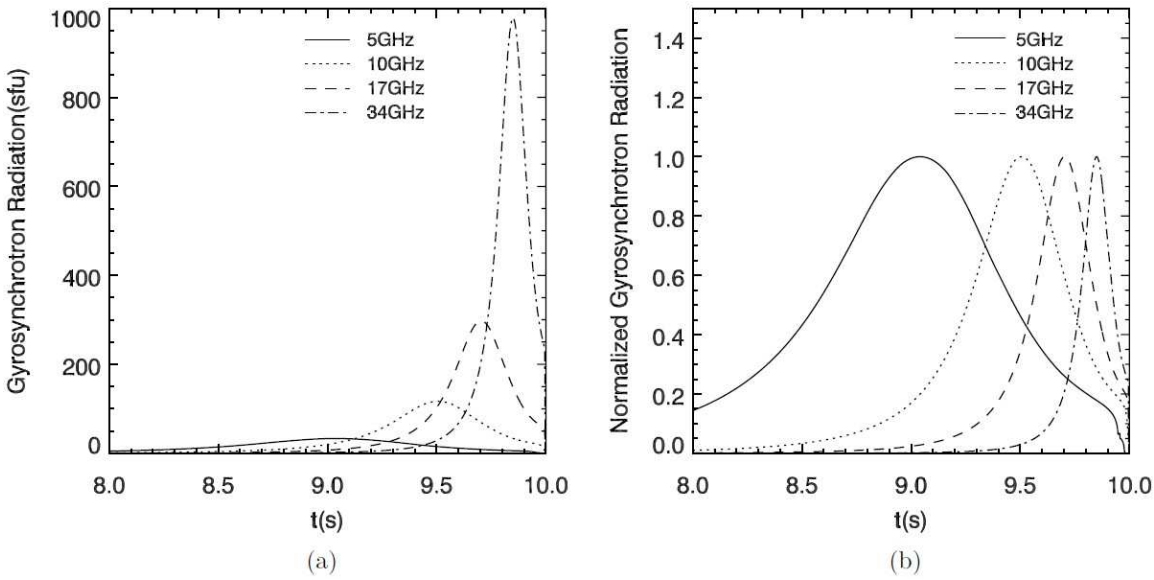

Figure 6.5 The light curves (a) and the normalized light curves (b) of the GS emission from a collapsing trap at a number of fixed frequencies 5, 10, 17, 34 GHz. The initial trap parameters and the contraction law are described in the text. A significant time delay between the light curves, comparable to duration of the light curves, is evident from the Figure.

Figure 6.5 presents the light curves of the emission at a number of fixed frequencies, 5, 10, 17, 34 GHz. Within the adopted model the peak flux increases with frequency, see Figures 6.4, 6.5; in fact, this increase may become less pronounced if the coulomb losses in the collapsing trap are taken into account (Bogachev & Somov 2009). A distinctive feature of the light curves, contrasting to that of DSR produced from the stochastic acceleration sites, is a noticeable time delay: the higher frequency light curves are delayed relative to lower frequency light curves; this time delay will be present even when the coulomb

losses (Bogachev & Somov 2009) are included. A time delay in the sense predicted by the modeling is frequently observed in solar flares, in particular, in those with quasiperiodic pulsations (Fleishman et al. 2008). Observationally, however, the GS emission from a collapsing trap can be contaminated by GS emission from trapped electrons produced by previous acceleration episodes, so unambiguous detection of the GS emission from a collapsing trap itself requires additional accurate analysis to separate the contributions, which as yet has not been performed.

6.4 Discussion

There are many models in which electrons can be accelerated to nonthermal energies. Some mechanisms accelerate a tiny fraction of the electrons, which can only be observed via coherent radio emissions (e.g., type III bursts produced by electron beams, or accompanying metric spikes), others produce more powerful acceleration, sufficient to generate observable incoherent radio emission from either the acceleration site itself or from a remote "radiation site".

The idea of using radio observations to probe energy release/acceleration regions in flares has been around for awhile (e.g., Bastian et al. 1998), however, the studies focused mainly on *coherent* decimeter radio bursts. For example, Benz (1986) argued that decimeter narrowband millisecond radio spike clusters can be a signature of electron acceleration in flares, and, if so, the flare energy release must have been highly fragmented with each spike indicating a single energy release/acceleration episode. However, it has been found (Aschwanden & Guedel 1992) that the radio spikes are frequently delayed compared with associated hard X-ray emission, implying the spikes are a secondary phenomenon associ-

ated with flares. Moreover, spatially resolved observations (Benz et al. 2002; Battaglia & Benz 2009) show that the spike sources are typically far away from main flare locations. Even though higher frequency microwave radio spikes (Fleishman et al. 2003; Rozhansky et al. 2008) can be produced at or around the main flare location, it seems doubtful that the coherent radio burst originate from elementary acceleration episodes (Fleishman & Mel'Nikov 1998; Fleishman et al. 2003; Rozhansky et al. 2008; Battaglia & Benz 2009).

In contrast, in this dissertation *incoherent* radio emission from the acceleration region of a solar flare within two distinct acceleration models—stochastic acceleration by cascading MHD turbulence and regular (betatron and Fermi) acceleration in a collapsing trap, have been calculated. It is demonstrated that the radio emissions produced within these two competing acceleration models are distinctly different, which potentially allows distinguishing between them by the radio observations. In particular, it is found that the stochastic acceleration process is accompanied by a very narrowband DSR continuum radio emission, whose predicted properties are generally consistent with observed properties of narrowband microwave or decimetric (type IVdm) continuum bursts, thus, it is suggested that some of those bursts can be produced from the sites of stochastic acceleration.

CHAPTER 7

SUMMARY OF THE DISSERTATION

This dissertation focuses on the rapid evolution of the magnetic environment in flare-productive active regions. The rapid topological change of sunspots has been a subject of intense research since it was discovered by NJIT/Space Weather Research Lab (SWRL) (Wang et al. 2004a; Deng et al. 2005; Liu et al. 2005) eight years ago. To better understand the physics mechanism behind the solar eruptions, the first comparison of the MHD modeling with real data is carried out. The observations and simulation are compared quantitatively in the context of evolution of 3D magnetic fields, and some solar eruption models are employed to qualitatively interpret the associated rapid changes in sunspot structure. In this study, there is fundamental progress in this research area. In the following, the major results are summarized.

The first morphology change is that the penumbral segments in the outer δ-spot structure decay rapidly after major flares, and meanwhile, the neighboring umbral cores and/or inner penumbral regions become darker. The rapid changes, which can be identified in the time profiles of WL mean intensity, are substantial and permanent and quite different from the overall sunspot evolution. They are temporally and spatially correlated with flares. No such rapid changes have been found in the absence of flares. Chen et al. (2007) investigated the statistical character of 403 events from 1998 May 9 to 2004 Jul 17, including 40 X-class, 174 M-class, and 189 C-class flares. Their main result suggests that the phenomenon of sunspot change associated with flares is more notable for larger events.

The second finding is the significant enhancement of transverse magnetic fields

shown with the co-aligned magnetic field observations in the darkened central areas at the flare PIL, while the transverse field associated with the penumbral decay areas deceases. These rapid changes are interpreted in terms of magnetic reconnection, which alters the magnetic field topology during flares. This significant enhancement of these near-surface transverse magnetic fields at the flaring PIL strongly supports the formation of low-lying field lines as a result of the reconnection. Furthermore, the observed rapid and permanent transverse field change can be naturally incorporated into the two-stage reconnection scenario.

The simplified reconnection picture of Liu et al. (2005) (Figure 7.1) described a scenario in which the two components of a δ spot become strongly connected after the flare. In the outer border of the δ-structure, the penumbral fields change from a highly inclined to a more vertical configuration, which leads to penumbral decay. The umbral core and inner penumbral region close to a neutral line become darker as a result of increased field strength there, mainly in the form of transverse fields.

The remote brightenings that occur early in the flare event well before the main HXR emissions signify the beginning of the reconnection between magnetic elbows of the sigmoid. The remote brightening areas that appear as additional flare ribbons, together with the ribbons at the flare core region, outline the overall sigmoidal configuration. Flare ribbon separation starts with a slow phase co-temporal with remote brightenings (the first stage of reconnection), followed by a fast phase when HXR emissions peaked (the second stage of reconnection). This two-stage magnetic reconnection, accounting for the sigmoid-to-arcade transformation, is discernible in Hα images.

Based on the tether-cutting flare model proposed by Moore et al. (2001), a tentative

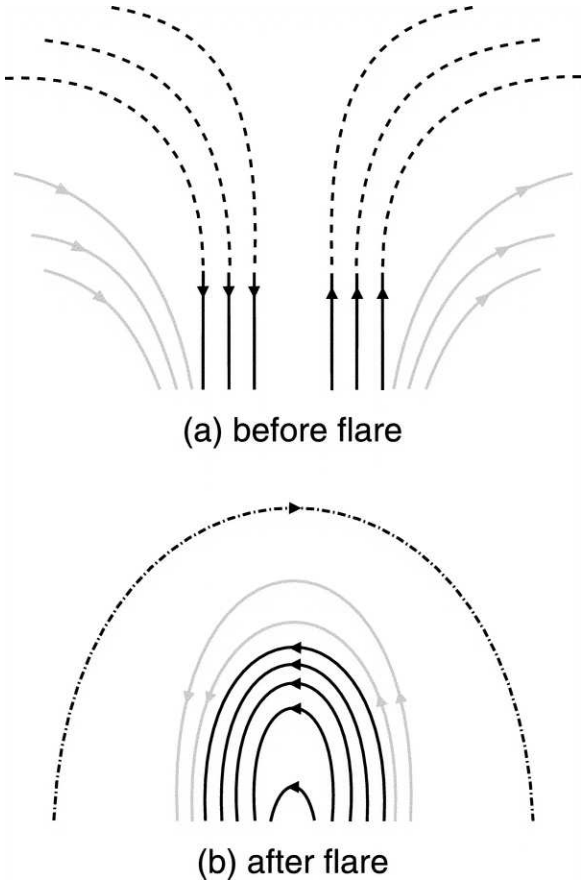

Figure 7.1 Schematic picture interpreting the observations. (a) Initial magnetic field configuration before the flare. Penumbral fields are in gray and umbral fields are in black. (b) Magnetic field configuration in the postflare state. The dash-dotted line represents the connection between two points far apart, which may form the large-scale arcade structure of CMEs. (Courtesy of Liu et al. (2005).)

flaring scenario links the sigmoidal active region to the appearance of ribbon-like hard X-ray sources. At the early phase of the eruption, tether-cutting reconnection occurs in the sigmoid core region where the magnetic fields are highly sheared. The hard X-ray emission appears as footpoint-like sources located at the foot of the sigmoidal loops. Later on, the reconnection between the sigmoidal loops results in a small loop below the coronal X-point and a large twisted flux loop above. The small loop actually protects the filament from disruption, while the large twisted flux loop erupts outward and blows away the envelope fields, following which reconnection occurs between the opened legs of the envelope fields. At this stage, the electrons are presumed to be accelerated in the whole coronal arcade, or in the local corona area then fan out through the arcade to bombard the dense chromosphere, leading to the ribbon-like hard X-ray emissions. The investigation of both observation and simulation confirms many aspects of this model.

It is demonstrated that radio emissions produced within two competing acceleration models are distinctly different, which potentially allows distinguishing between them by the radio observations. These two distinct acceleration models of the radio emission from the acceleration region of a solar flare are stochastic acceleration by cascading MHD turbulence and regular (betatron and Fermi) acceleration in a collapsing trap. In particular, it is found that the stochastic acceleration process is accompanied by a very narrowband DSR continuum radio emission, whose predicted properties are generally consistent with observed properties of narrowband microwave or decimetric (type IVdm) continuum bursts, thus, it is suggested that some of those bursts can be produced from the sites of stochastic acceleration.

As a concluding remark for this dissertation, the prospective for further studies is

outlined below:

- *The HMI onboard the SDO provides an unprecedented opportunity to explore the possible triggering mechanism of flare/CMEs using full-disk photospheric vector magnetograms with high spatial and temporal resolution. The extended study of the 3-D magnetic configuration and its evolution in the different phases of flares should be made;*

- *The numerical MHD modeling combined with specific observational data would lead to a fundamental improvement of the knowledge on solar explosive models. More quantitative analyses should be made in assessing the applicability of different flare models;*

- *Observational findings on the action of the Lorentz force on the solar atmosphere and the solar interior should be carefully checked to further understand the physical origins of sunquakes underlying solar eruption phenomena (Fisher et al. 2012).*

REFERENCES

Aly, J. J. 1991, Astrophys. J. Lett., 375, L61.

Antiochos, S. K., DeVore, C. R., & Klimchuk, J. A. 1999, Astrophys. J., 510, 485.

Anwar, B., Acton, L. W., Hudson, H. S., Makita, M., McClymont, A. N., & Tsuneta, S. 1993, Sol. Phys., 147, 287.

Asai, A., Nakajima, H., Shimojo, M., White, S. M., Hudson, H. S., & Lin, R. P. 2006, PASJ, 58, L1.

Aschwanden, M. J. 2002, Space Sci. Rev., 101, 1.

—. 2005, Physics of the Solar Corona. An Introduction with Problems and Solutions (2nd edition), ed. Aschwanden, M. J.

Aschwanden, M. J. & Guedel, M. 1992, Astrophys. J., 401, 736.

Aschwanden, M. J., Kosugi, T., Hanaoka, Y., Nishio, M., & Melrose, D. B. 1999, Astrophys. J., 526, 1026.

Balasubramaniam, K. S., Pevtsov, A. A., Neidig, D. F., Cliver, E. W., Thompson, B. J., Young, C. A., Martin, S. F., & Kiplinger, A. 2005, Astrophys. J., 630, 1160.

Bastian, T. S., Benz, A. O., & Gary, D. E. 1998, Annu. Rev. Astron. Astrophys., 36, 131.

Battaglia, M. & Benz, A. O. 2009, Astron. Astrophys., 499, L33.

Battaglia, M., Fletcher, L., & Benz, A. O. 2009, Astron. Astrophys., 498, 891.

Benz, A. O. 1986, Sol. Phys., 104, 99.

Benz, A. O., Saint-Hilaire, P., & Vilmer, N. 2002, Astron. Astrophys., 383, 678.

Bogachev, S. A. & Somov, B. V. 2005, Astronomy Letters, 31, 537.

—. 2007, Astronomy Letters, 33, 54.

—. 2009, Astronomy Letters, 35, 57.

Borrero, J. M., Tomczyk, S., Kubo, M., Socas-Navarro, H., Schou, J., Couvidat, S., & Bogart, R. 2011, Sol. Phys., 273, 267.

Bray, R. J. & Loughhead, R. E. 1979, Sunspots (New York: Dover Publications).

Bykov, A. M. & Fleishman, G. D. 2009, Astrophys. J. Lett., 692, L45.

Calabretta, M. R. & Greisen, E. W. 2002, Astron. Astrophys., 395, 1077.

Cameron, R. & Sammis, I. 1999, Astrophys. J. Lett., 525, L61.

Cassak, P. A., Drake, J. F., & Shay, M. A. 2006, Astrophys. J. Lett., 644, L145.

Chen, W.-Z., Liu, C., Song, H., Deng, N., Tan, C.-Y., & Wang, H.-M. 2007, Sol. Phys., 7, 733.

Cheng, X., Ding, M. D., Guo, Y., Zhang, J., Jing, J., & Wiegelmann, T. 2010, Astrophys. J. Lett., 716, L68.

Deng, N., Liu, C., Prasad Choudhary, D., & Wang, H. 2011, Astrophys. J. Lett., 733, L14.

Deng, N., Liu, C., Yang, G., Wang, H., & Denker, C. 2005, Astrophys. J., 623, 1195.

Fan, Y. 2010, Astrophys. J., 719, 728.

Fárník, F., Hudson, H. S., Karlický, M., & Kosugi, T. 2003, Astron. Astrophys., 399, 1159.

Fisher, G. H., Bercik, D. J., Welsch, B. T., & Hudson, H. S. 2012, Sol. Phys., 277, 59.

Fleishman, G. D. 2006, Astrophys. J., 638, 348.

Fleishman, G. D., Bastian, T. S., & Gary, D. E. 2008, Astrophys. J., 684, 1433.

Fleishman, G. D., Gary, D. E., & Nita, G. M. 2003, Astrophys. J., 593, 571.

Fleishman, G. D. & Mel'Nikov, V. F. 1998, Soviet Physics Uspekhi, 41, 1157.

Forbes, T. G. & Lin, J. 2000, Journal of Atmospheric and Solar-Terrestrial Physics, 62, 1499.

Forbes, T. G. & Priest, E. R. 1984, Sol. Phys., 94, 315.

—. 1995, Astrophys. J., 446, 377.

Franklin, J. 2005, Classical Electromagnetism (Pearson Education).

Gary, D. E., Hartl, M. D., & Shimizu, T. 1997, Astrophys. J., 477, 958.

Gibson, S. E. & Fan, Y. 2006, Journal of Geophysical Research (Space Physics), 111, 12103.

Guo, Y., Ding, M. D., Wiegelmann, T., & Li, H. 2008, Astrophys. J., 679, 1629.

Hale, G. E., Ellerman, F., Nicholson, S. B., & Joy, A. H. 1919, Astrophys. J., 49, 153.

Hamilton, R. J. & Petrosian, V. 1992, Astrophys. J., 398, 350.

Hanaoka, Y. 1999, PASJ, 51, 483.

Hart, A. B. 1956, Mon. Not. R. Astron. Soc., 116, 38.

Heyvaerts, J., Priest, E. R., & Rust, D. M. 1977, Astrophys. J., 216, 123.

Hirayama, T. 1974, Sol. Phys., 34, 323.

Holman, G. D. 1985, Astrophys. J., 293, 584.

Holman, G. D. & Benka, S. G. 1992, Astrophys. J. Lett., 400, L79.

Hudson, H. S., Fisher, G. H., & Welsch, B. T. 2008, in Astronomical Society of the Pacific Conference Series, Vol. 383, Subsurface and Atmospheric Influences on Solar Activity, ed. R. Howe, R. W. Komm, K. S. Balasubramaniam, & G. J. D. Petrie 221.

Ji, H., Huang, G., Wang, H., Zhou, T., Li, Y., Zhang, Y., & Song, M. 2006, Astrophys. J. Lett., 636, L173.

Ji, H., Wang, H., Liu, C., & Dennis, B. R. 2008, Astrophys. J., 680, 734.

Jiang, Y., Zheng, R., Yang, J., Hong, J., Yi, B., & Yang, D. 2012, Astrophys. J., 744, 50.

Jing, J., Wiegelmann, T., Suematsu, Y., Kubo, M., & Wang, H. 2008, Astrophys. J. Lett., 676, L81.

Kahler, S. W. 1982, J. Geophys. Res., 87, 3439.

Karlický, M. & Kosugi, T. 2004, Astron. Astrophys., 419, 1159.

Kirkpatrick, S., Gelatt, C. D., & Vecchi, M. P. 1983, Science, 220, 671.

Klimchuk, J. A. 1997, in Astronomical Society of the Pacific Conference Series, Vol. 111, Magnetic Reconnection in the Solar Atmosphere, ed. R. D. Bentley & J. T. Mariska319.

Kopp, R. A. & Pneuman, G. W. 1976, 50, 85.

Kosovichev, A. G. & Zharkova, V. V. 1998, Nature, 393, 317.

—. 2001, Astrophys. J. Lett., 550, L105.

Kosugi, T., Matsuzaki, K., Sakao, T., Shimizu, T., Sone, Y., Tachikawa, S., Hashimoto, T., Minesugi, K., Ohnishi, A., Yamada, T., Tsuneta, S., Hara, H., Ichimoto, K., Suematsu, Y., Shimojo, M., Watanabe, T., Shimada, S., Davis, J. M., Hill, L. D., Owens, J. K., Title, A. M., Culhane, J. L., Harra, L. K., Doschek, G. A., & Golub, L. 2007, Sol. Phys., 243, 3.

Kubo, M., Lites, B. W., Shimizu, T., & Ichimoto, K. 2008, Astrophys. J., 686, 1447.

Kundu, M. R., Bobrowsky, M., & Rust, D. M. 1983, Astrophys. J., 265, 1084.

Kurokawa, H., Wang, T., & Ishii, T. T. 2002, Astrophys. J., 572, 598.

Landau, L. D. & Lifshitz, E. M. 1971, The classical theory of fields, ed. Landau, L. D. & Lifshitz, E. M.

Lang, K. R. 2001, The Cambridge Encyclopedia of the Sun (Cambridge, UK: Cambridge University Press).

Leighton, R. B., Noyes, R. W., & Simon, G. W. 1962, Astrophys. J., 135, 474.

Leka, K. D., Barnes, G., Crouch, A. D., Metcalf, T. R., Gary, G. A., Jing, J., & Liu, Y. 2009, Sol. Phys., 260, 83.

Lin, R. P., Dennis, B. R., Hurford, G. J., Smith, D. M., Zehnder, A., Harvey, P. R., Curtis, D. W., Pankow, D., Turin, P., Bester, M., Csillaghy, A., Lewis, M., Madden, N., van Beek, H. F., Appleby, M., Raudorf, T., McTiernan, J., Ramaty, R., Schmahl, E., Schwartz, R., Krucker, S., Abiad, R., Quinn, T., Berg, P., Hashii, M., Sterling, R., Jackson, R., Pratt, R., Campbell, R. D., Malone, D., Landis, D., Barrington-Leigh, C. P., Slassi-Sennou, S., Cork, C., Clark, D., Amato, D., Orwig, L., Boyle, R., Banks, I. S., Shirey, K., Tolbert, A. K., Zarro, D., Snow, F., Thomsen, K., Henneck, R., McHedlishvili, A., Ming, P., Fivian, M., Jordan, J., Wanner, R., Crubb, J., Preble, J., Matranga, M., Benz, A., Hudson, H., Canfield, R. C., Holman, G. D., Crannell, C., Kosugi, T., Emslie, A. G., Vilmer, N., Brown, J. C., Johns-Krull, C., Aschwanden, M., Metcalf, T., & Conway, A. 2002, Sol. Phys., 210, 3.

Lites, B. W., Low, B. C., Martinez Pillet, V., Seagraves, P., Skumanich, A., Frank, Z. A., Shine, R. A., & Tsuneta, S. 1995, Astrophys. J., 446, 877.

Litvinenko, Y. E. 1996, Astrophys. J., 462, 997.

—. 2000, Sol. Phys., 194, 327.

Litvinenko, Y. E. 2003, in Lecture Notes in Physics, Berlin Springer Verlag, Vol. 612, Energy Conversion and Particle Acceleration in the Solar Corona, ed. L. Klein213–229.

Liu, C., Deng, N., Liu, R., Lee, J., Wiegelmann, T., Jing, J., Xu, Y., Wang, S., & Wang, H. 2012, Astrophys. J. Lett., 745, L4.

Liu, C., Deng, N., Liu, Y., Falconer, D., Goode, P. R., Denker, C., & Wang, H. 2005, Astrophys. J., 622, 722.

Liu, C., Lee, J., Deng, N., Gary, D. E., & Wang, H. 2006, Astrophys. J., 642, 1205.

Liu, C., Lee, J., Jing, J., Liu, R., Deng, N., & Wang, H. 2010, Astrophys. J. Lett., 721, L193.

Liu, C., Lee, J., Karlický, M., Prasad Choudhary, D., Deng, N., & Wang, H. 2009, Astrophys. J., 703, 757.

Liu, C., Lee, J., Yurchyshyn, V., Deng, N., Cho, K.-s., Karlický, M., & Wang, H. 2007, Astrophys. J., 669, 1372.

Lynch, B. J., Antiochos, S. K., MacNeice, P. J., Zurbuchen, T. H., & Fisk, L. A. 2004, Astrophys. J., 617, 589.

Manoharan, P. K., van Driel-Gesztelyi, L., Pick, M., & Demoulin, P. 1996, Astrophys. J. Lett., 468, L73.

Martínez-Oliveros, J. C. & Donea, A.-C. 2009, Mon. Not. R. Astron. Soc., 395, L39.

Martres, M. J. 1989, Sol. Phys., 119, 357.

McIntosh, P. S. 1990, Sol. Phys., 125, 251.

Melrose, D. B. 1997, Astrophys. J., 486, 521.

Metcalf, T. R. 1994, Sol. Phys., 155, 235.

Metcalf, T. R., De Rosa, M. L., Schrijver, C. J., Barnes, G., van Ballegooijen, A. A., Wiegelmann, T., Wheatland, M. S., Valori, G., & McTtiernan, J. M. 2008, Sol. Phys., 247, 269.

Metcalf, T. R., Leka, K. D., Barnes, G., Lites, B. W., Georgoulis, M. K., Pevtsov, A. A., Balasubramaniam, K. S., Gary, G. A., Jing, J., Li, J., Liu, Y., Wang, H. N., Abramenko, V., Yurchyshyn, V., & Moon, Y.-J. 2006, Sol. Phys., 237, 267.

Metcalf, T. R., Leka, K. D., & Mickey, D. L. 2005, Astrophys. J. Lett., 623, L53.

Miller, J. A. 1997, Astrophys. J., 491, 939.

Miller, J. A., Larosa, T. N., & Moore, R. L. 1996, Astrophys. J., 461, 445.

Moore, R. L. & Labonte, B. J. 1980, in IAU Symposium, Vol. 91, Solar and Interplanetary Dynamics, ed. M. Dryer & E. Tandberg-Hanssen207–210.

Moore, R. L., Sterling, A. C., Hudson, H. S., & Lemen, J. R. 2001, Astrophys. J., 552, 833.

Moreton, G. E. & Ramsey, H. E. 1960, PASP, 72, 357.

Nakajima, H., Dennis, B. R., Hoyng, P., Nelson, G., Kosugi, T., & Kai, K. 1985, Astrophys. J., 288, 806.

Nindos, A., Aurass, H., Klein, K.-L., & Trottet, G. 2008, Sol. Phys., 253, 3.

Park, B. T., Petrosian, V., & Schwartz, R. A. 1997, Astrophys. J., 489, 358.

Pearce, G. & Harrison, R. A. 1990, Astron. Astrophys., 228, 513.

Petrie, G. J. D. & Sudol, J. J. 2010, Astrophys. J., 724, 1218.

Petrosian, V., McTiernan, J. M., & Marschhauser, H. 1994, Astrophys. J., 434, 747.

Priest, E. & Forbes, T. 2000, Irish Astronomical Journal, 27, 235.

Pryadko, J. M. & Petrosian, V. 1998, Astrophys. J., 495, 377.

Qiu, J. 2009, Astrophys. J., 692, 1110.

Qiu, J. & Yurchyshyn, V. B. 2005, Astrophys. J. Lett., 634, L121.

Richardson, R. S. 1951, Astrophys. J., 114, 356.

Rozhansky, I. V., Fleishman, G. D., & Huang, G.-L. 2008, Astrophys. J., 681, 1688.

Sakao, T., Kosugi, T., & Masuda, S. 1998, in Astrophysics and Space Science Library, Vol. 229, Observational Plasma Astrophysics : Five Years of YOHKOH and Beyond, ed. T. Watanabe & T. Kosugi273.

Schrijver, C. J., De Rosa, M. L., Metcalf, T., Barnes, G., Lites, B., Tarbell, T., McTiernan, J., Valori, G., Wiegelmann, T., Wheatland, M. S., Amari, T., Aulanier, G., Démoulin, P., Fuhrmann, M., Kusano, K., Régnier, S., & Thalmann, J. K. 2008, Astrophys. J., 675, 1637.

Schrijver, C. J., De Rosa, M. L., Metcalf, T. R., Liu, Y., McTiernan, J., Régnier, S., Valori, G., Wheatland, M. S., & Wiegelmann, T. 2006, Sol. Phys., 235, 161.

Shen, J., Zhou, T., Ji, H., Wang, N., Cao, W., & Wang, H. 2008, Astrophys. J. Lett., 686, L37.

Shibata, K. 1996, Advances in Space Research, 17, 9.

Somov, B. V. & Bogachev, S. A. 2003, Astronomy Letters, 29, 621.

Somov, B. V. & Kosugi, T. 1997, Astrophys. J., 485, 859.

Spirock, T. J., Yurchyshyn, V. B., & Wang, H. 2002, Astrophys. J., 572, 1072.

Sterling, A. C. & Moore, R. L. 2004, Astrophys. J., 602, 1024.

Sturrock, P. A. 1991, Astrophys. J., 380, 655.

Sudol, J. J. & Harvey, J. W. 2005, Astrophys. J., 635, 647.

Sun, X., Hoeksema, J. T., Liu, Y., Wiegelmann, T., Hayashi, K., Chen, Q., & Thalmann, J. 2012, ArXiv e-prints

Tanaka, K. 1991, Sol. Phys., 136, 133.

Tang, F. & Moore, R. L. 1982, Sol. Phys., 77, 263.

Toptygin, I. N. 1985, Cosmic rays in interplanetary magnetic fields, ed. Toptygin, I. N.

Tripathi, D., Isobe, H., & Mason, H. E. 2006, Astron. Astrophys., 453, 1111.

Tsuneta, S. 1985, Astrophys. J., 290, 353.

—. 1996, Astrophys. J., 456, 840.

—. 1997, Astrophys. J., 483, 507.

Tsuneta, S., Ichimoto, K., Katsukawa, Y., Nagata, S., Otsubo, M., Shimizu, T., Suematsu, Y., Nakagiri, M., Noguchi, M., Tarbell, T., Title, A., Shine, R., Rosenberg, W., Hoffmann, C., Jurcevich, B., Kushner, G., Levay, M., Lites, B., Elmore, D., Matsushita, T., Kawaguchi, N., Saito, H., Mikami, I., Hill, L. D., & Owens, J. K. 2008, Sol. Phys., 249, 167.

Uchida, Y. 1974a, Sol. Phys., 39, 431.

Uchida, Y. 1974b, in IAU Symposium, Vol. 57, Coronal Disturbances, ed. G. A. Newkirk383.

Vilmer, N. & MacKinnon, A. L. 2003, in Lecture Notes in Physics, Berlin Springer Verlag, Vol. 612, Energy Conversion and Particle Acceleration in the Solar Corona, ed. L. Klein127–160.

Waldmeier, M. 1938, Zeitschrift fur Astrophysik, 15, 299.

—. 1955, Ergebnisse und Probleme der Sonnenforschung (Leipzig: Akademische Verlagsgesellschaft Geest and Portig).

Wang, H. 1992, Sol. Phys., 140, 85.

Wang, H., Ewell, Jr., M. W., Zirin, H., & Ai, G. 1994, Astrophys. J., 424, 436.

Wang, H. & Liu, C. 2010, Astrophys. J. Lett., 716, L195.

Wang, H., Liu, C., Jing, J., & Yurchyshyn, V. 2007, Astrophys. J., 671, 973.

Wang, H., Liu, C., Qiu, J., Deng, N., Goode, P. R., & Denker, C. 2004a, Astrophys. J. Lett., 601, L195.

Wang, H., Qiu, J., Jing, J., Spirock, T. J., Yurchyshyn, V., Abramenko, V., Ji, H., & Goode, P. R. 2004b, Astrophys. J., 605, 931.

Wang, H., Spirock, T. J., Qiu, J., Ji, H., Yurchyshyn, V., Moon, Y.-J., Denker, C., & Goode, P. R. 2002, Astrophys. J., 576, 497.

Wang, S., Liu, C., Liu, R., Deng, N., Liu, Y., & Wang, H. 2012, Astrophys. J. Lett., 745, L17.

Wheatland, M. S., Sturrock, P. A., & Roumeliotis, G. 2000, Astrophys. J., 540, 1150.

Wiegelmann, T. 2004, Sol. Phys., 219, 87.

Wiegelmann, T., Inhester, B., & Sakurai, T. 2006, Sol. Phys., 233, 215.

Wiegelmann, T., Thalmann, J. K., Schrijver, C. J., De Rosa, M. L., & Metcalf, T. R. 2008, Sol. Phys., 247, 249.

Xu, Y., Jing, J., Cao, W., & Wang, H. 2010, Astrophys. J. Lett., 709, L142.

Yurchyshyn, V., Wang, H., Abramenko, V., Spirock, T. J., & Krucker, S. 2004, Astrophys. J., 605, 546.

Yurchyshyn, V. B., Wang, H., Qiu, J., Goode, P. R., & Abramenko, V. I. 2000, Astrophys. J., 540, 1143.